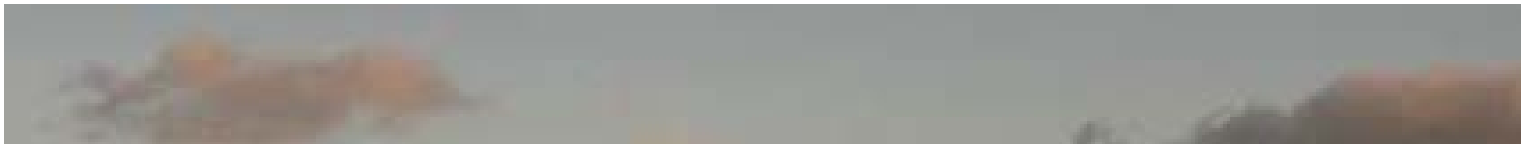

Free Access to the whole issue

E3S Web of Conferences

Volume 83 (2019)

2018 International Symposium on Hydrogen Energy and Energy Technologies (HEET 2018)

Nagoya, Japan, November 14-16, 2018

Y. Guo (Ed.)

Export the citation of the selected articles Export

Select all

Open Access

Flexible hydrogen fuel cell fabricated on paper with embedded aluminium foil 01004

Yifei Wang, Holly Kwok, Yingguang Zhang, Wending Pan and Dennis Y.C. Leung

Published online: 11 February 2019

DOI: https://doi.org/10.1051/e3sconf/20198301004

PDF (858.5 KB) | References | NASA ADS Abstract Service

Open Access

Numerical investigation on the characteristics of water transfer in PEMFC with bionic flow channel 01005

Tao Chen, Shihua Liu and Li Yang

Published online: 11 February 2019

DOI: https://doi.org/10.1051/e3sconf/20198301005

PDF (2.584 MB) | References | NASA ADS Abstract Service

Open Access

Effects of temperature on oxidation behaviours of 35CrMo in high temperature flue gas environment 01006

Chengchao Cui, Shuzhong Wang, Jianqiao Yang, Baoquan Zhang, Zhuohang Jiang, Dong Wang and Jianna Li

Published online: 11 February 2019

DOI: https://doi.org/10.1051/e3sconf/20198301006

PDF (523.4 KB) | References | NASA ADS Abstract Service

Open Access

Effect of Components Thickness on Heat and Mass Transfer Phenomena in Single Cell of PEFC Operated at High Temperature 01007

Akira Nishimura, Satoru Kamiya, Tatsuya Okado, Yusuke Sato and Masafumi Hirota

Published online: 11 February 2019

DOI: https://doi.org/10.1051/e3sconf/20198301007

PDF (953.7 KB) | References | NASA ADS Abstract Service

Open Access

Effects of cesium-substituted silicotungstic acid doped with polybenzimidazole membrane for the application of medium temperature polymer electrolyte fuel cells 01008

Kyaw Zay Ya, Pascal Nbelayim, Wai Kian Tan, Go Kawamura, Hiroyuki Muto and Atsunori Matsuda

Published online: 11 February 2019

DOI: https://doi.org/10.1051/e3sconf/20198301008

PDF (1.336 MB) | References | NASA ADS Abstract Service

Open Access

A Type of Hysteretic Nonlinear Model of Piezoelectric Sensor 01009

Qing-Xin Zhang, Zhi-Wen Zhu and Xin-Miao Li

Published online: 11 February 2019

DOI: https://doi.org/10.1051/e3sconf/20198301009

PDF (489.3 KB) | References | NASA ADS Abstract Service

Open Access

Nonlinear dynamic characteristics of SMA gripper under bounded noise 01010

Xin-Miao Li, Zhi-Wen Zhu and Qing-Xin Zhang

Published online: 11 February 2019

DOI: https://doi.org/10.1051/e3sconf/20198301010

PDF (970.3 KB) | References | NASA ADS Abstract Service

Open Access

Comparative analysis of common full scale reactors for dry anaerobic digestion process 01011

Khaled Elsharkawy, Mohamed Elsamadony and Hafez Afify

Published online: 11 February 2019

DOI: https://doi.org/10.1051/e3sconf/20198301011

PDF (335.9 KB) | References | NASA ADS Abstract Service

Open Access

Enrich waste activated sludge digestibility via natural enzyme supplementation 01012
Mohamed Elsamadony
Published online: 11 February 2019
DOI: https://doi.org/10.1051/e3sconf/20198301012
PDF (458.6 KB) | References | NASA ADS Abstract Service

Open Access
Problems and Countermeasures in Environmental Cost Accounting: A Case Study of China's Coal Industry 01013
Li-Xia Zeng, Peng He and Jin-Ping Shi
Published online: 11 February 2019
DOI: https://doi.org/10.1051/e3sconf/20198301013
PDF (245.0 KB) | References | NASA ADS Abstract Service

Open Access
Methodology Development to Locate Hydrogen Stations for the Initial Deployment Stage 01014
Kenshi Itaoka, Seiichiro Kimura and Katsuhiko Hirose
Published online: 11 February 2019
DOI: https://doi.org/10.1051/e3sconf/20198301014
PDF (1.937 MB) | References | NASA ADS Abstract Service

Open Access
Experimental Study on the Treatment of 1, 4 butanediol Mixed Wastewater by Ferro-carbon Micro-electrolysis 01015
Jie Lei, Xiaodong Zhang, Zhenglin Zhou, Shaohui Fan, Bo Jiang and Xianlan Tian
Published online: 11 February 2019
DOI: https://doi.org/10.1051/e3sconf/20198301015
PDF (627.0 KB) | References | NASA ADS Abstract Service

E3S Web of Conferences
eISSN: 2267-1242

https://www.e3s-conferences.org/articles/e3sconf/abs/2019/09/contents/contents.html

Statement of Peer review

In submitting conference proceedings to *Web of Conferences*, the editors of the proceedings certify to the Publisher that

1. They adhere to its **Policy on Publishing Integrity** in order to safeguard good scientific practice in publishing.
2. All articles have been subjected to peer review administered by the proceedings editors.
3. Reviews have been conducted by expert referees, who have been requested to provide unbiased and constructive comments aimed, whenever possible, at improving the work.
4. Proceedings editors have taken all reasonable steps to ensure the quality of the materials they publish and their decision to accept or reject a paper for publication has been based only on the merits of the work and the relevance to the journal.

Title, date and place of the conference

2018 International Symposium on Hydrogen Energy and Energy Technologies (HEET 2018)
November 14-16, 2018 | Nagoya, Japan

Proceedings editor(s):

Yun Guo

Date and editor's signature

16-01-2019

17, avenue du Hoggar - PA de Courtabœuf – BP 112 - 91944 Les Ulis Cedex A (France)
Tél. : 33 (0)1 69 18 75 75 - Fax : 33(0)1 69 07 45 17 – www.edpsciences.org

This is the proceeding of the 2018 International Symposium on Hydrogen Energy and Energy Technologies (HEET 2018), held at Tokyu Hotel Nagoya, Japan during November 14-16, 2018.

The vision of the HEET 2018 is provides a premier interdisciplinary platform for researchers, practitioners and educators to present and discuss the most recent innovations, trends, and concerns as well as practical challenges encountered and solutions adopted in the fields of Hydrogen Energy & Energy Technologies.

The conference has successfully performing forum to transferring and discussing research result among the researcher, students, government, private sector or industries. Participants and presenters from several countries such as USA, Denmark, Japan, China, South Korea, Qatar, Belgium, Germany, Netherlands, France have attended the conference to share their significant contribution in research related to, Hydrogen Energy & Energy Technologies.

We are thankful to all the authors who submitted papers and the delegates for their participation and their interest in HEET as a platform to share their ideas and innovation. Also, we are also thankful to all the committee members for providing continuous guidance and support and Efforts taken by peer reviewers contributed to improve the quality of papers provided constructive critical comments, improvements and corrections to the authors are gratefully appreciated for their contribution to the success of the conference.

Study on the enhancement of hydrogen generation via biomass gasification in fluidized-bed reactors

Yau-Pin Chyou[1,*], *Po-Chuang* Chen[1], *Der-Ming* Chang[1], *Keng-Tung* Wu[2], and *Rei-Yu* Chein[3]

[1]Institute of Nuclear Energy Research, Chemistry Division, 325 Taoyuan, Taiwan ROC
[2]National Chung Hsing University, Department of Forestry, 402 Taichung, Taiwan ROC
[3]National Chung Hsing University, Department of Mechanical Engineering, 402 Taichung, Taiwan ROC

Abstract. In this study, solid biomass is gasified in fluidized-bed reactors, to investigate the effect of various means on syngas composition, especially for enhancing hydrogen content in the production gas. Conventionally, air is supplied to the reactor as gasification medium, which inevitably results in a high nitrogen content in the syngas. Alternatively, steam or oxygen-rich gas can be supplied to improve the syngas characteristics. On the other hand, a so-called "indirect gasification technology" realizes the whole conversion processes in dual reactors, for combustion and gasification, respectively; moreover, solid materials are circulated through two reactors, while gaseous streams in between are separated from each other. Hence, this system features the advantage of producing near nitrogen-free syngas in the gasifier, with air as oxidant in the combustor. Baseline experiments with various operating parameters, including air equivalence ratio (ER) and temperature, were firstly performed in a 30 kW_{th} bubbling fluidized-bed gasifier; then, trial tests were conducted with the aforementioned operational and constructional factors. The preliminary test data show positive trends for the enhancement of hydrogen generation via biomass gasification. Further efforts will be pursued to establish a data base, which would be beneficial to extensive researches on clean energy and carbon abatement technologies.

1 Introduction

With the ambitious goal set by the "Paris Agreement," which aims at a level even below 2DS (two-degree scenario), a large amount emission of greenhouse gas (GHG), predominantly carbon dioxide (CO_2), caused by anthropogenic impacts has been an environmental issue around the globe for the climate change. However, increased concentrations of CO_2 in the environment are inevitable unless energy systems reduce the carbon emissions to the atmosphere. Decarbonizing the energy systems is a daunting challenge in the 2DS. It is essential to pursue follow-up efforts for energy utilization with

* Corresponding author: ypchyou@iner.gov.tw (Y.-P. Chyou)

lower carbon and pollutant emissions, as well as mitigate GHG emissions from the viewpoints of sustainability, which requires various portfolios. Furthermore, biomass can further reduce the carbon dioxide emission, due to the feature of carbon neutral. Hence, clean utilization of biomass via gasification technology is developed in this work.

Gasification technology is a kind of thermo-chemical process for converting carbonaceous feedstock to syngas, mainly consisting of CO, H_2, CO_2, H_2O, CH_4, etc., which can be further utilized in various application processes to meet the multiple energy and resource demands from the industry [1]. Gas generated from gasification process, dominantly CO and H_2, can be further converted to chemical products and liquid fuel after clean-up processes; while some carbon could be fixed in the chemical products or separated in the processes as requested from end applications, of which the feature results in lower CO_2 emission. Syngas could also be delivered to combined-cycle for generating electricity, so that the system efficiency is increased and pollutant emission is decreased.

Fluidized bed is one of the major platforms of biomass gasification. It utilizes gasification-medium (air, steam, CO_2 etc.) through the solid particles and makes them behave like fluid flow. Furthermore, there are some advantages when implementing fluidized bed for gasification, e.g., lower pollution, high efficiency and flexible feedstock [2-4]. Conventionally, air is supplied to the reactor as gasification medium, which inevitably results in high nitrogen content in the syngas. Alternatively, steam or oxygen-rich gas can be supplied to improve the syngas characteristics.

On the other hand, a so-called "indirect gasification technology" realizes the whole conversion processes in dual reactors, for combustion and gasification, respectively; moreover, solid materials are circulated through two reactors, while gaseous streams in between are separated from each other (Fig. 1). Hence, this system features the advantage of producing near nitrogen-free syngas in the gasifier, with air as oxidant in the combustor.

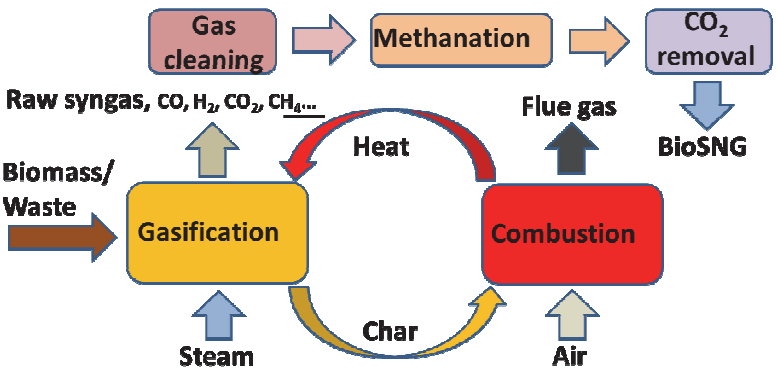

Fig. 1. Conceptual sketch of indirect gasification technology and application.

A comprehensive review on dual fluidized-bed (DFB) biomass gasifiers has been published in the literature [5]. A description of the gasifiers operated today is given, e.g., in Europe (TU Wien and Güssing in Austria [6] and ECN in The Netherlands [7]), and in Japan (IHI Co. [8], EBARA [9]). Biomass gasification with pure steam in a fluidized bed may generate a gasification gas with 60 vol % H_2 (dry basis). Thus, a gasification gas that is very rich in H_2 and with relatively low tar content, for which steam reacts with tar compounds, currently can be obtained, via biomass gasification with pure steam. This concept is also suitable for Bio-SNG production [10].

Interconnected fluidized bed (IFB), regarded as an alternative type of reactor for circulating operation, configures the reactor vessel and associated piping into integrated compartments, which facilitate solid circulation through the beds and enhance the system performance. With higher solid circulating rates and less particle attrition, IFB has been developed as a new application for many particle operations on physical and chemical processes.

Originally, Kunii proposed a conceptual design of a new compact fluidized-bed reactor combined with gasification and combustion processes 1980 [11]. In 1990's, the concept to develop the applications of the interconnected fluidized bed, such as the regenerative desulfurization process [12 - 15], has been realized at Delft University of Technology (DUT) in the Netherlands. In 2004, Wu et al. at Industrial Technology Research Institute (ITRI), Taiwan constructed a 200 kW_{th} interconnected fluidized bed gasification test facility to carry out gasification of refuse derived fuel (RDF) to obtain the performance information for future development [16].

Figure 2 shows the configuration of an interconnected fluidized bed [16]. The IFB system consists of four fluidization compartments, for which two dense-phase beds and two lean-phase beds are alternatively connected by weirs and orifices, respectively. The two lean-phase beds denote gasification zone and combustion zone, respectively. The two dense-phase beds denote the piping and feature to prevent the gas penetration from one lean-phase bed to another one. Hence, the gas in the gasification zone and combustion zone is individually isolated. The solids within the dense-phase bed flow with a lower velocity through the orifice into the lean-phase bed, and then ascend with a higher velocity over the weir into another dense-phase bed.

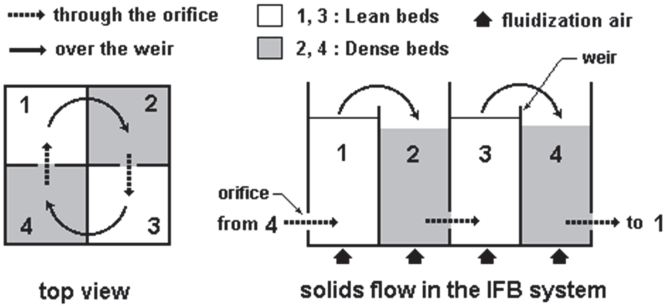

Fig. 2. Configuration of an interconnected fluidized bed.

2 Experimental

In recent years, research on mitigating greenhouse gas emissions and sustainable clean coal technologies has been undertaken at the Institute of Nuclear Energy Research (INER) in Taiwan, together with cooperative research teams at National Chung Hsing University (NCHU). In summary, this work acquires preliminary results for the gasification of Eucalyptus, and further efforts will be pursued to establish a data base for gasification reaction performance and optimal operating parameters, which would be beneficial to extensive researches on clean energy and carbon abatement technologies.

2.1 Feedstock

In this study, there are two types of feedstock used in gasification, i. e., Eucalyptus wood chips and mixed wood pellet. The feedstock size is smaller than 7 mm. Other feedstock properties are shown in Table 1.

Table 1. Feedstock property analysis.

Ultimate analysis (wt. %, daf*) :					
	C	H	O	N	S
Eucalyptus	49.07	4.92	44.94	0.27	0.16
Mixed Wood Pellet	49.52	6.26	43.50	0.72	0.0
Proximate analysis (wt. %, a.r.*) :					
	Moisture		Ash	Combustible	
Eucalyptus	11.48		0.56	85.9	
Mixed Wood Pellet	9.95		1.02	88.29	
Heating value (HHV, MJ/kg, a.r.)					
Eucalyptus	17.34				
Mixed Wood Pellet	17.69				

*daf: dry ash free a.r.: as received

2.2 Platform

As a start-up effort, a 30 kW_{th} bubbling fluidized-bed (BFB) gasification system has been commissioned; then, the facilities is extended to circulating fluidized-bed (CFB) mode. Later, construction efforts of various dual fluidized-bed (DFB) reactors are in progress.

2.2.1 Solo fluidized bed

Figure 3 shows the 30 kWth bubbling fluidized-bed gasification system, consisting of the feeding system, gasification chamber, air supply system, syngas cleaning system, tar sampling unit and syngas analysis system [17]. This gasifier is made of SUS310 stainless steel with an internal diameter of 6.2 cm in the bed region and total height of 580 cm, enclosed by insulating material of ceramic fibre to shield the heat loss and supplemented by an electric heating system for controlling experimental condition. Silica sand with 2.6 g/cm^3 in density and 505μm in average particle size were used as bed material.

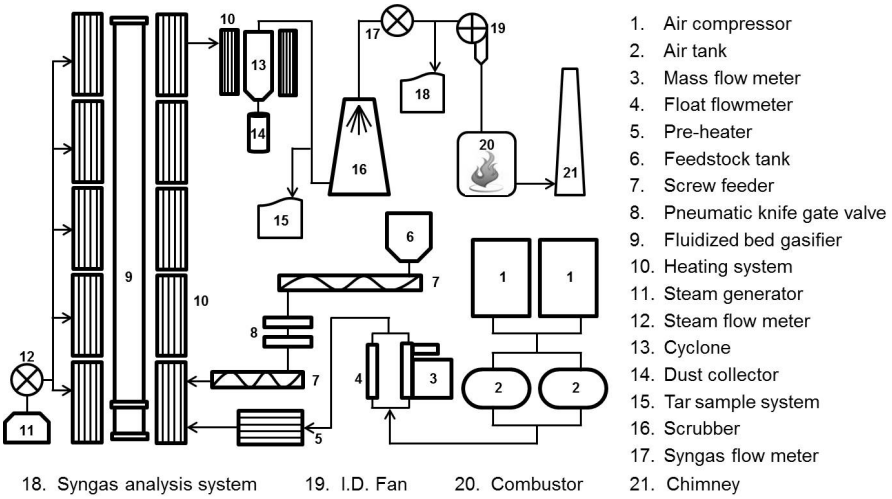

Fig. 3. The 30 kW_{th} bubbling fluidized-bed gasification system.

Syngas analysis system includes online analysis and batch system. The online analysis system is manufactured by Siemens, showing the content of CO, CO_2, O_2, H_2 and CH_4 during the experiment, which displays the timing for sampling the tar and syngas.

2.2.2 Interconnected fluidized beds

Both the cold model and hot model of IFB were commissioned. The former is to investigate hydrodynamic behavior [18], while the latter is for characteristics of thermos-chemical conversion [19]. Figure 4 presents the schematic of a 20 kW_{th} IFB gasification system. Steam generator will be equipped for further study of steam gasification in the future. Two bed materials were adopted in the study: the first one is silica sand, which is for operation in typical gasification; while the other one is ilmenite, which can release oxygen to investigate the effect on syngas compositions..

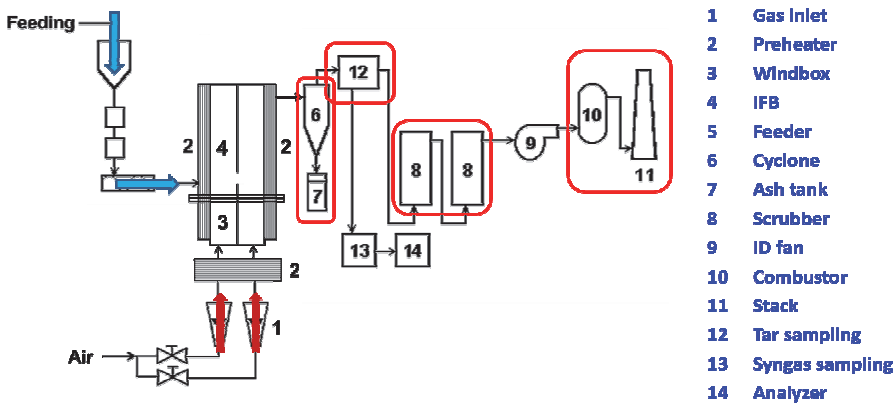

Fig. 4. The 20 kW_{th} IFB gasification system.

2.2.3 Dual fluidized beds

Indirect gasification can achieve nearly nitrogen-free syngas without using air separation unit (ASU) for generating pure oxygen or oxygen-rich stream. At present, a cold flow model was designed by referring to the actual size of the 100 kW_{th} dual fluidized beds, and operating based on dimensionless analysis. The apparatus of the cold model has thirteen pressure gauges which located on the two fluidized-bed reactor as well as the upper and the lower loop seals (Fig 5(a)). The test results were recorded by the instrument equipped. The main body of the cold model was constructed by acrylic material (Fig 5(b)). The characteristics of cold model provide the building blocks for the DFB hot model currently under commissioning at INER.

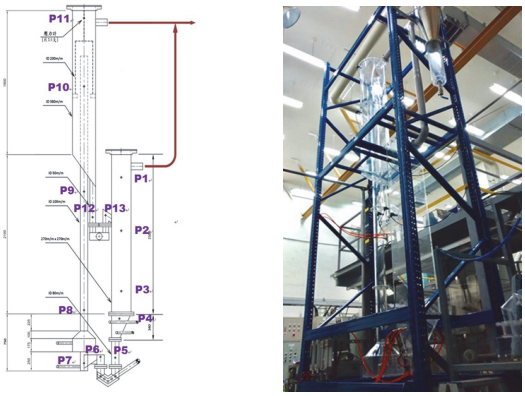

Fig. 5. The cold model of DFB gasification system: (a) Sketch of the cold model and the location of the pressure transmitters (P1~P13), and (b) the photo of the test apparatus.

The physical property of the bed material (olivine) and of the exhaust gas/product syngas in the hot mode reactor are listed in Table 2, at the CRH (combustion reactor) and GRH (gasification reactor) columns, respectively. Farrel's proposed that dimensionless group, e.g., De, Ar, Fl, Gs*, Fr and Rep, were could be calculated using these parameters in combination with the size of the cold model [20]. However, due to two degrees of freedom (i.e., U and Gs), only two dimensionless group values (Fl and Gs*) can be the same as (or close to) the hot model. Hence, the glass beat was selected as bed material in cold model.

Further analysis of the characteristics of the system, the average pressure distribution pattern is similar to that of the published literature [6]. The pressure distribution data are under analysis processes, and will be presented in the further study.

Both IFB and DFB have key features of two independent reaction zones with the gases being isolated. It is easy to adopt steam as gasification medium to generate nitrogen-free syngas. Steam is generally used in industry and is relatively cheaper compared with oxygen as gasification medium. But, steam-blown gasification reactions are endothermic and result in a requirement of an external heat source. The external heat is provided by the bed material that is circulating between the two beds. Adopting IFB to apply in steam gasification is a new concept and is still in the early stage of development. Thus, the hot model of IFB is using air as gasification medium in the first stage, to simplify the experimental procedure. The experimental data are used as the base case to make comparison with those of steam gasification in the further study. On the other hand, DFB

has been well employed in the steam gasification, and is introduced in the study to make comparison with IFB in the future.

Table 2. The results of dimensionless analysis.

		CR_H	CR_C	GR_H	GR_C
Bed Material		Olivine	Glass	Olivine	Glass
η_G	Pa s	4.50E-05	1.83E-05	3.59E-05	1.83E-05
ρ_G	kg m^{-3}	0.29	1.15	0.20	1.15
U	m s^{-1}	9.20	3.06	0.66	0.19
ρ_P	g cm^{-3}	2.85	2.42	2.85	2.42
d_P	μm	520.00	200.00	520.00	200.00
Φ	-	0.80	0.80	0.80	0.80
D	mm	102.30	102.30	270x270	270x270
G_S	kg m^{-2} s^{-1}	42.24	11.85		
De	ρ_P/ρ_G	9796.98	2095.53	14103.04	2095.53
Ar	dp3*ρg*(ρs-ρg)*g/μ2	564.21	652.06	616.49	652.06
Fl	U/u_{mf}	120.45	130.00	6.88	8.00
G_S*	$G_S\rho_p^{-1}$ U^{-1}	1.61E-03	1.60E-03		
Fr	$U^2/g\ d_p$	16608.26	4780.76	85.32	18.10
Re_p		30.93	38.58	1.93	2.37
$Ar^{1/3}$		8.26	8.67	8.51	8.67
U*	$Re_p/Ar^{1/3}$	3.74	4.45	0.23	0.27
Q_o	m^3/h	272.22	90.58	173.05	49.44
m_s	kg h^{-1}	1250.00	350.72		

3 Results and Discussion

3.1 Baseline performance characteristics

The baseline gasification experiments were performed in the 30 kW_{th} bubbling fluidized-bed gasification system as shown in Figure 3, to investigate the effect of various operating parameters, including air equivalence ratio (ER) and temperature. The equivalent ratio (ER) is defined as the actual air-fuel ratio to stoichiometric air-fuel ratio. There are three equivalent ratio (ER=0.2, 0.3 and 0.4) and three experimental temperature (700, 800 and 900°C) as the experimental conditions in this study.

The effect of ER on CO and H_2 content in the syngas of Eucalyptus wood chips gasification are presented as contours in Figure 6. It is shown that CO and H_2 increased as ER decreased. As ER increasing, more air is supplied to the gasifier; according to Le Chatelier's Principle, whole gasification would tend to oxidation. Also it enhances the burning of char to generate CO_2 with the compensation of product gas such as H_2, CO and CH_4. As a result, there are more CO_2 while less H_2 and CO when the ER is increased. The trends are all consistent with previous research [21 - 23].

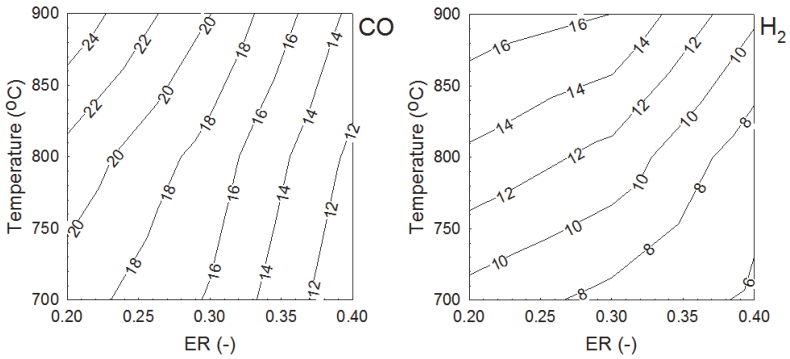

Fig. 6. Contours of CO and H_2 [%] in the syngas of Eucalyptus gasification.

Temperature is another important parameter in gasification. When the temperature ascends, CO and H_2 increase, which is consistent with the results of previous studies [24, 25]. Higher temperature promotes some endothermic reaction, like Boudouard reaction($C+CO_2 \rightarrow 2CO$) and water gas reaction ($C+H_2O \rightarrow CO+H_2$, $C+2H_2O \rightarrow CO_2+2H_2$), to produce more CO and H_2. On the other hand, CO/CO_2 ratio will be higher as temperature increases. When temperature is higher than 830°C, the Boudouard reaction will have more effect than the water gas reaction [26].

3.2 Influence of gasification medium

As mentioned before, air is usually supplied to the reactor as gasification medium for simplicity and cost reasons, which in turn results in high nitrogen content in the syngas. From operational viewpoints, alternative media, e.g., steam or oxygen-rich gas, can be implemented to improve the syngas characteristics.

Two trial tests were conducted to verify the above scenarios. The first case is to address the influence of steam. The reference case in Fig. 7 was carried out under the following operating conditions: feedstock mass flow rate 2 (kg/h), temperature 900°C and ER 0.3. For comparison, an additional stream of steam to fuel ratio (kg/kg) SF = 0.4 was injected to the reactor. Although the steam temperature was substantially lower, due to equipment limitation, than that in the reactor, it is clearly seen that hydrogen generation is enhanced.

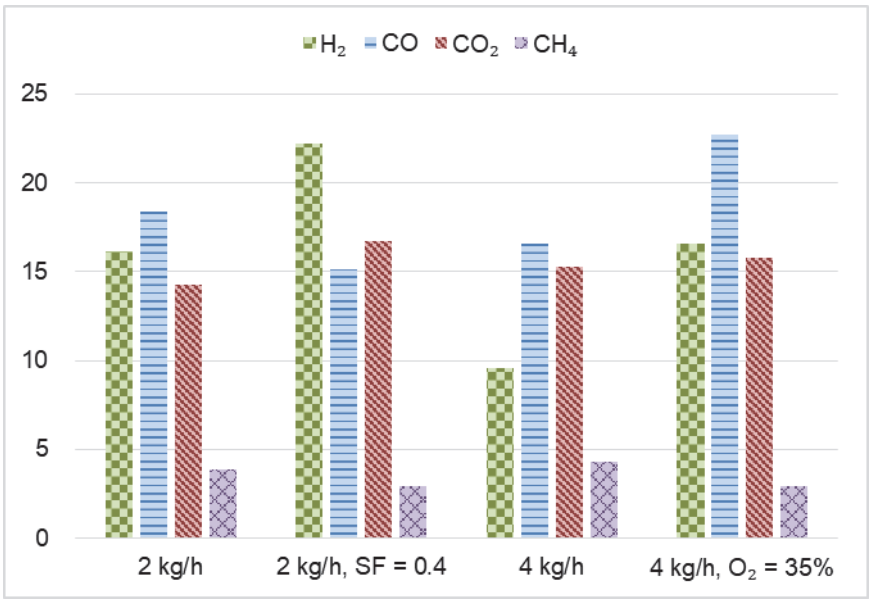

Fig. 7. Comparison of syngas composition with various gasification media.

Oxygen-rich gas is another candidate for enhancing hydrogen generation. Again in Fig. 9, the reference case was carried out under the following operating conditions: feedstock mass flow rate 4 (kg/h), temperature 900°C and ER 0.3. Then, the oxygen content was increased to 35%; as a consequence, hydrogen generation is enhanced as well.

3.3 Effect of indirect gasification

Figure 8 presents the effect of indirect gasification on syngas composition. The experiments were carried out under the following operating conditions: feedstock mass flow rate 2 (kg/h), temperature 900°C and ER 0.2. Since IFB features nearly zero N_2 environment in the gasifier when steam is used as gasification medium, the composition of syngas is presented as N_2-free condition for the cases of air as gasification medium from the current test rig in Fig. 4, to make convenience for comparing with steam counterpart in the further study. For fair comparison, the BFB data were adjusted to the same condition. It is seen that IFB exhibits potential for enhancing hydrogen generation, based on the preliminary trial.

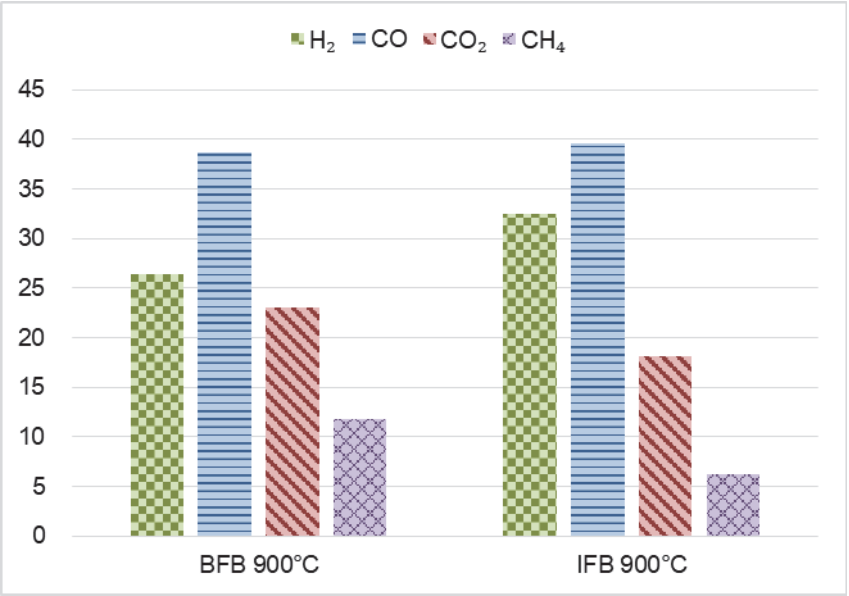

Fig. 8. Effect of indirect gasification on syngas composition (N_2-free): BFB vs. IFB.

3.4 Effect of chemical looping gasification

On the other hand, chemical looping process (CLP) is an enabling technology for advanced CO_2 separation option with great potential, which realizes the looping of solid materials through two reactors, while gaseous streams in between are separated from each other. Thus, the IFB, as a new CLP reactor, can be employed to reduce particle attrition, increase solid circulating rates, and separate CO_2 simultaneously. Hence, oxygen carrier (OC), ilmenite imported from Australia, was utilized to assist the gasification; as shown in Fig. 9, hydrogen generation is enhanced.

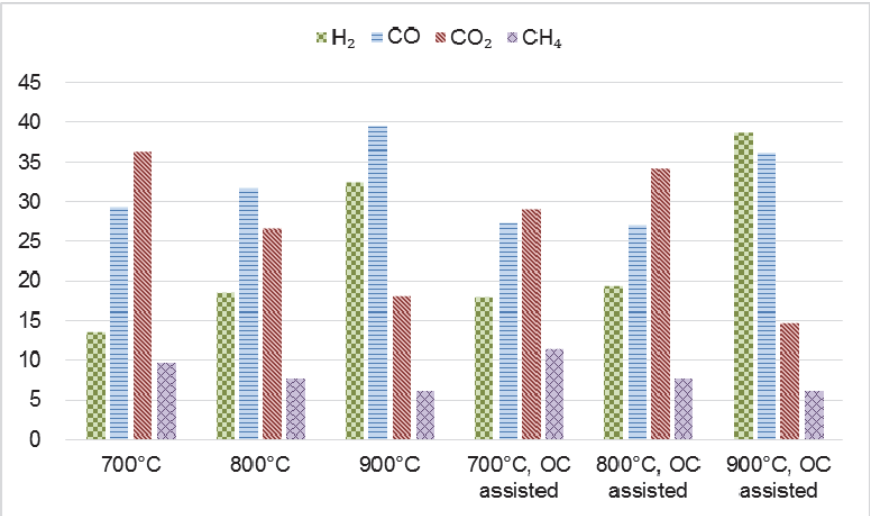

Fig. 9. Effect of chemical looping gasification on syngas composition (N_2-free): IFB.

4 Conclusions

Gasification experiments of biomass were performed in various fluidized-bed reactors to investigate the potential means for the enhancement of hydrogen generation. The preliminary test data show positive trends for the experiments conducted with the aforementioned operational and constructional factors. Further efforts will be pursued to establish a data base for gasification reaction performance and optimal operating parameters. The outcome would be beneficial to extensive researches on clean energy and carbon abatement technologies.

The authors are grateful to the financial support from governmental R&D budget allocated to the Institute of Nuclear Energy Research (INER), Atomic Energy Council (AEC), and the Bureau of Energy (BoE), Ministry of Economic Affairs (MoEA) of Taiwan, ROC. The efforts provided by the CaSE (Clean Carbon as Sustainable Energy) project at INER and the research teams at NCHU are also acknowledged.

References

1. J. Raizaiyan, N.P. Cheremisinoff, *Gasification Technologies* (CRC Press, New York, 2005)

2. Z.A.B.Z. Alauddin, P. Lahijani, M. Mohammadi, A.R. Mohamedb, Renew. Sust. Energ. Rev. **14**, 2852 (2010).

3. P. Basu, *Combustion and gasification in fluidized beds*, (CRC Press, New York, 2006)

4. R.L. Bain, *2004 AIChE spring national meeting-conference proceedings*, 547 (2004).

5. J. Corella, J.M. Toledo, G. Molina, Ind. Eng. Chem. Res. **46**, 6831 (2007)

6. S. Koppatz, C. Pfeifer, H. Hofbauer, Chem. Eng. J. **175**, 468 (2011)

7. B. van der Drift, *IEA Bioenergy*, Task 33 workshop (2015)

8. T. Kumagai, *75th IEA-FBC Meeting*, Skive, Denmark (2017)

9. T. Ohshita, (In Jpn.), Suiso Enerugi Shisutemu, **28**, 93 (2003)

10. K. Bengtsson, Twin-bed Gasification Concepts for Bio-SNG Production (Department of Chemical Egineering, Lund University, Sweden, (2007)

11. D. Kunii , Chem. Eng. Sci., **35**, 1887 (1980).

12. R. Korbee, J.C. Schouten and C.M. van den Bleek, AICHE Symp. Ser., **87**, 70 (1991).

13. R. Korbee, O.C. Snip, J.C. Schouten, C.M. van den Bleek, Chem. Eng. Sci., **49**, 5819 (1994).

14. O.C. Snip, R. Korbee, J.C. Schouten, C.M. van den Bleek, AIChE Symp. Series, **91**, 82 (1995).

15. O.C. Snip, M. Woods, R. Korbee, J.C. Schouten, C.M. van den Bleek, Chem. Eng. Sci., **51A**, 2021 (1996).

16. K.-T. Wu, J.S. Wang, H.F. Lee, S.J. Hwang, and H.T. Lee, *Proceedings of 9th Asian Conference on Fluidized-Bed and Three-Phase Reactors*, Taipei, 97-102 (2004).

17. H.-T. Hsu, S.-C. Lin, Y.-P. Chyou, *The 13th International Conference on Combustion & Energy Utilization*, Taipei, Taiwan, (2016)

18. Y.-P. Chyou, Y.-C. Tung, K.-T. Wu, C.-J. Tsai, P.-C. Chen, H.-T. Hsu, *The 24th European Biomass Conference & Exhibition,* Amsterdam, Netherlands, (2016)

19. Y.-P. Chyou, W.-C. Chang, Y.-C. Tung, P.-C. Chen, R.-Y. Chein, K.-T. Wu, *The 9th International Freiberg Conference on IGCC & XtL Technologies*, Berlin, Germany (2018)

20. P.A. Farrel, *Hydrodynamic scaling and solids mixing in pressurized bubbling fluidized bed combustors* (Ph. D. thesis, MIT, USA, 1996)

21. Z.A.B.Z. Alauddin, P. Lahijani, M. Mohammadi, A.R. Mohamed, Renew. Sust. Energ. Rev., **14**, 2852 (2010)

22. P. Lv, Z.L. Yuan, C.W. Ma, Y. Chen, J. Zhu, Renew. Energ., **32**, 2173 (2007)

23. K. Qin, W. Lin, P.A. Jensen, A.D. Jensen, Fuel, **93**, 589 (2012)

24. M. Karmakar, A. Datta, Bioresource technol., **102**, 1907 (2011)

25. K. Umeki, T. Namioka, K. Yoshikawa, Fuel Process. Technol., **94**, 53 (2012)

26. E. Kantarelis, P. Donaj, W. Yang, A. Zabaniotou, J. hazard. Mater., **167**, 675 (2009)

Review of Supercritical Hydrothermal Combustion

Haitao Xu[1], *Shuzhong* Wang[1,*], *Mengmeng* Ren[1], *Jianqiao* Yang[1], *Chengchao* Cui[1], *Yanhui* Li[1], *Jie* Zhang[2]

[1]Key Laboratory of Thermo-Fluid Science and Engineering of MOE, School of Energy and Power Engineering, Xi'an Jiaotong University, China

[2]State Key Laboratory Base of Eco-hydraulic Engineering in Arid Area, Xi'an University of Technology, China

Abstract. Two major points in supercritical hydrothermal combustion were reviewed:(1) The structure of semi-batch reactors or continuous reactors used in different institutes and colleges. These investigations can be used to guide the design of reactors for later scholars and lay the foundation for the industrialization of supercritical hydrothermal combustion. (2) The research status of characterization of hydrothermal flame processes by various scholars. These investigations can be used to guide the process parameters of industrialization of supercritical hydrothermal combustion. The continuous reactor designed in each organization is very sophisticated, which can avoid the two major problems of reaction in the supercritical state: salt precipitation and corrosion. The ignition temperature, extinction temperature, and other characteristics of supercritical hydrothermal combustion studied by scholars are summarized and the laws are basically similar. The removal rate of different organic matters was also summarized under supercritical hydrothermal combustion, and the removal rate of more than 99% was basically achieved.

1 Introduction

Supercritical water(SCW) refers to water in the environment where both temperature and pressure are above its critical point(T>374°C, P>22.1MPa). Supercritical water has special physical and chemical properties such as high diffusivity, low density, low viscosity, low dielectric constant and small amount of hydrogen bonds. Therefore, a satisfactory reaction environment is provided. Supercritical hydrothermal combustion means (SCHC) that in supercritical water, the fuel above a certain concentration reaches the ignition point, and the fuel is ignited with the phenomenon of "water-fire compatibility". Supercritical hydrothermal combustion was first proposed by Franck[1,2] and his colleagues in 1987. For more than 30 years, the University of Valladolid (Uva), Swiss Federal Institute of Technology Zurich(ETH), Xi'an Jiaotong University (Xjtu), Karlsruhe Institute of

* *Shuzhong* Wang: szwang@aliyun.com

Technology (KIT) and others research institutes have conducted extensive research on supercritical hydrothermal combustion.

Supercritical hydrothermal combustion is a special supercritical water oxidation process which was firstly proposed by Modell[3], and different scholars gave similar views to judge whether there is severe supercritical water oxidation — supercritical hydrothermal combustion. Provided that the reactor is equipped with a visualization window of sapphire or quartz glass, it can be directly observed whether there are hydrothermal flames in the reactor. The supercritical hydrothermal combustion research results on coal of Ma[4] represent that when the surface temperature of coal particles is much higher than the temperature of the surrounding fluid (generally the surface temperature of the particles is more than 800 ℃), it is taken into account that the supercritical hydrothermal combustion reaction of coal occurs. Zhang[5] believes that supercritical hydrothermal combustion occurs when the temperature of fluid in the reactor rises sharply (at least 100 ℃/min). Augustine[6] believes that the hydrothermal flame which operates in a regime of thermal runaway has the features of extremely fast reaction rates(with residence times being only 10–100ms) and high temperatures(usually more than 1000 °C).

Supercritical hydrothermal combustion has other advantages over flameless supercritical water oxidation. Supercritical hydrothermal combustion can be used to solve two of the major obstacles confronting the practical application of SCWO to the treatment of hazardous, toxic, or non-biodegradable aqueous organic waste streams—metal corrosion at high temperature and plugging of the reactor due to precipitating salt solids[6]. As an example, the temperature in the local high temperature zone possessed by supercritical hydrothermal combustion is higher than that of the flameless supercritical water, so the ability to destroy refractory organic matter is stronger. Additionally, supercritical hydrothermal combustion is more intense than the flameless supercritical water oxidation, and the residence time of supercritical hydrothermal combustion is generally less than 1 s. Moreover, the fast reaction makes the reactor size smaller and the cost less. Therefore, it is easier to industrialize and more economical.

At present, scholars' research on supercritical hydrothermal combustion focuses on flame characteristics: ignition temperature, extinction temperature, flame temperature, flame height (diameter), the total organic carbon (TOC) removal rate of organic matter or waste and the design of the reactor.

2 Reactor designed by different organization

Reddy[7] proposed that hydrothermal flames are divided into premixed flames and diffusion limited flames. According to the feed flow rate (usually depends on Reynolds number), hydrothermal flames can also be divided into laminar hydrothermal flames and turbulent hydrothermal flames. The types of hydrothermal flames can be seen in Figure 1.

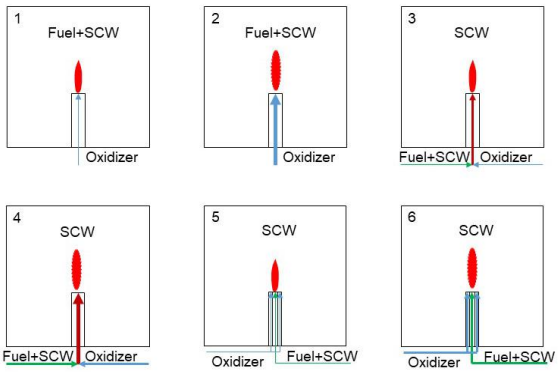

Fig. 1. The types of hydrothermal flames: (1) laminar flames in semi-batch reactor, (2) turbulent flames in semi-batch reactor,(3) laminar flames in continuous reactor(premixed),(4) turbulent flames in continuous reactor(premixed), (5) laminar flames in continuous reactor and (6) turbulent flames in continuous reactor

There are two types of reactors for supercritical hydrothermal combustion: semi-batch reactors and continuous reactors. The semi-batch reactor means that the inside of the reactor is flooded with fuel, and thereafter the oxidant is injected into the reactor through the nozzle, and the fuel is ignited once the inside of the reactor satisfies the hydrothermal flame ignition condition. The flame is extinguished as the internal fuel gradually decreases until it is exhausted. Continuous reactors mean that fuels and oxidants are injected into the interior of the reactor at the same time, and hydrothermal flames are ignited once the inside of the reactor satisfies certain conditions. In theory, the injection of fuel and oxidant is not stopped, and the flame will not be extinguished.

Continuous reactors are divided into three main types: transpiring wall reactor (TWR), wall-cooled hydrothermal burner (WCHB) and tubular reactor. Subcritical water which can form a thin water film is injected into micropores on the inner wall of TWR. The thin water film prevents corrosive substances from coming into contact with the wall and dissolves salts. The wall of the WCHB is cooled with cold water to prevent high-temperature corrosion. The place where the cold water is in contact with the supercritical water can lower the temperature and redissolve the inorganic salt to prevent salt deposition.

2.1 Semi-batch reactor

Reactor studies began with semi-batch reactors. The semi-batch reactor used in the Sandia National Laboratory in the United States can be seen in Steeper et al [8]. Steeper uses a 14.7 mL reactor to prefill water and methane (or methanol) in a supercritical state, and then inject oxygen from the bottom import. Thereby, the process of the hydrothermal flame from ignition to extinction is obtained, and the ignition characteristic curve of methane and methanol is obtained. The device has three sapphire windows, with the right side being the incident laser port, the left side being the transmitted laser port, and the top being the scattered light collection port. The device can therefore identify the indoor components as well as the fuel concentration by using Raman scattering.

The semi-batch reactor used at McGill University can be seen in sobhy et al [9], with a reactor's volume of 15 mL. Sobhy first injects the methanol solution into the reactor through the test fluid loading port. Once the internal pressure of the reactor reaches 23 MPa, it is heated to 400 ℃. Afterward, 400 ℃ of dry air is injected into the reactor through the air injection nozzle to generate a hydrothermal flame. The hydrothermal flame can be observed through the sapphire window port, or the hydrothermal flame image can be

obtained by infrared imaging. Sobhy obtained the destruction efficiency of naphthalene under hydrothermal combustion conditions by this device.

2.2 Continuous reactors

The Federal Institute of Technology in Zurich, Switzerland, began research on supercritical hydrothermal combustion in 1996. The research team designed a TWR and WCHBs. The WCHBs has four generations[10-12], and first three generations are similar in structure.

The water and fuel of the first generation WCHB[10] are injected from the middle lower port, and oxygen is injected into the burner from the side annular port to ignite, while the subcritical water is injected from the outer ring of the burner to cool the burner wall. The product is discharged from the upper port. This generation has two sapphire window ports at the end of the burner, which can see the process of the hydrothermal flames from ignition to extinction. The second generation is similar in structure to the first generation, but the length of the burner is longer, while the sapphire window port is increased from 20mm to 165mm. In comparison with the first generation, the third generation moved the inlet and burner from below to the top, while the sapphire window ports increased from two to four and the length increased from 20mm to 85mm. The hydrothermal combustion reaction in the combustion chamber can be observed from all directions.

The fourth generation WCHB[12] is a combination of a coaxial and a radial nozzle where the fuel is injected at 30° with respect to the oxygen flow and produces the turbulent flame. Main volume of the reactor is 5.83L. In addition, inside the combustion chamber is a heating coil that uses electricity to ignite the hydrothermal flame. This is also the focus of ETH's recent research.

The TWR of the Swiss Federal Institute of Technology in Zurich can be seen in Wellig et al[13]. The fuel is injected from the upper center, and the first oxygen is injected into the burner from the outer ring of the fuel port to ignite. The waste water is injected from the outer ring of the burner, and the second oxygen is injected from the outermost ring to the supply oxygen. The lower part of the reactor is a transpiring with four transpiring wall ports for supplying subcritical water to form a thin water film, which not only prevents salt from depositing on the wall, but also prevents high temperature corrosion substances generated by the reaction from contacting on the wall. In addition, since there are four transpiring wall ports, it is easy to install temperature measurement points. The device can also just preheat wall water, fuel and air, and these substances are less corrosive.

The University of Valladolid designed some reactors. The WCHB which can be seen in Bermejo et al[14] designed by the team has a structure that exchanges heat between the internal high-temperature heat source and material. A salt precipitation chamber below ensures that the mixer is not clogged, while a long reaction chamber passage extends the reaction time. Additionally, it is safe for the reason that pressure shell is far away from reaction chamber at high temperature.

Another WCHB was designed by the University of Valladolid, which can be seen in Cabeza et al[15]. The reactor uses cooling water to cool the wall between internal wall and external wall. Feed flow and air are premixed in internal wall and then react in reaction chamber. The reaction product flows out from bottom. This reactor is characterized by its simple structure.

The University of Valladolid also designed a TWR with a volume of 6.3L, which can be seen in Bermejo et al[16]. The reactor consists of stainless steel and the clean transpiring water circulates around the porous wall to protect the wall from corrosion and salt deposition. Similar to the WCHB mentioned before, the feed flow and air are premixed in static mixer and then react in reaction chamber. The reaction products also flow out from bottom. The characteristics of the reactor is that pressure shell which bears pressure is

separated from reaction chamber which bears high temperature. Therefore, the structure is safer.

China's Xi'an Jiaotong University began research on supercritical hydrothermal combustion in 2005 and designed a multi-functional supercritical hydrothermal combustion reactor, as shown in the following figure 2. The reactor has an inner cylinder which can be replaced by transpiring wall or cooled wall. Inside the inner cylinder is a combustion reaction chamber with a fuel inlet, a waste inlet and an oxidant inlet. There are four thermocouples on the upper and lower sides to measure the internal temperature. The outer wall is a pressure-bearing wall, and there are three ports on the wall. If the inner cylinder is a cooled wall, the upper left port is blocked, the water is poured from the lower port, and the upper right port is discharged. If the inner cylinder is a porous transpiring wall, the lower port is blocked, and water is supplied from the upper two ports, which mixed with the liquid inside the burner through the transpiring wall, and then discharged through the bottom outlet.

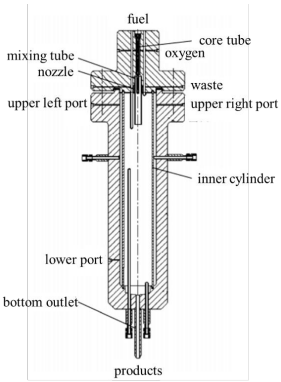

Fig. 2. Xi'an Jiaotong University multi-function reactor[17]

Shandong University also designed a 1.8L transpiring wall reactor which can be seen in Zhang et al[5] for hydrothermal combustion experiments. The reactor they designed was similar to the reactor at ETH. Using a retaining ring, the porous wall is divided into two zones, and the transpiring water can pass through the transpiring wall at different temperatures and flow rates. In addition, the fuel, the oxygen and the auxiliary heating fluid were injected from the coaxial nozzle, and therefore the oxidation coefficient and fuel concentration can be changed at any time during the experiment. Zhang used the reactor to test the ignition temperature and the extinction temperature under different flows conditions.

3 Characterization of hydrothermal flame processes

3.1 Ignition temperature

Ignition temperature is the lowest temperature at which a hydrothermal flame ignites at a certain supercritical pressure and fuel concentration. Some scholars have conducted experimental studies on the relationship between pressure and ignition temperature. As shown in figure 3 and figure 4, Schilling[2] used a semi-batch reactor to measure the ignition temperature of methane at different pressures. The fuel was 30mol% of methane, and the oxidant was pure oxygen. It was found that when the pressure increased from 20 MPa to 100 MPa, the ignition temperature was reduced just from 420 ° C to 400 ° C. Steinle[18] also studied the ignition temperature of 30mol% methane in a semi-batch reactor, but he used air as an oxidant and found that when the pressure increased from 32

MPa to 100 MPa, the ignition temperature decreased from 420 ° C to 395 ° C. Hirth[19] used a semi-batch reactor to measure the ignition temperature of different concentrations of methane at different pressures. The fuel was methane and the oxidant was pure oxygen. It was found that the pressure increased from 30 MPa to 100 MPa and 30mol% methane ignition temperature was reduced from 425 ° C to 390 ° C. The results of the three scholars had shown that the increase in pressure is conducive to the reduction of the ignition temperature.

The scholars also conducted an experimental study on the relationship between the concentration of fuel and the ignition temperature. Hirth found that if the pressure was unchanged at 60 MPa, the methane concentration increased from 10mol% to 30mol%, and the ignition temperature was reduced from 500 °C to 410 ° C; if the holding pressure was unchanged at 73 MPa, the methane concentration was increased from 5mol% to 20mol%, and the ignition temperature decreased from 450 ° C to 350 ° C. Steeper[8] studied the ignition characteristics of not only methane, but also methanol. Using pure oxygen as the oxidant, he found in a semi-batch reactor at a reaction pressure of 27.5 MPa, when methane was increased from 5mol% to 12mol%, the ignition temperature decreased from 480 °C to 380 °C; when methanol was increased from 6mol% to 36mol%, the ignition temperature decreased from 475 ° C to 405 ° C. The experimental results of Sobhy[9] showed that under the condition of 23 MPa, air as an oxidant, the concentration of methanol increased from 11.2 mol% to 32.3 mol%, and the ignition temperature decreased from 400 °C to 350 °C. Experiments conducted by Reddy[20] showed that under the pressure of 22.5 MPa, air as an oxidant, the concentration of n-propanol increased from 0.7mol% to 1.9mol%, and the ignition temperature decreased from 360 °C to 330 °C. Ren[21] found that the ignition temperature of 8wt% quinolone is 425 °C in a batch reactor and it decreased to 400 °C when the quinolone increased to 10wt%. It can be seen that the ignition temperature decreases as the fuel concentration increases, and the ignition temperature of methane is lower than that of methanol. In addition, materials of large molecular weight can be ignited at low molar concentrations.

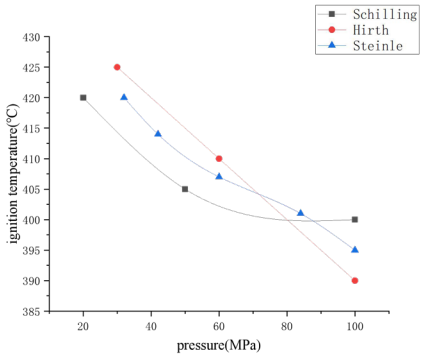

Fig. 3. Relationship between ignition temperature and pressure of 30mol% methane

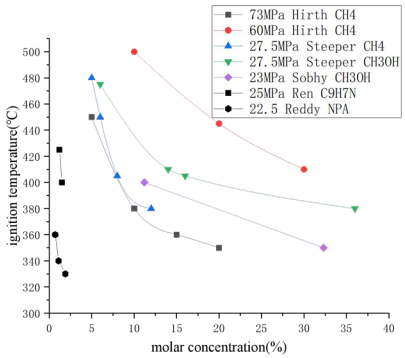

Fig. 4. Relationship between ignition temperature and fuel concentration (semi-batch reactor and batch reactor)

Other scholars have done experiments on the ignition characteristics of continuous reactors. As shown in Figure 5, experiments by Narayanan[22] who used WCHB-3 showed that the ignition temperature of 7.1mol% methanol was 452 °C under the condition of 25 MPa and pure oxygen as the oxidant. The experiment by Weber[23] who used WCHB showed that under the condition of 25 MPa and pure oxygen as the oxidant, ignition temperature of 10mol% methanol was 520 °C. Experiments conducted by the WCHB of Prikopsky[11] showed that 9.7mol% of methanol had an ignition temperature of 410 ° C to 430 ° C when pure oxygen was used as the oxidant. Wellig[10] used the TWR to test the ignition temperature of methanol. Under the condition of 25 MPa, while the oxidant was pure oxygen, the methanol concentration was increased from 9.7mol% to 12.3mol%, and the ignition temperature is decreased from 490 °C to 460 °C. Zhang[5] used the TWR to measure the ignition temperature of methanol. The oxidant used was oxygen. At 23 MPa, the ignition temperature of methanol at 4.2mol% was 600 °C, and the ignition temperature decreased to 460 °C at 7.0mol%. Bermejo[14] conducted supercritical hydrothermal combustion experiments in a tubular reactor showed that 1.2mol% of isopropanol had an ignition temperature of 450 ° C when air was used as the oxidant. Serikawa[24] conducted experiments with supercritical hydrothermal combustion in a pilot scale continuous reactor showed that at 25 MPa, air as an oxidant, 2mol% of isopropanol had an igniting temperature of 470 °C. Wellig[13] experimental results on the TWR showed that 9.7mol% methanol ignition temperature was 472-490 °C, pure oxygen as an oxidant.

It can be seen that a lower IPA concentration can ignite at 450 ° C comparing with methanol and the ignition temperature of the WCHB and that of the TWR have no obvious boundaries. In fact, because of the experimental conditions and equipment differences between experiments conducted by various scholars, it is not meaningful to uniformly compare the ignition temperature. In addition, different injection flow rates will also affect the ignition temperature.

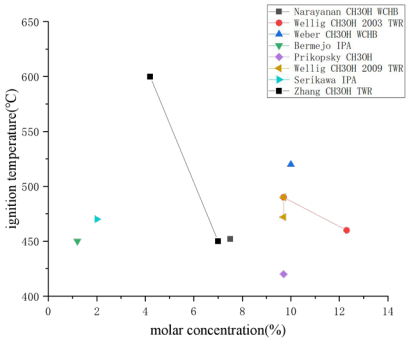

Fig. 5. Relationship between ignition temperature and fuel concentration (continuous reactor)

3.2 Extinction temperature

The extinction temperature in supercritical hydrothermal combustion means the minimum injection temperature of the fuel capable of maintaining hydrothermal flame when a hydrothermal flame has already been generated in the reactor. Scholars often study ignition characteristics and extinction characteristics simultaneously in experiments. The study of extinction temperature can only be carried out in the continuous reactor. As shown in Figure 6, the experimental results of Wellig's TWR[10] show that under the condition of 25MPa and pure oxygen as the oxidant, 7.1mol% of the methanol extinction temperature was 373 °C, and when the methanol concentration increased to 17.2mol%, the extinction temperature decreased to 100 ° C. Another set of experiments by Wellig[13] showed that when the methanol concentration under the same conditions increased from 3.5mol% to 20.2mol%, the extinction temperature decreased from 444 °C to 25 °C, and the fuel can be injected at ambient temperature to keep the hydrothermal flame from extinguishing. The supercritical hydrothermal combustion experiment of WCHB of Weber[25] shows that under 25MPa, pure oxygen is used as oxidant, when the methanol concentration increased from 2.3mol% to 15.8mol%, and the extinction temperature decreased from 550°C to 100°C. Zhang's TWR[5] measured that under 23MPa with pure oxygen as oxidant, methanol concentration increased from 4.2mol% to 7mol%, and the extinction temperature decreased from 405°C to 301°C. It can be seen that under the same conditions, the extinction temperature decreases as the fuel concentration increases, and the temperature can drop to ambient temperature. The form of the reactor (TWR and WCHB) has little effect on the extinction temperature.

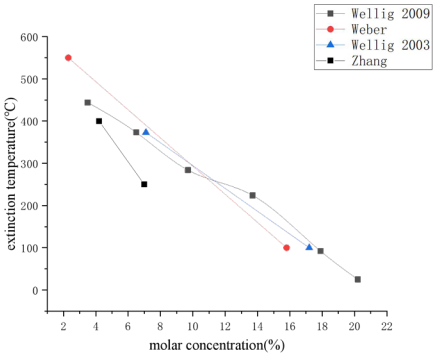

Fig. 6. Relationship between extinction temperature and fuel concentration

3.3 Other flame characteristics

In addition to studying the ignition characteristics and extinction characteristics, scholars have also studied other flame Characteristics, such as the flame height and the luminance. The intermittent experimental study by Schilling[2] shows that the increase of pressure will increase the flame height. Under the condition of pure oxygen as oxidant and 30mol% methane as fuel, the flame height will increase from 1.2 mm at 30 MPa to 3.7 mm at 200 MPa, and the diameter is kept constant at 0.5 mm. The experiment done by Pohsner[26] under similar conditions with Schilling shows that at 97 MPa, the flame height is 2 mm and the diameter is 0.7 mm. He estimated that flame height was related to the nozzle diameter and pressure of the reactor. Serikawa[24] used a pilot scale continuous reactor to carry out hydrothermal combustion experiments of isopropanol. It was found that at 25 MPa, 6mol% of isopropanol showed a light blue color at a 1.1 times oxidation coefficient, and the maximum temperature was 830 ° C, while at 2.2 times the oxidation coefficient, the flame is red and the maximum temperature rises to 1100 °C.

3.4 Destruction efficiency

Scholars also studied the destruction efficiency of organic matter in a supercritical hydrothermal combustion environment. For methanol and methane, Roche[27] found that removal rate in WCHB was between 80% and 96%, while the residence time was 20ms-50ms, and the flame temperature was 900-1100 °C. Wellig[10] found that the removal rate of methanol in TWR exceeded 99.8%, and the residence time was 50ms-100ms. Príkopský[11] found that the removal rate of methanol in the third generation TWR is 97.85%-99.99%. For isopropanol, Bermejo[14] found that at 450-500 ° C, as the residence time was less than 0.4 s in continuous reactor, the hydrothermal flame ignited and the TOC removal rate was more than 99%. Sato[28] found that the removal rate of isopropanol in continuous reactor at 25 MPa reached 99.98%. Serikawa[24] of Japan conducted a hydrothermal combustion experiment of dioxins and hexanes with a continuous reactor of pilot plant under conditions of 25MPa and air as the oxidant. Experimental result shows that the removal rate of dioxins is higher than 99.9%. Sobhy[9] used a semi-batch reactor at 25 MPa and the oxidant was air for hydrothermal combustion experiments, and found that the conversion of naphthalene and methanol was as high as 99.9%. Cabeza[29] used a tubular reactor to carry out hydrothermal combustion experiments to destroy acetic acid and ammonia respectively and isopropanol was used as fuel. It was found that the TOC removal

rate of acetic acid and isopropanol was as high as 99% at temperatures above 750 °C, and the TOC removal rate of ammonia and isopropanol reached 99%, but the maximum TN removal of ammonia was never higher than 92%. In another experiment, Cabeza[15] used the WCHB for hydrothermal combustion experiments to destroy ammonia, while the temperature was higher than 600 °C and isopropanol was used as an auxiliary fuel. It was found that the TOC removal rate was up to 99.99%, and the conversion rate of ammonia nitrogen is higher than 99.9%. If the supercritical hydrothermal combustion experiment of sludge is carried out with isopropanol as an auxiliary fuel, the TOC removal rate is as high as 99.5%. It can be seen that under the condition of supercritical hydrothermal combustion, the removal rate of refractory organic matter is extremely gratifying.

Table 1. Removal rate of organic matter under supercritical hydrothermal combustion conditions.

Author	Source	Types of reactor	Organic matter	Removal rate
Roche	[27]	WCHB	Methanol and methane	80%-96%
Wellig	[10]	TWR	Methanol	> 99.8%
Príkopský	[11]	TWR	Methanol	97.85%-99.99%
Bermejo	[14]	Tubular reactor	Isopropanol	> 99%
Sato	[28]	Tubular reactor	Isopropanol	99.98%
Serikawa	[24]	Tubular reactor	Dioxins and hexanes	> 99.9%
Sobhy	[9]	Semi-batch reactor	Naphthalene and methanol	99.90%
Cabeza	[29]	Tubular reactor	Acetic acid and isopropanol	99%
			Ammonia and isopropanol	99%
Cabeza	[15]	WCHB	Isopropanol and ammonia	99.99%
			Isopropanol and sludge	99.50%

It can be seen from table 1 that under the conditions of supercritical hydrothermal combustion, the removal rate of most organic matters is above 99% regardless of the reactor. The refractory organics can be ignited by mixing with the fuel to increase the removal rate.

4 Conclusion and outlook

The continuous reactor designed in each organization is very sophisticated, which can avoid the two major problems of reaction in the supercritical state: salt precipitation and corrosion. The ignition temperature decreases as the pressure increases and the fuel concentration increases. The extinction temperature decreases as the fuel concentration increases. The increase in pressure will result in the increase in the height of the flame. The increase in the oxidation coefficient results in the increase in flame temperature and the change in flame colour. The removal rate of different organic matters was also summarized under supercritical hydrothermal combustion, and the removal rate of more than 99% was basically achieved.

Although the TWR and WCHB designed by various organizations are able to avoid the two major problems in SCWO, the industrial applications now just use tubular reactors which cannot avoid the problems mentioned earlier. How to promote the TWR and WCHB into industrial applications should be the focus of future study.

The supercritical hydrothermal combustion experiments carried out by most scholars are using alcohol fuels, and the advantages of supercritical hydrothermal combustion removing refractory organic matters are not demonstrated. The interaction between the refractory organic matter and fuel in supercritical hydrothermal combustion is also the focus of future study.

5 Acknowledgement

This research is supported by the Fundamental Research Funds for the Central Universities [xjj2018201] and [xjj2018006], the Projects from National Natural Science Foundation of China [51871179].

References

1. E.U. Franck, Fluids at high pressures and temperatures. J. Chem. Thermodyn. **19**, 225–242, (1987)
2. W. Schilling, E.U. Franck, Combustion and Diffusion Flames At High Pressures To 2000 Bar. Physical Chem. Chem. Phys. **92**, 631–636, (1988)
3. M. Modell, Supercritical Water : Testing Reveals New Process Holds Promise. Solid Waste Manag. **25**, 26–28,30,76, (1982)
4. H. Ma, Fundamental Research on Power-Generating System Coupling of Gasification and Hydrothermal Combustion of Coal in Supercritical Water. Xi'an Jiaotong University .(2013)
5. F. Zhang, Y. Zhang, C. Xu, S. Chen, G. Chen, C. Ma, Experimental Study on the Ignition and Extinction Characteristics of the Hydrothermal Flame. Chem. Eng. Technol. **38**, 2054–2066, (2015)
6. C. Augustine, J.W. Tester, Hydrothermal flames: From phenomenological experimental demonstrations to quantitative understanding. J. Supercrit. Fluids. **47**, 415–430, (2009)
7. S.N. Reddy, S. Nanda, U.G. Hegde, M.C. Hicks, J.A. Kozinski, Ignition of hydrothermal flames. RSC Adv. **5**, 36404–36422, (2015)
8. R.R. Steeper, S.F. Rice, M.S. Brown, S.C. Johnston, Methane and methanol diffusion flames in supercritical water. J. Supercrit. Fluids. **5**, 262–268, (1992)
9. A. Sobhy, I.S. Butler, J.A. Kozinski,. Selected profiles of high-pressure methanol-air flames in supercritical water. Proc. Combust. Inst. **31 II**, 3369–3376, (2007)
10. B. Wellig, Transpiring wall reactor for supercritical water oxidation. Swiss Federal Institute of Technology Zurich. (2003)
11. K. Príkopský, Characterization of continuous diffusion flames in supercritical water. Swiss Federal Institute of Technology Zurich. (2007)
12. T. Meier, P. Stathopoulos, P. Rudolf von Rohr, Hot surface ignition of oxygen–ethanol hydrothermal flames. J. Supercrit. Fluids. **107**, 462–468, (2016)

13. B. Wellig, M. Weber, K. Lieball, K. Príkopský, P. Rudolf von Rohr, Hydrothermal methanol diffusion flame as internal heat source in a SCWO reactor. J. Supercrit. Fluids. **49**, 59–70, (2009)
14. M.D. Bermejo, P. Cabeza, M. Bahr, R. Fernández, V. Ríos, C. Jiménez, M.J. Cocero, Experimental study of hydrothermal flames initiation using different static mixer configurations. J. Supercrit. Fluids. **50**, 240–249, (2009)
15. P. Cabeza, J.P. Queiroz, S. Arca, C. Jiménez, A. Gutiérrez, M.D. Bermejo, M.J. Cocero, Sludge destruction by means of a hydrothermal flame. Optimization of ammonia destruction conditions. Chem. Eng. J. **232**, 1–9, (2013)
16. M.D. Bermejo, P. Cabeza, J.P.S. Queiroz, C. Jiménez, M.J. Cocero, Analysis of the scale up of a transpiring wall reactor with a hydrothermal flame as a heat source for the supercritical water oxidation. J. Supercrit. Fluids. **56**, 21–32, (2011)
17. Y. Li, S. Wang, M. Ren, J. Zhang, D. Xu, L. Qian, P. Sun, Recent advances on research and application on supercritical hydrothermal combustion technology. Chem. Ind. Eng. Prog. **35**, 1942–1955, (2016)
18. J.U. Steinle, E.U. Franck, High-Pressure Combustion - Ignition Temperatures To 1000 Bar. Berichte Der Bunsen-Gesellschaft-Physical Chem. Chem. Phys. **99**, 66–73. (1995)
19. T. Hirth, E.U. Franck, Oxidation and Hydrothermolysis of Hydrocarbons in Supercritical Water at High Pressures. Berichte der Bunsengesellschaft für Phys. Chemie. **97**, 1091–1097, (1993)
20. S.N. Reddy, S. Nanda, U.G. Hegde, M.C. Hicks, J.A. Kozinski, Ignition of n-propanol-air hydrothermal flames during supercritical water oxidation. Proc. Combust. Inst. **36**, 2503–2511, (2017)
21. M. Ren, S. Wang, C. Yang, H. Xu, Y. Guo, D. Roekaerts, Supercritical water oxidation of quinoline with moderate preheat temperature and initial concentration. Fuel. **236**, 1408–1414, (2019)
22. C. Narayanan, C. Frouzakis, K. Boulouchos, K. Príkopský, B. Wellig, P. Rudolf von Rohr, Numerical modelling of a supercritical water oxidation reactor containing a hydrothermal flame. J. Supercrit. Fluids. **46**, 149–155,(2008)
23. M. Weber, Apparate einer SCWO-Anlage und deren Leistungsfähigkeit. Swiss Federal Institute of Technology Zurich. (1997)
24. R.M. Serikawa, T. Usui, T. Nishimura, H. Sato, S. Hamada, H. Sekino, Hydrothermal flames in supercritical water oxidation: Investigation in a pilot scale continuous reactor. Fuel. **81**, 1147–1159, (2002)
25. M. Weber, C. Trepp, Required fuel contents for sewage disposal by means of supercritical wet oxidation (SCWO) in a pilot plant containing a wall cooled hydrothermal burner (WCHB). Process Technol. Proc. **12**, 565–574, (1996)
26. G.M. Pohsner, E.U. Franck, Spectra and temperatures of diffusion flames at high pressures to 1000 bar. Physical Chem. Chem. Phys. **98**, 1082–1090, (1994)
27. H.L. Roche, Wandgekühlter Hydrothermal-Brenner (WHB) für die überkritische Nassoxidation. Swiss Federal Institute of Technology Zurich. (1996)
28. H. Sato, S. Hamada, R.M. Serikawa, T. Nishimura, T. Usui, H. Sekino, Continuous flame oxidation in supercritical water. High Press. Res. **20**, 403–413, (2001)
29. P. Cabeza, M.D. Bermejo, C. Jiménez, M.J. Cocero, Experimental study of the supercritical water oxidation of recalcitrant compounds under hydrothermal flames using tubular reactors. Water Res. **45**, 2485–2495, (2011)

Material screening for two-step thermochemical splitting of H_2S using metal sulfide

Osahon Osasuyi[1], *Khalid* Al-Ali[1,2*], *Mohammad* Abu Zahra[1,2], *Giovanni* Palmisano[1], and *Dang* Viet Quang [1]

[1]Department of Chemical Engineering, Khalifa University, Masdar Institute, Masdar City, P.O. Box 54224, Abu Dhabi, The United Arab Emirates.

[2]Center for Catalysis and Separation, Khalifa University of Science and Technology, P.O. Box 127788, Abu Dhabi, United Arab Emirates

Abstract. Associated with the rise in energy demand is the increase in the amount of H_2S evolved to the environment. H_2S is toxic and dangerous to life and the environment, thus, the need to develop efficient and cost-effective ways of disposing of the H_2S gas has become all-important. To this end, a two-step thermochemical H_2S splitting cycle is proposed in this work which does more than just getting rid of the toxic gas but has the potential to produce valuable H_2 gas as well as store the solar heat energy. Studies have proved that the type of material used, such as metal sulfides, is critical to the efficiency of this thermochemical splitting process. As follows, this study focuses on establishing a criterion to aid in selecting favorable metal sulfides for application and further development in the H_2S thermochemical decomposition sphere. Using a computational approach, via the HSC Chemistry 8®, evaluations such as the equilibrium yield from the sulfurization and decomposition reaction steps, the temperature required for reaction spontaneity, and the Reversibility Index were determined. Investigations proved that sulfides of Zirconium, Niobium, and Nickel were auspicious candidates for the thermochemical decomposition.

Introduction

Hydrogen sulfide, which is naturally present in crude oil and natural gas, is toxic and considered as a contaminant to the environment. Hydrogen sulfide is usually removed from petroleum products through the refining of crude oil and sweetening of sour natural gas. The rise in the global energy demand thereby poses a challenge because meeting this demand would require increased use of fossil fuels [1], ultimately leading to a rise in the amount of H_2S evolved to the environment [2].

Researchers and corporations have put in a lot of work to bring about ways to reduce these H_2S emissions. The Claus Process, which is the state of the art approach for disposing of noxious H_2S, involves the thermal decomposition of H_2S by partial oxidation to produce

* Corresponding author: khalid.alali@ku.ac.ae

sulfur and water. This process releases a great deal of energy in the form of low-grade steam, which has relatively low economic value. However, the thermolysis of the noxious H_2S provides a realizable means of deriving higher economic benefits, as hydrogen is simultaneously generated during this process [3]. This reaction is endothermic having a potential for improving energy efficiency through storage of heat in the form of Hydrogen production. The H_2 produced can be used in the synthesis of new products, hydrodesulfurization and hydrocracking processes, and as a fuel source. The reaction for the thermal splitting is shown below [4]:

$$H_2S\,(g) \;\leftrightarrows\; H_2(g) + {}^{1}/_{2}\,S_2\,(s) \qquad \Delta G° = 33.3\ kJ/mol \quad \Delta H° = 20.4\ kJ/mol \qquad (1)$$

The technical challenge with producing H_2 from H_2S is that the direct reaction of H_2S decomposition to elemental sulfur is endergonic, thus its equilibrium for the reaction is unfavourable at all temperatures. Therefore, this process will require free-energy input, e.g. from heat recovery systems of from the sun, to drive the overall reaction.

To attain higher conversions using realistic reactor sizes and residence times, catalysts are generally applied to accelerate this kinetically limited process [5-11]. However, the thermodynamic forces of the thermolysis process are unaffected by the catalysts and strongly limits the overall process. The equilibrium H_2S conversion is about 6 % at 800˚C under at atmospheric pressure [12], which is too low for an economically viable process. To overcome this thermodynamic limitation, studies were carried out using catalytic membrane reactors [13-14]. Despite the fact that very high conversions were obtained using these membrane reactors, the high cost of implementation accompanying this method, via the application of metallic hydrogen-permeable membranes, makes it unfavorable.

In the pursuit to establish a comparatively cheap means of attaining high conversions of H_2, a two-step thermochemical closed cycle using metal sulfides was adopted in this work. The thermochemical approach was used to devise a sequence of easier reaction steps to accomplish the overall reaction of H_2S decomposition. The first step of the H_2S decomposition cycle involves a metal sulfide (MeS_{low}) sulfurization under H_2S atmosphere. This reaction is usually exothermic and takes place at lower temperatures. While the second step involves a regeneration of the metal sulfide (MeS_{low}) under high-temperature conditions. The cyclic reaction is derived from the Kiuchi-type 1 reaction as shown in the figure below [15]:

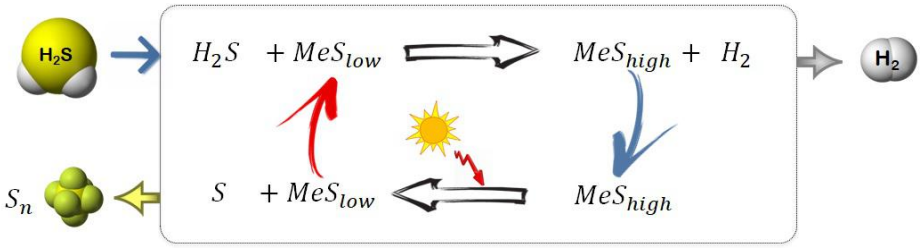

Fig. 1. Two-step thermochemical H_2S splitting cycle

The type of metal sulfides used for the H_2S splitting cycle is very crucial to process' efficiency [15-20]. A lot of work has been carried out on the direct thermal splitting of H_2S. However, just a few metal sulfides have been done using the two-step thermochemical splitting approach of H_2S and without any nomination basis for these metal sulfides used for the experimental studies. As such, the objective of this study is to identify the most promising candidates (metal sulfides) for the two-step thermochemical H_2S splitting cycle, which can aid in the provision of data and insight for further research and application.

Methodology

A systematic approach has been developed to achieve a successful material screening process regarding the thermochemical splitting of H_2S. This activity was broken down into a series of steps:

A) Identification of stable/predominant metal sulfides

First, identification of predominant and stable metal sulfides which exists at the specified operating conditions was carried out. In addition to acquiring information on the lower metal sulfides and higher metal sulfides that can be used for further analysis, knowledge on the metal sulfide reaction systems which have only one stable phase is obtained. These single-stable phase sulfides are not suitable for the two-step thermochemical cycle. Thus, this process helped in sieving out unsuitable metals prior to any further investigations.

A quick estimate of the phase stability of these metal sulfides was determined computationally using the Temperature-Partial Pressure (TPP) module of the HSC Chemistry 8.0®. Since thermodynamic stability occurs when a system is in its lowest energy state, the module aided in determining the phase stability based on the minimum Gibbs energy.

Identification of the stable higher sulfide phase was executed under isothermal conditions (25˚C), with the partial pressures of H_2 and H_2S ranging from 0.1 to 1 bar. During the regeneration step, H_2S and H_2 are not present, thus, the assumption that the partial pressures of these components tend to zero. Identification of the stable lower sulfide phase was carried out under isothermal conditions (800˚C), with the partial pressures of S_2 ranging from 0.1 to 1 bar.

B) Thermodynamic parameters determination

The predominant lower and higher metal sulfide phases recognized in the previous step was then applied in the Reaction Equation module of the HSC Chemistry 8.0® to determine thermodynamic properties describing the state of the heterogeneous reaction systems. The Enthalpy, Entropy, and Gibbs free energy were determined, providing more insight into the nature of the two-step cycle. The required input is the stoichiometric reaction equation for the sulfurization and regeneration reactions of the thermochemical H_2S splitting cycle at the appropriate operating conditions.

C) Equilibrium amount of reaction products

The multi-component equilibrium compositions for the reaction system were determined using the Equilibrium module of the HSC Chemistry 8.0®. The GIBBS solver, which makes use of the Gibbs energy minimization method, was applied via the Equilibrium module to calculate equilibrium amounts of reaction products using previously determined thermodynamic parameters. This was used to determine the equilibrium amount of the H_2 evolved and higher metal sulfide produced in the first sulfurization step, and the equilibrium amount of sulfur evolved and lower metal sulfide regenerated in the second step of the thermochemical H_2S splitting cycle.

To achieve accurate equilibrium results, the potentially stable phases for the heterogeneous system must be considered. This was achieved in the first step using the Phase Stability Diagram module. The appropriate number of moles of raw materials for the reaction was considered, estimated stoichiometrically, using a basis of 1 kmol. The

temperature for the two-step reaction of the thermochemical cycle was set at 25˚C for the sulfurization step, and 800˚C for the regeneration step, under isobaric conditions of 1 bar.

Aided by the three steps above, key parameters, as shown in Fig. 2, were determined to serve as performance yardsticks to guide in the selection of metal sulfides for the H_2S thermochemical splitting cycle:

- Phase stability at operating conditions.
- The yield of Hydrogen and higher metal sulfide produced.
- The yield of Sulfur and lower metal sulfide produced.

$$Percent\ Yield(\%) = \frac{Actual\ Yield}{Theoretical\ Yield} \times 100 \quad (2)$$

- Temperature requirement for reaction spontaneity
- Reversibility Index (RI)

$$\mathrm{RI} = \frac{moles\ of\ \ MeS_{low}\ \ produced\ in\ regeneration\ reaction}{Initial\ moles\ of\ \ \ MeS_{low}\ \ \ reacting\ in\ sulfurization\ reaction} \quad (3)$$

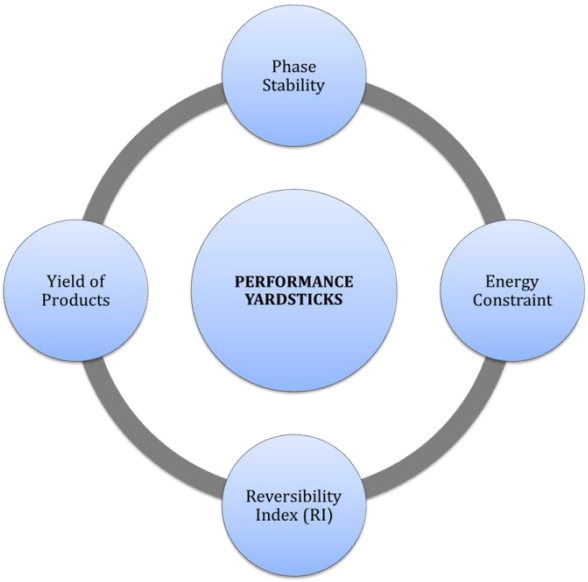

Fig. 2. Evaluation criteria for selection of metal sulfides

Results and discussion

Table 1 displays a list of the stable lower and higher metal sulfides at the reaction operating conditions. A total of 27 metals were tested, however, only the sulfides listed were used for performance analysis. Most of the metals tested were transition metals due to the favorable bonding interactions that exist between their d-orbitals and the p-orbitals of sulfur, along with their potential to form multiple oxidation states. Among the 27 metals tested, the following displayed a single-phase metal sulfide stability under the cyclic reaction conditions and did not qualify for any further inquiry: MoS_2, Cu_2S, ZnS, MnS, Li_2S, RuS_2,

CdS, MgS, Rb_2S, Cs_2S, and Al_2S_3. The bonding interactions, such as the metal-sulfur bond strength, is a major factor that brings about the single stable phase occurrence. For example, metal sulfides like ZnS have very low adsorption bonding with the sulfur atoms from H_2S, which prevents the progress of the sulfurization reaction.

Table 2. Stable Higher and Lower Metal Sulfides at Operating Conditions.

Metal	Higher Metal Sulfide (MeS_{high}) at 25˚C	Lower Metal Sulfide (MeS_{low}) at 800˚C
Sc	ScS_3	ScS
Ti	TiS_2	TiS
V	V_2S_3	$VS_{1.043}$
Cr	Cr_2S_3	$CrS_{1.17}$
Fe	FeS_2	FeS
Co	CoS_2	CoS
Ni	NiS_2	NiS
Zr	ZrS_3	ZrS_2
Nb	NbS_2	$NbS_{1.65}$
Tc	Tc_2S_7	TcS_2
Rh	Rh_2S_3	Rh_3S_4
Pd	PdS	Pd_4S
Ir	IrS_2	Ir_2S_3
Hf	HfS_3	HfS_2
Na	Na_2S_2	Na_2S
K	K_2S_2	K_2S

It is important to note that some of the metal sulfides listed in Table 1 have more than one stable sulfide that exists at a given state for both the sulfurization and regeneration operating conditions. As a case in point is the Ni-S binary reaction system. These sulfides exist in several thermodynamically stable sulfide states that are potentially functional for the cyclic H_2S splitting reaction. Some of the nickel sulfide phases include Ni_3S_2, Ni_7S_8, Ni_9S_8, NiS, Ni_3S_4, NiS_2. In this thermodynamic study, NiS and NiS_2 were applied as shown in Table 1. NiS_2 was used as the higher metal sulfide state existing after the sulfurization reaction, because of the tendency for it to be easily regenerated as compared to other nickel sulfides with lower sulfur content. This does not necessarily mean that these nickel sulfide

phases (NiS-NiS_2), as seen in Table 1, are the most favorable pair of nickel sulfide states that can be applied for the H_2S splitting cycle.

As shown in the Fig. 3, most of the metal sulfide reaction systems generated a high yield of hydrogen due to the exergonic nature of the sulfurization reaction which takes place at 25˚C and at 1 bar. Thus, the sulfurization of the metal sulfides occurs spontaneously in most cases. Only the Hf-H-S reaction system revealed to be endergonic under the specified operating conditions, attributing to the relatively low yield achieved when reacting 1 kmol of Hafnium Sulfide with H_2S. The sulfurization reaction of HfS_2 has ΔG of 1.486 kJ. In all cases, the sulfurization reaction of the lower metal sulfides was exothermic, thereby increasing the temperature would cause a decrease in the equilibrium conversion and yield of hydrogen.

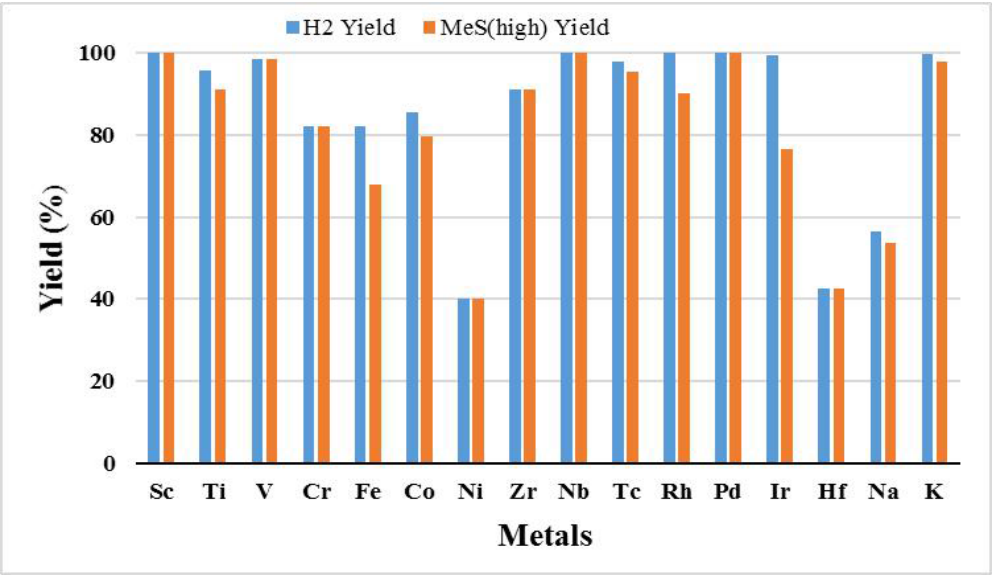

Fig. 3. The yield of hydrogen and higher metal sulfide generated at 25˚C for 1 kmol of H_2S

Studies in literature corroborate the findings presented in Table 1. Even though some of these metal sulfides are not suitable for the two-step thermochemical cycle, the nature of their stable existence in one-phase enables them to function as catalysts for the direct thermal dissociation of H_2S. A couple of sulfides in our study which fit the bill are Molybdenum sulfide and Lithium Sulfide. Investigations conducted by several researchers [5-7] revealed that the reaction of MoS_2 with H_2S doesn't generate its trisulfide under X-ray diffraction analysis. MoS_2 seems to be inert at temperatures below 500˚C but catalyzes the decomposition reaction at higher temperatures. At 500˚C, the H_2 yield for the H_2S thermal decomposition reaction increased from 6% to 8.5% when MoS_2 was introduced. Li_2S also proved to be a poor candidate for the two-step thermochemical cycle but a good catalyst for the direct thermal splitting of H_2S. After thermally splitting the H_2S over Li_2S at 550˚C, the metal sulfide remained unchanged, and there was an increase in H_2 yield from about 1% to 3% when compared to a non-catalytic thermolysis of H_2S [21].

On the other hand, more favorable candidates for two-step thermochemical cycles such as the monosulfides of Fe, Co, Ni, K, and Na have been verified in literature to show poor catalytic activity but rapidly reacts with H_2S to produce higher metal sulfides—disulfides specifically. Investigations by Chivers et al. [5] using Na_2S and K_2S for the sulfurization reaction were similar to Table 1, reacting with H_2S to produce Na_2S_2 and K_2S_2. At 600˚C, the H_2 yield for Na_2S and K_2S was 14% and 18% respectively.

In the regeneration step, the higher metal sulfide is thermally decomposed at 800˚C and 1 bar to produce its lower metal sulfide and elemental sulfur. The thermal decomposition efficiency is represented by the yield of the sulfur produced as well as the yield of the lower metal sulfide as shown in Fig. 4. For most reaction systems, the regeneration reaction is endergonic and endothermic at the 800˚C and 1 bar, hence, the operating conditions are not favorable for many metal sulfides. However, for the Zr-H-S, Hf-H-S, and Nb-H-S reaction systems, the thermal decomposition occurs spontaneously with ΔG of -35.87 kJ, -49.81 kJ, and -2.396 kJ respectively. Higher sulfides of Zirconium and Hafnium decomposed to produce a 100% yield of sulfur and their lower metal sulfides, while Niobium produced a yield of about 80%. Sulfides of Chromium and Technetium also showed relatively great results for the decomposition reaction. However, the use of Technetium isn't favorable due to its radioactive nature.

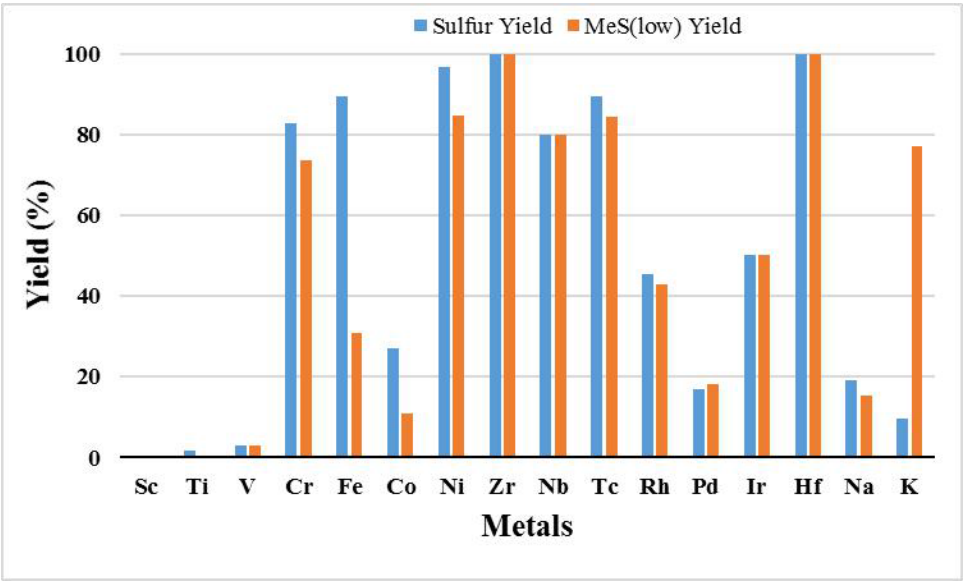

Fig. 4. The yield of sulfur and lower metal sulfide generated at 800˚C

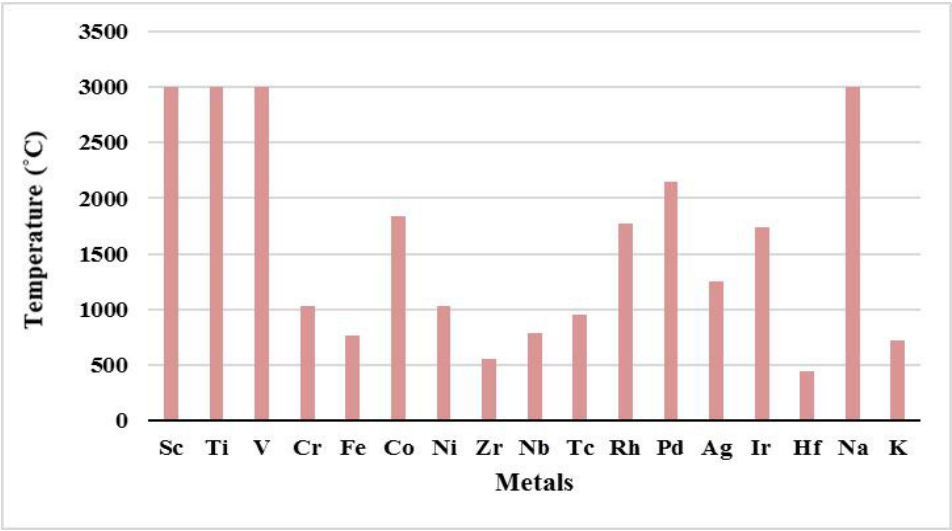

Fig. 5. Temperature requirement for reaction spontaneity

Figure 5 shows the temperature levels needed to attain reaction spontaneity in the regeneration process. When the temperature of the reaction is increased, the regeneration reaction, usually endothermic, can be transformed from an endergonic reaction to a spontaneous reaction. Sulfides of Zirconium, Hafnium, Niobium, Potassium, and Iron proved to have spontaneous regeneration reactions at temperatures below 800˚C, ultimately resulting in a relatively higher yield of sulfur and lower metal sulfide shown in Fig. 4. Additionally, these sulfides are more energy efficient as relatively lower temperatures can be operated successfully for the regeneration reaction.

The amount of sulfur and lower metal sulfide presented in Fig. 4 was estimated based on the assumption that a yield of 100% was derived for the generated higher metal sulfide in the sulfurization step, thereby rendering the maximum possible yield for the sulfur and lower metal sulfide in the regeneration step. However, a more accurate depiction of the Reversibility Index for the H_2S splitting thermochemical cycle would require the latter thermal decomposition reaction to be a function of the yield of the higher metal sulfide derived in the sulfurization reaction. A key parameter considered in evaluating the performance of a catalyst is the Regeneration performance. Likewise, the Reversibility Index measures the degree to which one can recover the material used for the H_2S decomposition reaction. As clearly shown in Fig. 6, the Zr-H-S reaction system displayed the best RI with a value of about 0.91. Sulfides of Technetium and Niobium showed good results with RI of about 0.8.

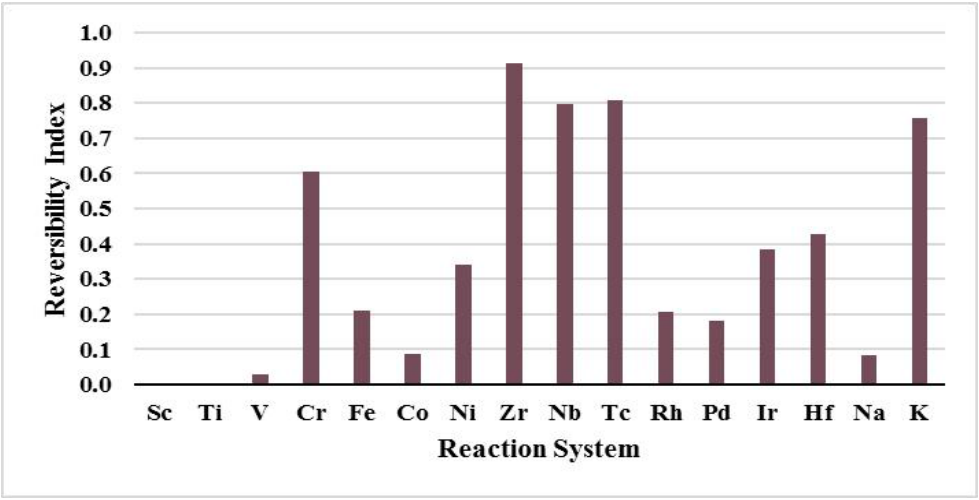

Fig. 6. Reversibility Index of Metal Sulfides

Conclusion

Following the computational activity executed in this study, some promising metal sulfides and relevant data have been identified, such as sulfides of Zirconium and Niobium, which can be applied and improved upon in the thermochemical H_2S decomposition field of study. These sulfides have a lot of potential for further research and development as they haven't been experimentally investigated for the H_2S decomposition process.

Sulfides of Nickel are uniquely promising because of the existence of several thermodynamically stable states that are functional for the H_2S splitting cycle. So, there's the possibility that even more favorable nickel sulfide pairs, than what was tested during the

material screening activity in this work, exists for the cyclic reaction. Moreover, nickel sulfides are relatively cheap and accessible, making it a good candidate for experimental investigations that would be carried in the future.

It is important to note that the yield for the products derived in this study is in the equilibrium state and doesn't truly reflect the actual conversions achieved in real reactors, which are dependent on the reaction kinetics and transport phenomena of the reactants. However, the equilibrium study in this work renders the maximum achievable amount, serving as a guide for the selection of materials, and a target for actual processes.

Finally, the experimental studies, using the favorable metal sulfides identified in this work, have begun to achieve a better understanding of the interplay between the thermodynamics and kinetics interactions associated with the two-step thermochemical decomposition of H_2S into Hydrogen production. Accomplishing this objective would also render some insights necessary for favorable process modifications and optimization in future projects.

This work is part of a one-to-one project ongoing between Masdar Institute, Part of Khalifa University of Science and Technology and Massachusetts Institute of Technology. This research is supported by the Government of Abu Dhabi to help fulfill the vision of the late President Sheikh Zayed bin Sultan Al Nahyan for sustainable development and empowerment of the UAE and humankind.

References

1. J. Conti, P. Holtberg, J. Diefenderfer, A. LaRose, J. T. Turnure, L. Westfall. No. DOE/EIA-0484 (2016)
2. R. H.Worden, P. C. Smalley, Chem. Geol., **133**, 157 (1996)
3. W. Villasmil, A. Steinfeld, Energy Convers. Manag., **51**, 2353 (2010)
4. J. Zaman, A. Chakma, Fuel process. technol., **41** (2), 159 (1995)
5. T. Chivers, J. B. Hyne, C. Lau, Int J Hydrogen Energy, **5**, 499 (1980)
6. T. Chivers, C. Lau, Int J Hydrogen Energy, **12**, 235 (1987)
7. K. Fukuda et al., Ind. Eng. Chem. Fundam., **17**, 243 (1978)
8. N. O. Guldal, H. E. Figen, S. Z. Baykara, Int. J. Hydrogen Energy, **40**, 7452 (2015)
9. N. O. Guldal, H. E. Figen, S. Z. Baykara, Chem. Eng. J., **313**, 1354 (2017)
10. A. L. Martínez-Salazar *et al.*, Int. J. Hydrogen Energy, **40**, 17354 (2015)
11. S. Megalofonos, N. Papayannakos, Appl. Catal., **165**, 249 (1997)
12. V. E. Kaloidas, N. G. Papayannakos, Int. J. Hydrogen Energy, **12**, 403 (1987)
13. D. J. Edlund, W. A. Pledger, J. Memb. Sci., **77**, 255 (1993)
14. K. Akamatsu, M. Nakane, T. Sugawara, T. Hattori, S. Ichi Nakao, J. Memb. Sci., **325**, 16 (2008)
15. H. Kiuchi, T. Iwasaki, I. Nakamura, T. Tanaka, ACS symposium series, **116**, 349 (1980)
16. H. Kiuchi, K. Funaki, Y. Nakai, T. Tanaka, Int. J. Hydrogen Energy, **9**, 701 (1984)
17. D. Berk, R. A. Heidemann, W. Y. Svrcek, L. A. Behie, Can. J. Chem. Eng., **69**, 944 (1991)
18. A. Pietro Reverberi, J. J. Klemeš, P. S. Varbanov, B. Fabiano, J. Clean. Prod., **136**, 72 (2016)

19. T. V. Reshetenko, S. R. Khairulin, Z. R. Ismagilov, V. V. Kuznetsov, Int. J. Hydrogen Energy, **27**, 387 (2002)
20. L. M. Al-Shamma, S. A. Naman, Int. J. Hydrogen Energy, **14**, 173 (1989)
21. T. Chivers, C. Lau, Int. J. Hydrogen Energy, **10**, 21 (1985)

Flexible hydrogen fuel cell fabricated on paper with embedded aluminium foil

Yifei Wang[1], Holly Kwok[1], Yingguang Zhang[1], Wending Pan[1], and Dennis Y.C. Leung[1,]*

[1]Department of Mechanical Engineering, the University of Hong Kong, Hong Kong, China

Abstract. Direct hydrogen fuel cells are generally heavy and rigid systems based on metal or plastic materials, which are not suitable for various miniwatt and flexible devices. In this study, we have developed a lightweight and flexible fuel cell based on paper substrate embedded with an Al foil inside, which is used as an in-situ hydrogen source by reaction with an electrolyte solution during operation. Benefited from the inhibited hydroxyl transportation by the porous cellulose network, the vigorous Al corrosion reaction is well controlled even though strong alkaline electrolyte is adopted, so that the fuel cell can be discharged for more than 5 hours at 1 mA cm^{-2} (0.83 V) with only 3.5 mg Al foil. The corresponding faradaic and energy efficiencies are as high as 72% and 18.3%, respectively. The fuel cell flexibility is also quite good when facing different bending angles. Considering its moderate power output, this flexible paper-based hydrogen fuel cell is especially suitable for powering various miniwatt and flexible devices, such as wearable electronics, biosensors, RFID tags, etc. However, higher power can be obtained by suitable stacking of the fuel cell.

1 Introduction

Fossil fuels such as coal, oil and natural gas are currently the mainstream energy source worldwide, which is however, not only resource limited but also generating pollution and damage to the environment. Compared with these hydrocarbon fuels, hydrogen fuel is a renewable energy carrier which can be produced through chemical, electrochemical or photocatalytic approaches, which is also pollution-free and carbon-neutral during consumption. Therefore, it is highly feasible and promising for the hydrogen cycle to replace the conventional carbon cycle as long as the associated technology develops, which will lead to a "hydrogen economy" in the future [1].

To utilize hydrogen, fuel cell is one of the most efficient devices which can convert the chemical energy in the hydrogen directly to electricity. Based on their electrolytes, fuel cell can be classified into many sub-types, including proton exchange membrane fuel cell (PEMFC), solid oxide fuel cell, alkaline fuel cell, phosphoric acid fuel cell, molten carbonate fuel cell, microfluidic (membraneless) fuel cell (MFC), etc. [2] Among them, the PEMFC receives great R&D attention especially in the transportation and portable application sectors. This is mainly because of its low temperature operation, high power

* Corresponding author: ycleung@hku.hk

output together with mature membrane electrolyte technology [3]. Nevertheless, to date, most of the PEMFCs are inflexible reactors based on metal or plastic framework and multi-layer cell configuration, which are not only heavyweight and complex, but also require sophisticated and expensive fabrication. These shortcomings may be tolerable for large systems such as electric vehicle, but are much less favorable for portable electronics, especially the flexible electronics. Therefore, great efforts have been made in the past decade to develop flexible fuel cells in order to expand the application prospect of this technology [4-13]. Tominaka et al. [10] fabricated a bendable fuel cell on cycloolefin polymer substrate by hot embossing. With methanol as fuel, this cell could generate a peak power density of 83 $\mu W\ cm^{-2}$. Weinmueller et al. [11] also designed a flexible methanol fuel cell on a thin polymer film of photosensitive SU-8. This time a much higher power density of 19 $mW\ cm^{-2}$ was achievable, and the cell functioned normally under both single radius bending condition and S-shape bending condition. Hsu et al. [7] embedded metal wires into carbon fibre bunches as a novel flexible current collector. The subsequent flexible PEMFC achieved similar performance to the conventional nonflexible cell with hydrogen fuel, which was also almost unaffected when facing different bending curvatures. Chang et al. [4-6] have done a series of work to develop flexible polydimethylsiloxane-based hydrogen PEMFC. Using Ag nano-wire percolation networks as current collector, their device could achieve even better power output at bending status than that of flat status, which was benefited from the decreased resistance originated from the increased compressive force normal to the membrane electrode assembly. In general, since the polymer electrolyte membrane is intrinsically flexible, the key issue for developing flexible PEMFC is to design flexible gas diffusion layer, current collector and bipolar plates.

Despite its research progress, the current PEMFC is generally high cost because of the expensive polymer electrolyte membrane (e.g. Nafion membrane). In addition, the membrane requires delicate water balance in order to maintain a normal and stable fuel cell operation, leading to sophisticated water management subsystem [14, 15]. Furthermore, even though the fuel cell itself is flexible, a bulky hydrogen storage unit and associated delivery tubing are still requisite, which will impair the flexibility of the whole system. Recently, a novel type of paper-based fuel cell (PBFC) is proposed, which employs the capillary action of cellulose paper to passively transport the aqueous electrolyte [16-20]. In this manner, the PBFC is not only cost-efficient and structurally-simple, but also highly flexible. Various fuels have been studied in the PBFC, including methanol [17], formate [16], glucose [18], hydrogen peroxide [19], etc. As for hydrogen, since paper is not a gas-tight material, a plastic shell is required to encapsulate the PBFC inside, which inevitably sacrifice the device flexibility [20]. In this work, we aim to develop a flexible hydrogen PBFC. To eliminate the necessity for hydrogen storage and to prevent the hydrogen from escaping, an Al foil was innovatively utilized and embedded inside the paper substrate as hydrogen source. The other fuel cell components were directly deposited onto the paper surface. In this manner, a low-cost, concise, lightweight and flexible fuel cell system was developed. To the best of our knowledge, this novel cell design has never been investigated before.

2 Experimental

2.1 Fuel cell design and fabrication

Unlike conventional rigid fuel cells based on either metal or plastic framework, the present flexible fuel cell was built entirely within a single piece of paper substrate. Fig. 1 (a) shows the schematic diagram of its working principle. A thin layer of Al was stored inside the

paper as hydrogen source, while the hydrogen oxidation reaction (HOR) anode and oxygen reduction reaction (ORR) cathode were directly deposited onto the opposite side of the paper surface. During operation, an alkaline electrolyte solution was provided and wicked into the paper substrate by capillary action. The Al layer would react with the electrolyte to generate H_2 for the anode side, while O_2 from the ambient air was utilized by the cathode side. Consequently, electricity can be generated continuously until the Al layer is exhausted. Fig. 1(b) illustrates the exploded view of the present flexible fuel cell. First of all, an Al foil (kitchen foil, 98.3% purity, 1cm x 1cm) was embedded inside a piece of home-made paper during the paper-making process. Next, two 5x5 Ag grids (1 cm^2 total area) were drawn on opposite sides of the paper, which covered exactly the Al foil inside. They were also connected to Cu tape ends for external connection. Afterwards, the anode and cathode catalyst inks were deposited onto corresponding grids by a pipette, respectively. For the anode side, the catalyst ink was composed of 50 mg Pt/C (Johnson Matthey, 60 wt.% Pt), 2.5 mg Nafion binder and 1 mL ethanol-water (1:1) solvent, which were sonicated for 30 min to achieve uniform distribution. For the cathode side, the catalyst ink was composed of 50 mg MnO_2/CNT (home-made by co-precipitation method [21], 60 wt.% MnO_2), 2.5 mg Nafion binder and 1mL ethanol-water (1:1) solvent, which were also sonicated for 30 min. For each cell, 40 µL of the anode ink and 20 µL of the cathode ink were deposited, respectively, leading to an anode catalyst loading of 1.2 mg cm^{-2} Pt and cathode catalyst loading of 0.6 mg cm^{-2} MnO_2. Here it is worth mentioning that Pt was temporarily utilized in this work in order to testify our flexible fuel cell concept first, which will be replaced by non-noble HOR catalysts such as Ni in our future work. After electrode deposition, a sealing tape was attached to the anode surface in order to isolate it from ambient air. Otherwise, a significant mix potential would be generated on the anode side, leading to fuel cell failure. The final prototype was 100 mg in weight and was highly flexible.

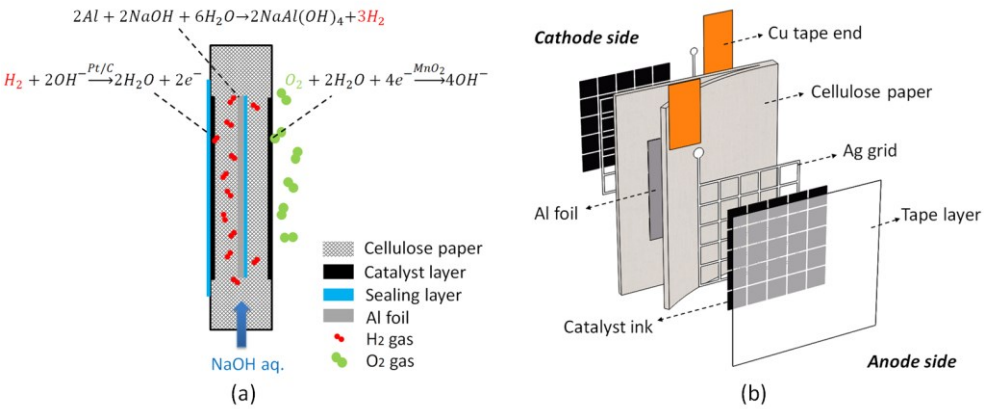

Fig. 1 Schematic diagrams of the flexible hydrogen PBFC: (a) Working principle; (b) Exploded view of the cell structure.

2.2 Fuel cell testing

The present fuel cell was tested with 3 M NaOH electrolyte. This concentration was used because a higher concentration would shrink the paper substrate and deform the deposited Ag grids and electrodes on it. The fuel cell was suspended vertically, with its Cu ends connected to an electrochemical work station (CHI 760E). Its paper end was contacted with 0.5 mL electrolyte solution to facilitate the capillary absorption process. Once the electrode

area was totally wetted, the fuel cell OCV was recorded until it reached a stable value. Afterwards, the fuel cell polarization curve was obtained by Linear Sweep Voltammetry (LSV) from OCV to 0 V, at a sweep rate of 5 mV s^{-1}. During the sweep, the cathodic potential was also recorded simultaneously by a multimeter, which was connected to both the fuel cell cathode and a reference electrode (Ag/AgCl in saturated KCl). The tip of the reference electrode was inserted into the electrolyte drop.

To investigate the fuel cell discharge stability and efficiency, galvanostatic dischage test was conducted at different current densities. With a specific amount of embedded Al (3.5 mg for a 1 cm^2 foil), both the faradaic efficiency and energy efficiency were calculated by the following equations, respectively.

$$\varepsilon_{faradaic} = \frac{iAt}{mC\delta} \tag{1}$$

$$\varepsilon_{energy} = \frac{V}{U} \cdot \varepsilon_{faradaic} \tag{2}$$

where ε is the efficiency, i is the discharge current density (mA cm^{-2}), A is the electrode area (cm^2), t is the discharge time (h), m is the mass of Al foil (0.0035 g), C is the Al specific capacity (2980 mA h g^{-1}), δ is the Al purity, V is the discharge voltage, and U is the theoretical voltage (2.7 V for Al).

3 Results & Discussion

3.1 Fuel cell performance

The OCV characteristic of the fuel cell was first studied after providing the alkaline electrolyte. As shown in Fig. 2(a), it took about 8 minutes before the OCV climbed to a steady value of 0.93 V. At the first 4 minutes, the OCV was even negative. Afterwards, the OCV encountered a gradual and stable rise up. This is due to the corrosion of Al that resulted in slow accumulation of H_2 gas inside the paper substrate. At the first 4 minutes, the concentration of H_2 was negligible, so that the remaining air inside the paper would cause an ORR potential on the anode side (same as the cathode side). Since Pt is more active for ORR than MnO_2, the anode ORR potential would be more positive than that of the cathode, leading to a negative OCV. During the next 4 minutes, the H_2 concentration kept increasing, so that the HOR potential started to dominate the anode side, leading to a gradually elevating OCV. The final value of 0.93 V was normal compared with those in the literature [22].

After stabilization of the OCV, the polarization curves of three cells were recorded and compared in Fig. 2(b). At the higher voltage region (above 0.6 V), the polarization curves were very straight and quite similar with each other, which were dominated by ohmic resistance. However, at the lower voltage region (below 0.6 V), the curves encountered a sharp drop and the differences between them was quite evident, probably due to the severe mass transport resistance. As shown in Fig. 2(c), this mass transport resistance was mainly from the anode side, indicating a starvation of H_2 at the lower voltage region. This H_2 starvation was quite random for each cell tested, so that the curve repeatability at lower voltage was not as good as that at higher voltage. In the following sections, an averaged polarization curve would be utilized. The averaged peak power density was 4 mW cm^{-2}, and the averaged maximum current density was 8 mA cm^{-2}. Therefore, the present flexible hydrogen PBFC is more suitable for miniwatt applications with low current drain.

Fig. 2(d) shows the battery discharge curves at current densities of 1, 2 and 5 mA cm^{-2}, with only 3.5 mg embedded Al foil as H_2 source. At 1 and 2 mA cm^{-2}, the discharge curves were very stable until a sudden stop due to the exhaustion of the Al. This result indicates that the generation of hydrogen in the present flexible fuel cell was a very stable process, which supplied hydrogen to the anode at a constant rate. However, when the discharge current density was elevated to 5 mA cm^{-2}, the curve started to oscillate, which is probably due to the insufficient supply rate of H_2. Nevertheless, the discharge process could still be sustained until the Al foil exhausted. Higher discharge current densities than 5 mA cm^{-2} would lead to a quick drain up of the fuel cell (not shown in the figure). The battery lifetime and discharge efficiencies were all summarized in Table 1. It is interesting to note that even with only 3.5 mg Al, the fuel cell could work for 333.3 minutes stably at 1 mA cm^{-2}, leading to a high faradaic efficiency of 54.3% and energy efficiency of 16.7%. The highest faradaic efficiency of 72.0% was obtained at 5 mA cm^{-2}, while the highest energy efficiency of 18.3% appeared at 2 mA cm^{-2}. All these results prove that the generation of hydrogen in the present flexible fuel cell is a slow and stable process, while the wetted cellulose paper may also help to seal and store the generated H_2, preventing them from quick leakage into the ambient air.

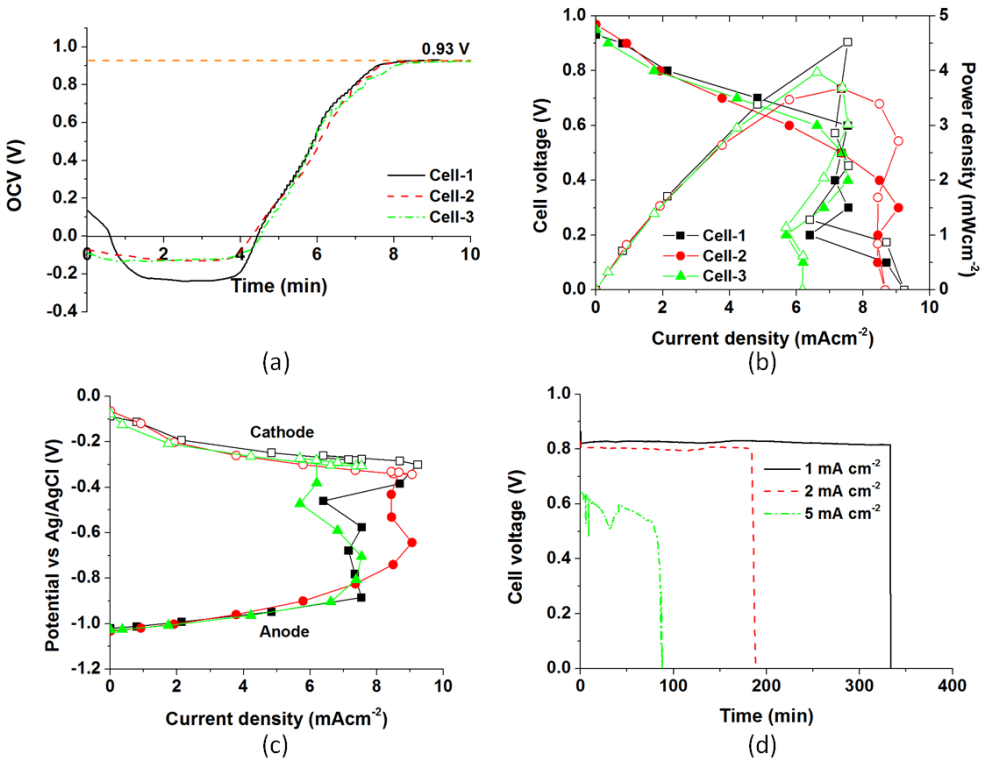

Fig. 2. Electrochemical testing of the present flexible hydrogen fuel cell: (a) Initiation of the cell OCV; (b) Polarization curve tested with 3 M NaOH at room temperature; (c) Single electrode polarization; (d) Galvanostatic discharge with 3.5 mg Al at different current densities.

Table 1. Summary of the fuel cell lifetime and discharge efficiencies

Current density	Battery lifetime	Faradaic efficiency	Energy efficiency
1 mA cm^{-2}	333.3 min	54.3%	16.7%
2 mA cm^{-2}	188.3 min	61.2%	18.3%
5 mA cm^{-2}	88.5 min	72.0%	14.6%

3.2 Comparison of H_2 generation rate

The slow and extended Al corrosion process in this work conflicts with the common sense that Al generally reacts vigorously with strong alkaline solution. To figure out the reason behind, a comparative study between a bare Al foil and a paper-embedded Al foil in alkaline was conducted by a drainage method as shown in Fig. 3(a). The volume of collected H_2 gas was recorded with a time step of 1 min for bare Al and 10 min for embedded Al, immediately after the Al was immersed into the alkaline. Fig. 3(b) shows the testing result with averaged values and error bars, which indicates that the corrosion rate was much slower of the embedded Al foil than that of the bare Al foil. For the former, the process could last for nearly an hour, while it was only 6 minutes for the latter case. In addition, both the two cases obtained a total gas volume of 4.8 mL which is the theoretical value of 3.5 mg Al foil at room temperature, proving the reliability of this drainage testing method. The average H_2 generation rate was 80 μL min^{-1} for the embedded Al and 800 μL min^{-1} for the bare Al. This difference is mainly because of the cellulose paper that wrapped the Al foil, whose micro fibre network helps to restrict the contact between the Al surface and alkaline solution. According to Bruggeman's diffusion model [23], the micro-scale pores of the paper will greatly decrease the effective diffusion coefficient of hydroxyl ions inside the paper, which consequently suppresses the Al corrosion and H_2 generation. However, it is worth noticing that the H_2 generation process in Fig. 2(d) could last as long as 5.6 hours, while it was only 1 hour in Fig. 3(b). This is mainly because that, in the former case only the end of paper was in contact with the alkaline, while in the latter case all the paper was immersed inside. Therefore, the diffusion path of the former is much longer (2.5 cm, length of the paper) than that of the latter (0.1 cm, half thickness of the paper), leading to an even longer corrosion time.

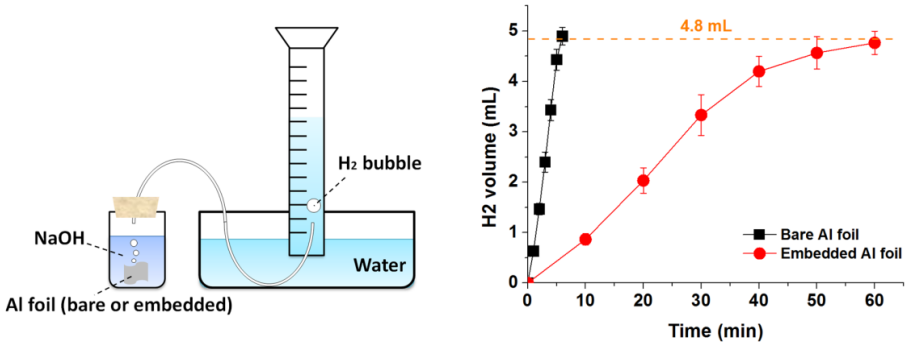

(a) (b)

Fig. 3 Comparative study of the H_2 generation rate between a bare Al foil and an embedded Al foil in paper: (a) Schematic diagram of the drainage method; (b) H_2 generation rate with 3.5 mg Al foil and 5 mL 3 M NaOH solution.

3.3 Study of fuel cell flexibility

Since cellulose paper was utilized as cell substrate and all other cell components such as ink-based electrode, Ag grid current collector and Al foil were flexible, the present hydrogen fuel cell was intrinsically a flexible power source, which can be applied in many flexible devices such as wearable electronics, biosensors, RFID tags, etc. To investigate its flexibility, the effect of bending angle on cell power output was studied. As shown in Fig. 4(a), the fuel cell was bended by the middle of its electrode from 45° to 135°, with the air-breathing cathode inside and the anode outside, while their polarization curves were compared in Fig. 4(b) and 4(c). In general, the bending has slightly decreased the fuel cell peak power density from 4 to 3.0-3.5 mW cm^{-2} (12.5-25% loss), while the OCV was not affected. However, it is interesting to find that the H_2 mass transport loss was greatly alleviated by the bending process, extending the maximum current density from 8 to 10.7-11.7 mA cm^{-2} (33.8-46.3% increase). This is probably because that the bending process has improved the contact between the Al foil and the paper substrate, leading to higher Al corrosion and H_2 generation rates. However, the bending did impair the electric conductivity of the electrodes, resulting in slightly lower power output at the high voltage region. In summary, the fuel cell exhibits good flexibility and will be competent for powering various flexible miniwatt devices.

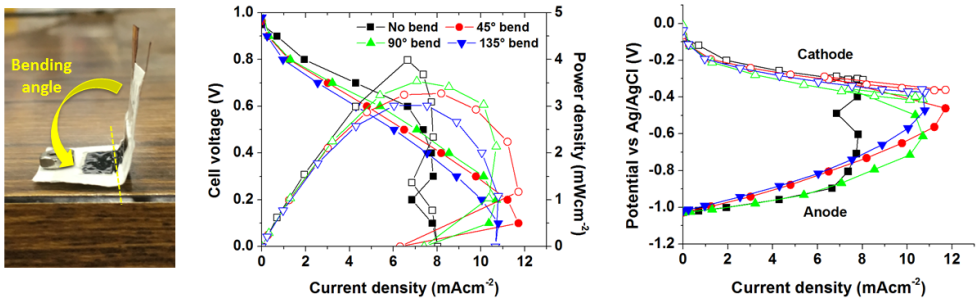

(a) (b) (c)

Fig. 4 Investigation of the fuel cell flexibility: (a) The bended fuel cell prototype; (b) Polarization curve tested at different bending angles; (c) Single electrode polarization.

4 Conclusion

In this work, a lightweight and compact flexible fuel cell system is developed by using cellulose paper as substrate. An embedded Al foil inside the paper is innovatively utilized as the hydrogen fuel source, which produces hydrogen in-situ via the Al-H_2O reaction. In addition, ink-based flexible electrodes are also deposited directly onto the paper surface. With alkaline as electrolyte, the fuel cell can provide an OCV of 0.93 V, a peak power density of 4 mW cm^{-2} and a maximum current density of 8 mA cm^{-2}. Benefitted from protective effect of the paper substrate, the Al corrosion is found to be a gentle and mild process, which can continuously provide H_2 for more than 5 hours even with only 3.5 mg Al. Consequently, the cell discharge faradaic and energy efficiency are as high as 72% and 18.3%, respectively. Finally, the fine fuel cell flexibility is also well demonstrated by bending it into different angles.

The authors would like to acknowledge the CRCG grant of the University of Hong Kong and the SZSTI of Shenzhen Municipal Government to provide funding support to this project.

References

1. G.W. Crabtree, M.S. Dresselhaus, M.V. Buchanan, Phys Today, **57**, 39-44 (2004).
2. R. O'hayre, S.-W. Cha, F.B. Prinz, W. Colella, *Fuel cell fundamentals* (John Wiley & Sons 2016).
3. V. Mehta, J.S. Cooper, J. Power Sources, **114**, 32-53 (2003).
4. I. Chang, T. Park, J. Lee, H.B. Lee, S. Ji, M.H. Lee, S.H. Ko, S.W. Cha, Int. J. Hydrogen Energy, **39**, 7422-7427 (2014).
5. I. Chang, T. Park, J. Lee, H.B. Lee, S.H. Ko, S.W. Cha, Int. J. Hydrogen Energy, **41**, 6013-6019 (2016).
6. I. Chang, T. Park, J. Lee, M.H. Lee, S.H. Ko, S.W. Cha, J. Mater. Chem. A, **1**, 8541-8546 (2013).
7. F.-K. Hsu, M.-S. Lee, C.-C. Lin, Y.-K. Lin, W.-T. Hsu, J. Power Sources, **219**, 180-187 (2012).
8. T. Ito, K. Kimura, M. Kunimatsu, Electrochem. Commun., **8**, 973-976 (2006).
9. T. Park, I. Chang, H.B. Lee, S.H. Ko, S.W. Cha, Int. J. Hydrogen Energy, **42**, 1884-1890 (2017).
10. S. Tominaka, H. Nishizeko, J. Mizuno, T. Osaka, Energy Environ. Sci, **2**, 1074-1077 (2009).
11. C. Weinmueller, G. Tautschnig, N. Hotz, D. Poulikakos, J. Power Sources, **195**, 3849-3857 (2010).
12. J. Wheldon, W.-J. Lee, D.-H. Lim, A.B. Broste, M. Bollinger, W.H. Smyrl, Electrochem. Solid-State Lett., **12**, B86-B89 (2009).
13. A. wins Army, *Fuel Cells Bulletin* (2010).
14. E. Kjeang, N. Djilali, D. Sinton, J. Power Sources, **186**, 353-369 (2009).
15. S.A.M. Shaegh, N.-T. Nguyen, S.H. Chan, Int. J. Hydrogen Energy, **36**, 5675-5694 (2011).
16. T.S. Copenhaver, K.H. Purohit, K. Domalaon, L. Pham, B.J. Burgess, N. Manorothkul, V. Galvan, S. Sotez, F.A. Gomez, J.L. Haan, Electrophoresis, **36**, 1825-1829 (2015).
17. J. Esquivel, F. Del Campo, J.G. de la Fuente, S. Rojas, N. Sabate, Energy Environ. Sci, **7**, 1744-1749 (2014).
18. A. Dector, J. Galindo-de-la-Rosa, D. Amaya-Cruz, A. Ortíz-Verdín, M. Guerra-Balcázar, J. Olivares-Ramírez, L. Arriaga, J. Ledesma-García, Int. J. Hydrogen Energy, **42**, 27979-27986 (2017).
19. S.M.M. Ehteshami, M. Asadnia, S.N. Tan, S.H. Chan, J. Power Sources, **301**, 392-395 (2016).
20. J.P. Esquivel, J. Buser, C. Lim, C. Dominguez, S. Rojas, P. Yager, N. Sabate, J. Power Sources, **342**, 442-451 (2017).
21. C. Xu, B. Li, H. Du, F. Kang, Y. Zeng, J. Power Sources, **180**, 664-670 (2008).
22. S.M. Mitrovski, R.G. Nuzzo, Lab on a Chip, **6**, 353-361 (2006).
23. V.D. Bruggeman, Annalen der physik, **416**, 636-664 (1935).

Numerical investigation on the characteristics of water transfer in PEMFC with bionic flow channel

Tao Chen , *Shihua* Liu[¯], and *Li* Yang

School of Mechanical and Electronic Engineering, Wuhan University of Technology, Wuhan 430070, China

Abstract. The content and the transmission characteristics of the water in the polymer electrolyte membrane fuel cell (PEMFC) have a significant influence on its performance. So far, there are few separate numerical studies on the process of water transport in the bionic flow channel, and the performance of bionic flow channel is different from conventional flow channel in part owing to the differences of their water drainage. Therefore, in order to understand the water drainage process of bionic flow channel, two different types of bionic flow channels are adopted in this paper. The method of numerical simulation is used to study the transmission process of liquid water in the bionic flow channel of different placement orientations. The simulation results found that the orientations of bionic flow channel has an influence on the process of water transport in the flow channel, and the process of water drainage also has a significant difference in the two different types of bionic flow channel.

1 Introduction

The water management has always been the main problem to further enhance the performance of PEMFC[1], in order to deeply understand the influence of the water transfer state and the various control parameters on the water transmission, so as to improve the internal structure and material properties of fuel cell, more and more studies on the water management of fuel cell are emerging, such as the high-tech measurement methods of X-rays, neutron imaging, scanning electron microscopy and nuclear magnetic resonance, etc. Those high-tech measurement methods are adopted to accurately study the transmission process of water in the internal flow channels [2-3], using micro-electro-mechanical systems technology [4-5] and optical fiber sensor [6-8] etc to measure the Water transfer process in the flow channel, more researches are based on visualization technology to observe the state of water transfer in the fuel cell[9-11], although these techniques can be used to study the state of water transfer inside the flow channel, due to the experimental difficulties, and the cost is relatively so higher that these methods are limited to some extent.

Up to date, the method of computer simulation is applied in most studies [12-15], Such as utilizing lattice Boltzmann model[16-18] and volume-of-fluid (VOF) model [19-23] to

[¯] Corresponding author: lshtgyx@163.com

simulate the process of water transfer in fuel cell, the results of those methods show that the characteristics and phenomena of the water transfer in the flow channel of the fuel cell are both well explained. Anh Dinh Le [19] et al. numerically investigated the process of water transfer in PEMFC with interdigitated flow channel. Theodorakakos A [20] et al. simulated the dynamic process of liquid droplet detachment from porous surface. M. Koz [21] et al. numerically investigated the effects of droplet size in a PEMFC flow field. Cai Y [22-23] et al. numerically investigated the water transfer process in the serpentine flow channel and the straight flow channel. From these studies, on the one hand, through the computer simulation, the detailed process of the liquid water transfer in the flow channel and the factors which affect water transfer can be found. On the other hand, it can be found that the water transfer process of the existing research are focuses on the inner of conventional flow channel, few scholars have carried out the separate simulation study on the water transfer process in the bionic flow channel, and part of the performance of bionic flow channel is different from conventional flow channel owing to the differences of their water drainage [24]. Therefore, the simple numerical study on liquid water in a conventional flow channel is not enough to fully explain the phenomenon of water transport in the bionic flow channel.

With the continuous development of bionic design in recent years, many researchers have applied the bionic design to the flow channel of fuel cell, Ramos-Alvarado et al. [25] applied the constructal theory to the design of flow field. Kloess et al. [26] evaluated the performance of the flow field plate based on the types of lung and leave. Roshandel et al. [27] investigated the performance of the flow field plate based on the type of a leaf. Chen et al. [28] also investigated the performance of leaf type flow field. Guo et al. [29] presented a mathematical model to investigate the performance of leaf type flow field. However, these scholars only conduct the overall test or simulation to the performance of fuel cell which have utilized the method of bionic design, and there is no separate study on the drainage performance in the flow channel of bionic design. From these researches of bionic design, we can not understand enough the water drainage characteristics of flow channel with bionic design, which is not conducive to the design improvement of bionic flow channel and the problem of water management will have a greater effect on the performance of the PEMFC [30].

Therefore, it is significant to investigate the characteristics of water transport in the bionic flow channel. This paper mainly study the transmission process of water in bionic flow channel. Two different types of symmetrical leaf bionic flow channel and asymmetrical leaf bionic flow channel are selected as the research object [31], utilizing the method of numerical simulation to present the transfer process of liquid water in the bionic flow channel, and the influence of different placement orientations of bionic flow channel on water transport has also been studied. All of this can be conducive to a clear understanding of the internal water drainage process of bionic flow channel in detail, it also provides the necessary guidance and basis for the design of bionic flow channel.

2 Numerical models

2.1 VOF model

The numerical simulations of the 3D, laminar, unsteady, two-phase flow was applied to the computation domain using FLUENT 15.0. The conservation of mass and momentum were applied to the model as the governing equations and the energy equations were not considered. In order to track the two-phase flow interface of gas-water in the domain of computation, the method of volume-of-fluid (VOF) was used [32]. Then, the conservation law of mass and momentum are as follows:

Continuity equation:

$$\frac{\partial \rho}{\partial t} + \nabla \cdot (\rho \vec{v}) = 0 \tag{1}$$

Momentum equation:

$$\partial(\rho \vec{v})/\partial t + \nabla \cdot (\rho \vec{v} \vec{v}) = -\nabla p + \nabla \cdot (\vec{\tau}) + \rho \vec{g} + \vec{F} \tag{2}$$

where $\vec{F}$ is the momentum source term due to surface tension, ρ is the static pressure and $\vec{\tau}$ is the stress tensor:

$$\vec{\tau} = \mu\left[\left(\nabla \vec{v} + \nabla \vec{v}^{T}\right) - 2/3 \nabla \cdot \vec{v} I\right] \tag{3}$$

Where I is the unit tensor, μ is the dynamic viscosity .

Volume fraction of water α_2 can be solved as follows:

$$\frac{\partial \alpha_2}{\partial t} + \vec{v} \cdot \nabla \alpha_2 = 0 \tag{4}$$

The volume fraction of gas α_1 can be solved by following equation:

$$\alpha_1 + \alpha_2 = 1 \tag{5}$$

The surface tension of phase and wall has an important influence on the transmission process of two-phase flow which is included in the VOF model[32]. In the paper, the model of continuum surface force which is proposed by Brackbill et al. [33] was used.

2.2 Geometric model

Figure 1 is a model of two different bionic flow channel structures. These two bionic structures are derived from Ref. [31]. A water inlet hole of 0.2mm diameter is arranged on the wall near the inlet of the bionic flow channel (The wall is the interface between the channel and the gas diffusion layer (GDL)) [23]. FLUENT 15.0 is used to simulate water dynamic in the bionic flow channels. The number of meshes of symmetrical leaf bionic flow channels is 221674, and The number of meshes of asymmetrical leaf bionic flow channels is 232583. Accuracy of the model tested by increasing and reducing the number of meshes by 20%, and the similar processes of water transport were obtained.

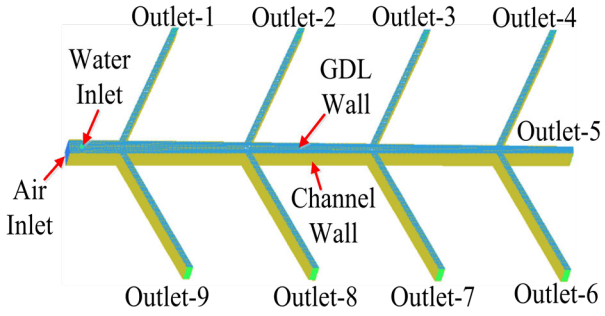

(a) Symmetrical leaf bionic flow channel

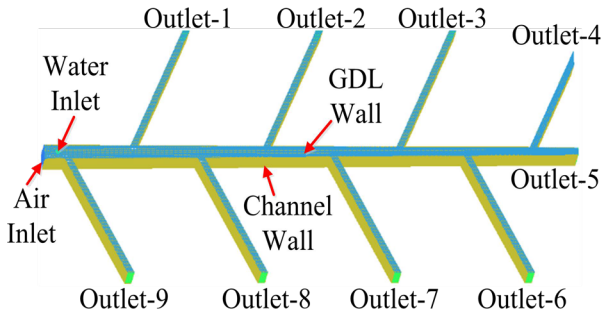

(b) Asymmetrical leaf bionic flow channel

Fig. 1. Schematic of two different bionic flow channel

2.3 Geometric model

In the parameter settings of the simulation, a gas velocity of 10 ms^{-1} normal to the boundary is used[34]. Moreover, according to the theoretical calculation of the velocity of water to be about $1.8x10^{-6}$ ms^{-1}, which is too small compared to 10 ms^{-1} of gas inlet [35]. To accelerate the speed of computational, the velocity of water with 0.1ms^{-1} normal to the boundary is used in this study. The gauge pressure at the outlet of the flow channel is set to 0Pa. In all the computational cases, the gravity is considered all the time according to the different locations of the flow channel placement. The contact angle of the surface of GDL and flow channel wall were 140° and 45°, respectively [36]. The time step was set at 10^{-6} s in order to guarantee that the global courant number is less than one. The surface tension at the gas-liquid interface is 0.072 Nm^{-1}. In order to solve the governing equations, the pressure velocity coupling method via the PISO scheme is used.

3 Results and discussion

The characteristics of water flow in the bionic flow channel are simulated. The five cases corresponding to different orientations of bionic flow channel placement were simulated, as listed in Table.1. Detailed results and discussions are as follows.

Table 1. The gravity in different orientations of leaf bionic flow channel placement

	X axial gravity/(ms^{-2})	**Y axial gravity/(ms^{-2})**	**Z axial gravity/(ms^{-2})**
Side	0	-9.8	0
Inversion	-9.8	0	0
Reversal	0	0	9.8
Perpendicularity	9.8	0	0
Level	0	0	-9.8

3.1 The state of water in the symmetrical leaf bionic flow channel in different orientations and different time

Fig.2 is the state of the water in the symmetrical leaf bionic flow channel in five different orientations (side, inversion, reversal, perpendicularity and level) and different

time. From Fig. 2-a, at about 3ms, the droplets in a state of constant expansion hardly move. Since the wall of the water inlet is the surface of the GDL, the volume of the droplets at the beginning is very small, and the force of gas flow exerting on the droplet is not enough to get rid of the adsorption force between the droplet and the surface of the GDL. Only when the liquid droplet grows up to a certain volume before the apparent movement, and this situation also occurred in the Fig. 2-b, c, d, e. From Fig. 2-a, b, c, d, e (symmetrical leaf bionic flow channel in the state of side, inversion, reversal, perpendicularity and level respectively) can be seen, at about 9ms, the droplets move mostly in the branch flow channels (outlet-1 and outlet-9) where near the gas inlet, it can be also seen from Fig. 11 that the pressure difference in the branch flow channel nearer the gas inlet is larger, and it may also explain the reason why the droplets move faster in the branch flow channel where nearer the gas inlet.

However, from Fig.3, before the 11ms time, no matter what kind of orientations of the symmetrical leaf bionic flow channel, their maximum velocity curves are almost identical. After 11ms, the maximum velocity of the internal flow under the condition of different flow channel placement has a fluctuation. At about 15ms, from Fig. 2, there are water droplets in each branch flow channel (such as outlet-1 and outlet-9 etc.) where near the gas inlet of the symmetrical leaf bionic flow channel. There are few droplets in the branch flow channel (such as outlet-4 and outlet-6 etc.) where is far away from the gas inlet. It shows that the water in the symmetrical bionic flow channel is mainly discharged from the branch flow channel where near the gas inlet. What's more, it can be also seen from Fig. 11 that the pressure difference is very small in the branch flow channel where is far away from the gas inlet, and we can infer that the velocity of the liquid water flow in these flow channels is the slowest, Once liquid water accumulates in the branch flow channel where is far away from the gas inlet is difficult to be discharged rapidly, so that the water content is higher in these branch flow channels. It is the same to the results obtained by other literature that there are higher water content in the branch flow channel where is far away from the gas inlet [24,26,37].

In addition, from Fig.4, it shows the volume of water in the symmetrical flow channel in the different orientations and different time, and when the flow channel is in the orientation of perpendicularity, the performance of water drainage is the best, because the direction of the droplet gravity is consistent with the direction of gas flow. So, when designing symmetrical bionic flow channel which branch flow channel should be closer to the gas inlet and the number of branches along the main flow channel shouldn't be too many. Only in this way, it is possible to avoid the pressure of the branch flow channel which is far away from the gas inlet too small, so as to keep the flow channel well drained.

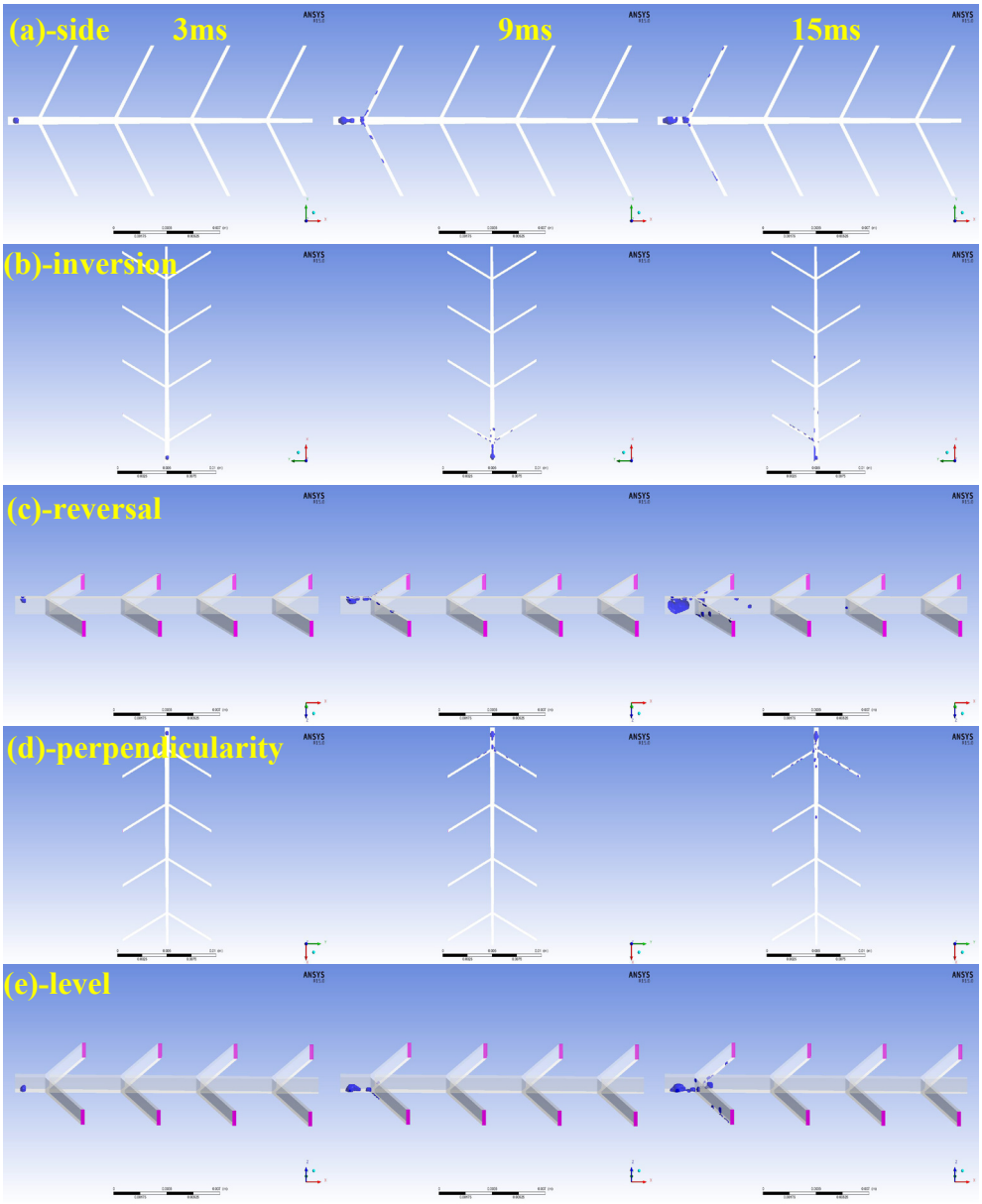

Fig. 2. The state of water in the symmetrical flow channel in different orientations and different time

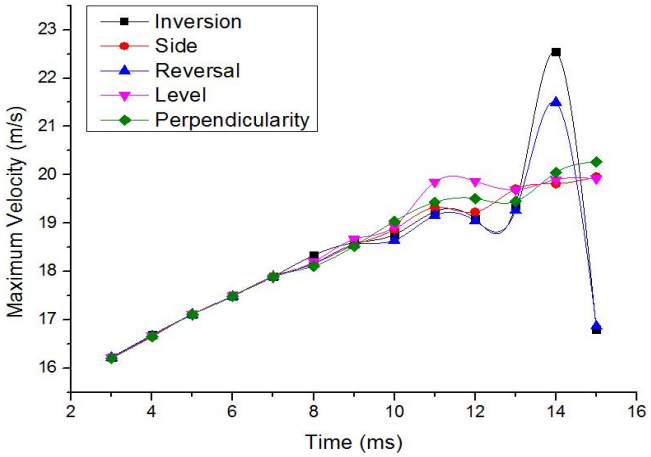

Fig. 3. The maximum velocity in the symmetrical flow channel in the different orientations and different time

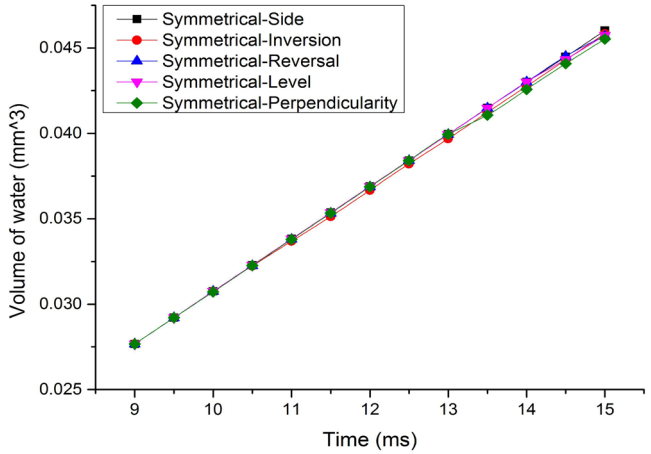

Fig.4. Volume of water in the symmetrical flow channel in the different orientations and different time

3.2 The state of water in the asymmetrical leaf bionic flow channel in different orientations and different time

Fig.5 is the state of water at different time in five different orientations (side, inversion, reversal, perpendicularity and level) in an asymmetrical leaf bionic flow channel. As the same shown in Fig. 2, the droplets barely move at about 3ms. At about 9 ms, there are significant differences in the distribution of liquid water droplets between Fig. 4-a, c, d (the asymmetrical leaf bionic flow channel in side, reversal and perpendicularity orientations) and 4-b, e (the asymmetrical leaf bionic flow channel in inversion and level orientations), and it can be seen that the position of liquid water droplets is almost consistent with the time of 3ms in Fig.5-b, e. That is to say that the liquid water moves slowly when the flow channel was placed in the state of inversion and Level. As shown in Fig.5-a, c, d, the liquid water mainly distribute in the main flow channel of bionic flow channel and the velocity is faster.

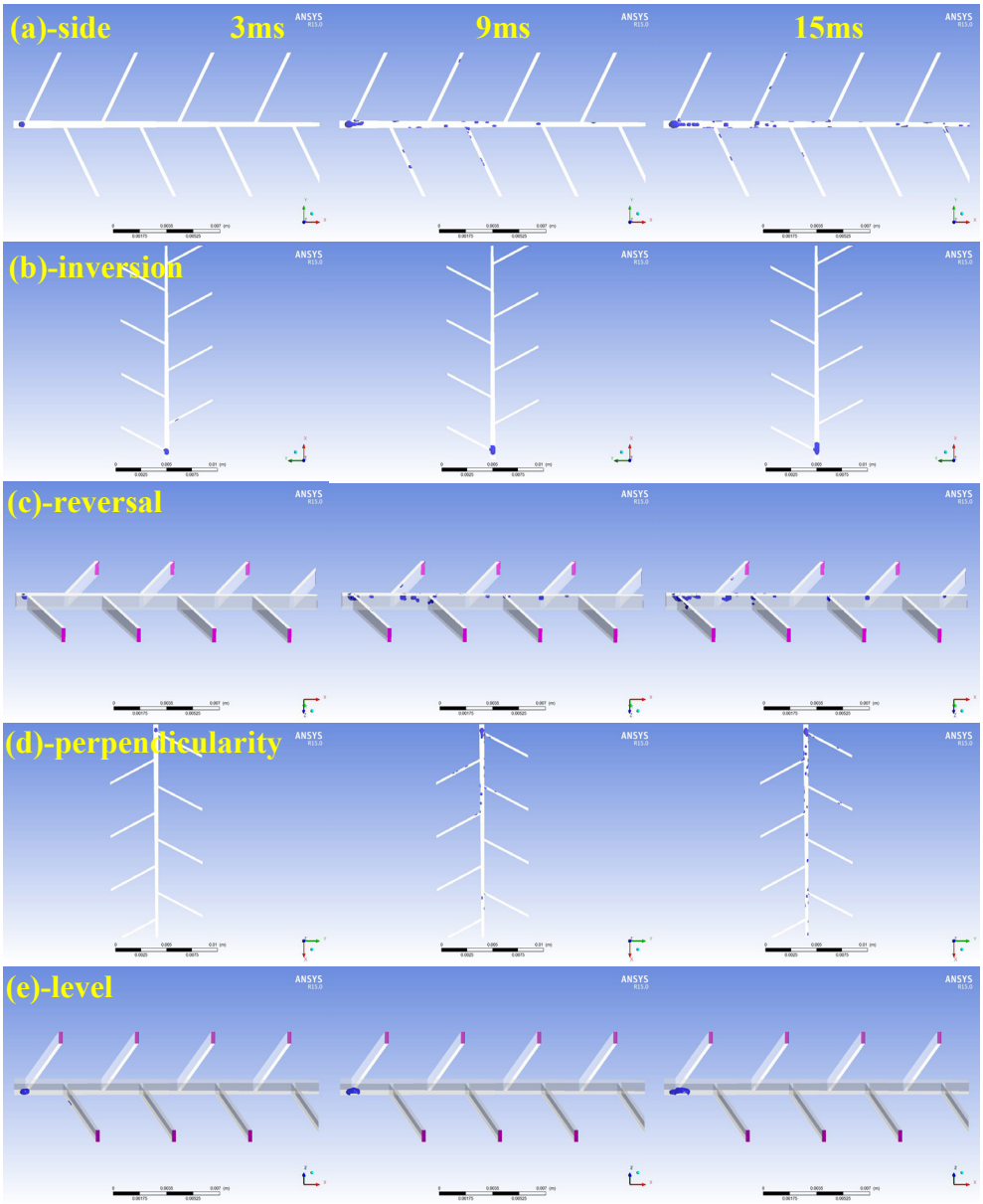

Fig.5. The state of water in the asymmetrical flow channel in different orientations and different time

It can be seen from Fig. 6 that the maximum velocity inside the flow channel which are the positions of side, reversal and perpendicularity is significantly faster than that in inversion and level positions. Because of the different orientations of flow channel, the directions of gas blowing force and gravity on the liquid water are different. It can be drawn that the gravity has a large effect on the movement and distribution of water droplets inside the channel when the asymmetrical leaf bionic flow channel is in different orientations. At about 15ms, it can be seen that the distance to gas inlet count for little the distribution of liquid water in branch flow channel, which is greatly different to the phenomenon that the

shorter of the distance to gas inlet, the more liquid water in branch flow channel of symmetrical leaf bionic flow channel. As shown in Fig.5-b, e, there are little difference in the movement of liquid water between inversion and level orientations in asymmetrical leaf bionic flow channel at about 15ms. In addition, it can be concluded from the Fig. 12 that pressure difference in each branch flow channel reduce along the direction of main flow channel in asymmetrical leaf bionic flow channel. Once liquid water accumulates in the branch flow channel which is far away from the gas inlet is difficult to be discharged rapidly, Therefore, the water in these branch flow channels is higher, and it can be drawn the same conclusions from other literature [24,26,37]. In addition, from Fig.7, it shows the water volume in the symmetrical flow channel in the different orientations and different time, and when the flow channel is in the orientation of perpendicularity, the performance of water drainage is the best, because the direction of the droplet gravity is consistent with the direction of gas flow. In conclusion, to avoid the pressure difference too low to drain liquid water from branch flow channel, the number of branches along the main flow channel shouldn't be too many in design of asymmetrical bionic flow channel.

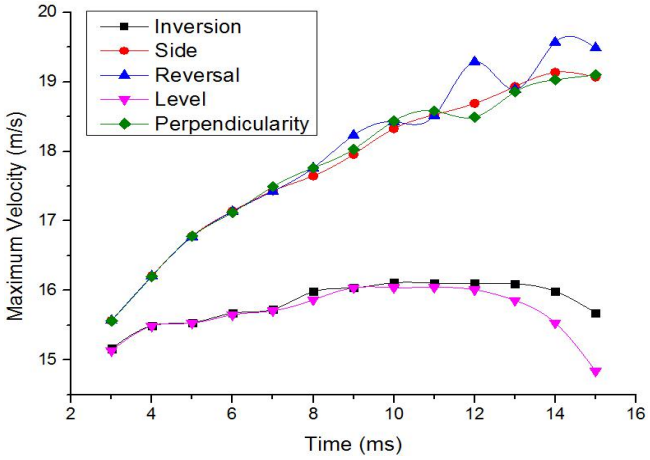

Fig.6. The maximum velocity in the asymmetrical flow channel in the different orientations and different time

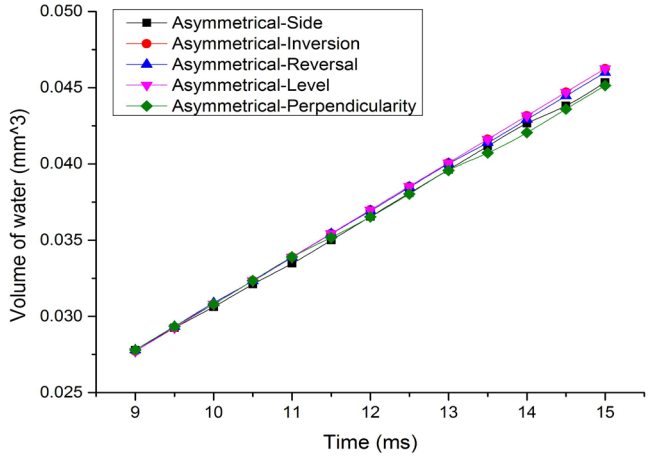

Fig.7. Volume of water in the asymmetrical flow channel in the different orientations and different time

3.3 The state of water in the flow channel of symmetrical and asymmetrical structures in the same orientation

In order to compare the state of water droplets at different time and same orientations more clearly in the bionic flow channel for symmetrical and asymmetrical of leaf type, followed a detailed comparison of the state of water movement in the two different bionic flow channels at different time. From Fig.8-a, Fig.8-c and Fig. 8-d, it can be seen that when the two bionic flow channels are in the three kinds of situations of side, reversal and perpendicularity respectively, the water inside the channel moves faster. However, the obvious difference of water distribution between the two channels can be seen in the three situations. For the water in the flow channel of symmetrical leaf bionic is mainly distributed in the branch flow channel where near the gas inlet, and there is almost no liquid water in the branch flow channel which is far away from the gas inlet, that is to say, comparing with the branch flow channel where far away from the gas inlet, most of the liquid water were drained from the branch flow channel where near the gas inlet. It also shows that the distance between gas inlet and branch flow channel has a great influence on the water distribution in the symmetrical leaf bionic flow channel. The liquid water in the asymmetrical bionic flow channel is mainly distributed in the main flow channel, and the other branch flow channel also has the presence of liquid water, in addition, the distribution of liquid water in the branch flow channel is no significant influence by the distance between the branch flow channel and the gas inlet, there is significant difference when compares with the situation that water is mainly distribution in the branch flow channel where near the gas inlet for the symmetrical leaf bionic flow channel, it can be seen clearly that the difference of water distribution between the two kinds of flow channels at about 15ms. As it can be seen in Fig.8-b and Fig.8-e, when the two types of bionic flow channel were placed in inversion and level situation that also appeared obvious differences between the movement and the distribution of liquid water. The water were drained mainly from the branch flow channel where near the gas inlet for symmetrical leaf bionic flow channel in the situations of inversion and level placement, comparing to the case of the same placement of the asymmetrical bionic flow channel, the velocity of liquid water is faster, and the velocity of the liquid water movement in the asymmetrical bionic flow channel of the inversion and the level position is the slowest.

It also can draw from Fig.9, no matter what positions for the two kinds of bionic flow channels, the maximum velocity of the water in the symmetrical leaf bionic flow channel is almost higher than that in the asymmetrical leaf bionic flow channel. Especially, form Fig.10, it shows that the performance of water drainage is the best for the position of perpendicularity in asymmetrical flow channel, And it can be seen from Fig.13, the pressure in the main flow channel of the symmetrical leaf bionic flow channel is in a state of fluctuation, and the amplitude of the fluctuation is larger and nearly identical for each placement of the flow channel. However, the pressure in the asymmetrical bionic flow channel is in a relatively stable state, and the pressure fluctuation, although there is a slight difference in the pressure of each channel. Therefore, the difference of pressure fluctuation and steady change in the main flow channel of the two types of bionic flow channel may be one of the cases which cause the difference of water distribution finally. In other words, the fluctuation of pressure has some influence on the process of water drainage inside the flow channel, the evidence can also be obtained from other studies[38].

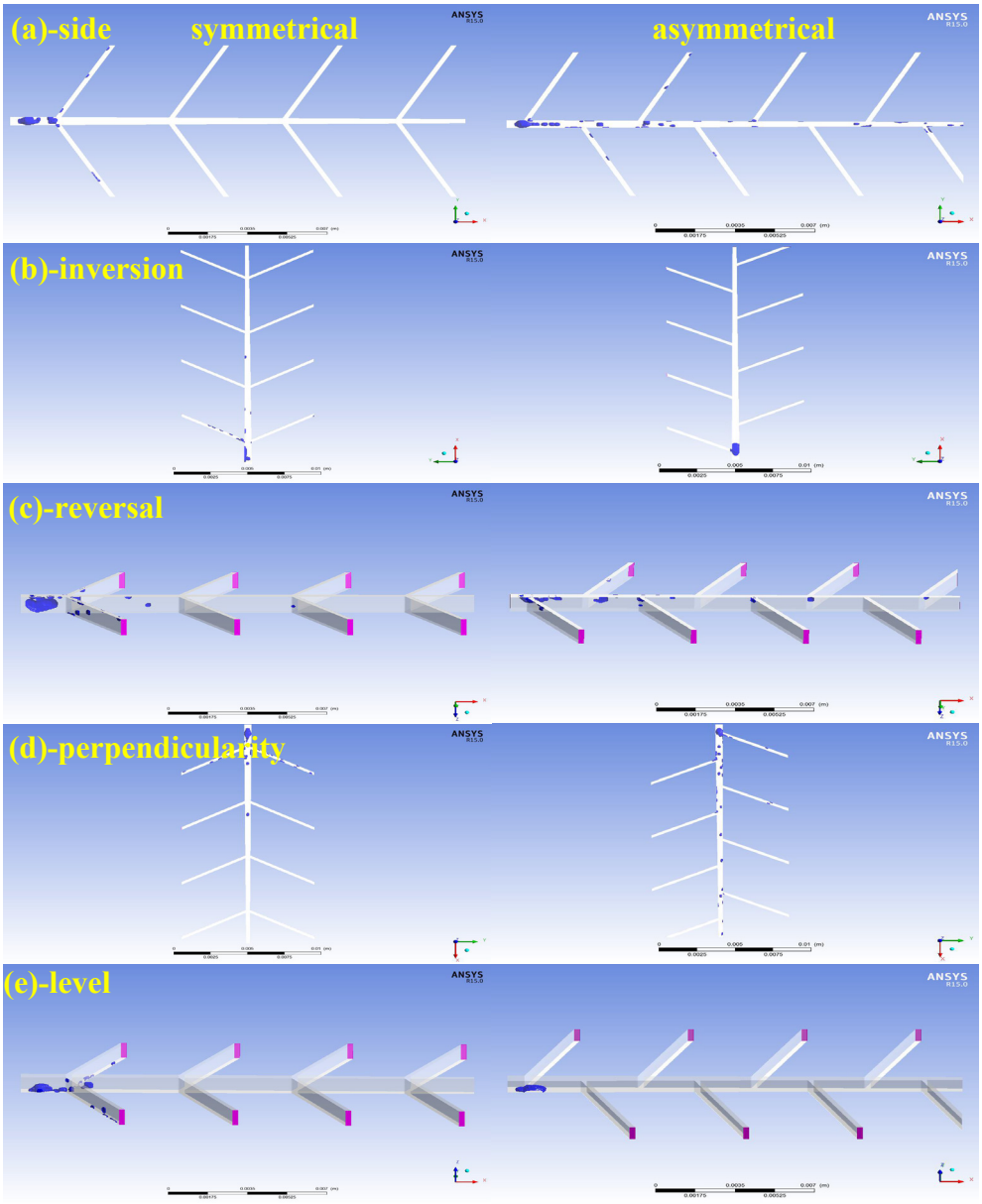

Fig.8. The state of water in flow channel of symmetrical and asymmetrical structures in different orientations and the time of 15ms

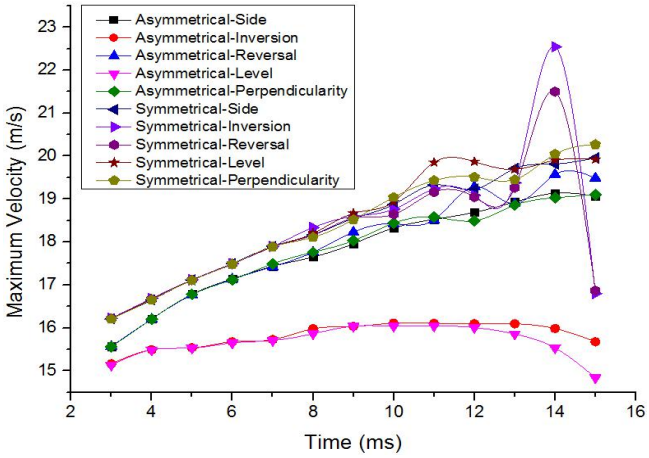

Fig.9. The maximum velocity in flow channel of symmetrical and asymmetrical structures in different orientations

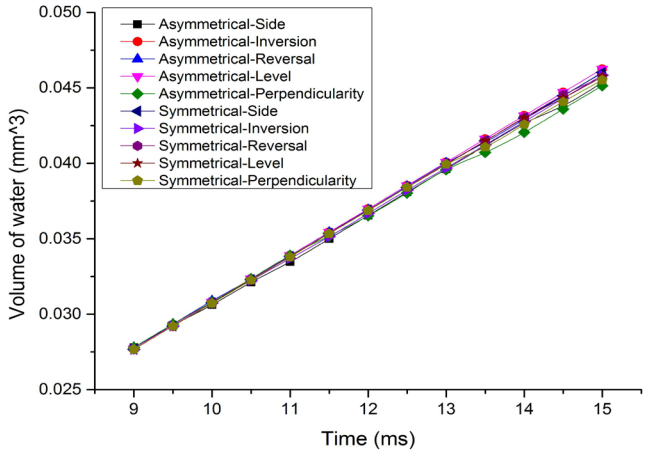

Fig.10. Volume of water in flow channel of symmetrical and asymmetrical structure in different orientations and different time

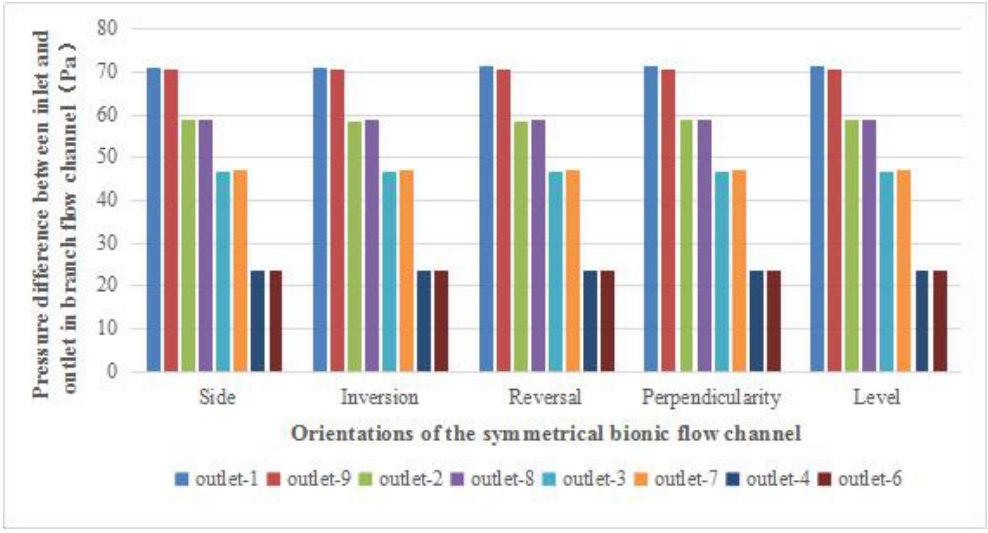

Fig. 11. The pressure difference in each branch flow channel of symmetrical structure in the different orientations

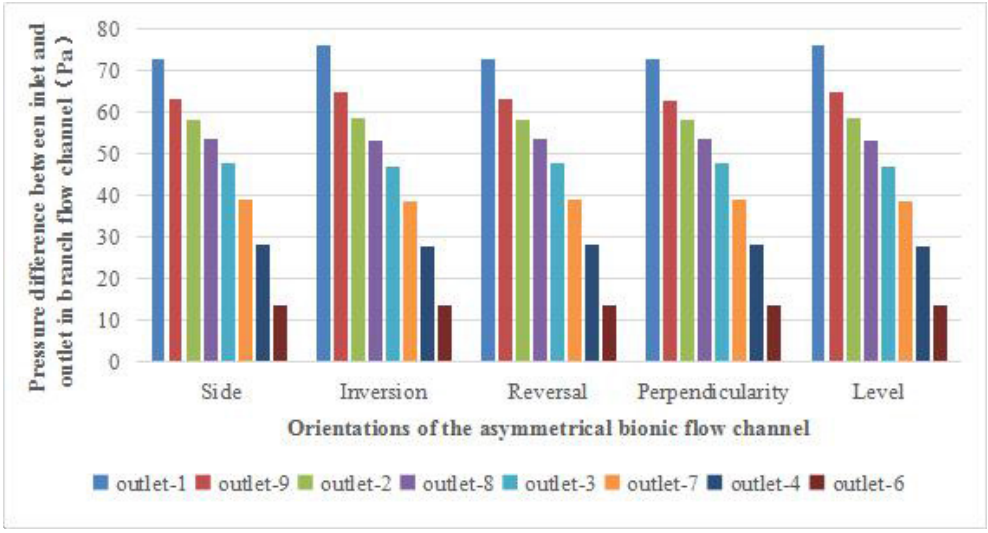

Fig.12. The pressure difference in each branch flow channel of asymmetrical structure in the different orientations

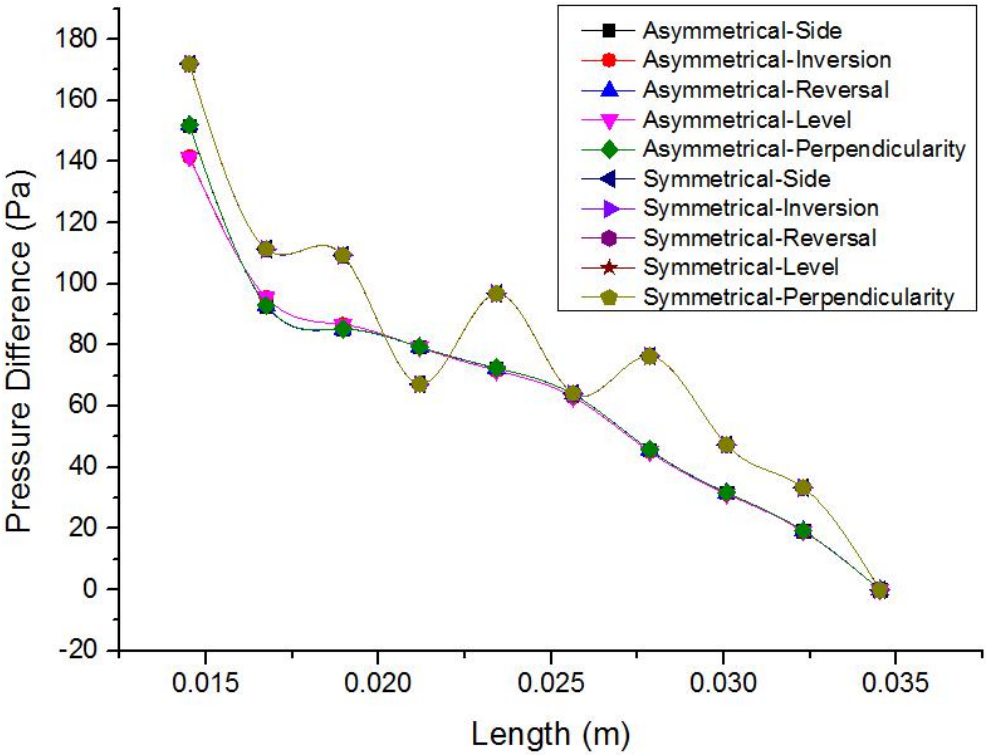

Fig. 13. The pressure difference in each branch flow channel of asymmetrical structure in the different orientations

4 Conclusion

This paper is mainly focused on the comparison and analysis of the flow and distribution of liquid water in the symmetrical and the asymmetrical of leaf bionic flow channel in the different orientations(side, inversion, reversal, perpendicularity and level). The conclusions are as follows:

(1) By comparing and analyzing the distribution and movement of the liquid water in leaf bionic flow channel of the symmetrical and the asymmetrical structures, it is concluded that there are significant differences. For the type of symmetrical leaf bionic flow channel, comparing with the branch flow channel where far away from the gas inlet, water is mainly distributed in the branch flow channel which near the gas inlet, and there is almost no liquid water in the branch flow channel which is far away from the gas inlet.

(2) The water in the asymmetrical bionic flow channel is mainly distributed in the main flow channel, the other branch flow channel also has the presence of liquid water. In addition, the distribution of liquid water in the branch flow channel has no significant influence by the distance between the branch flow channel and the gas inlet. and when the two types of bionic flow channel are placed in the positions of inversion and level respectively, the maximum velocity in the internal symmetrical bionic flow channel is far greater than that in the asymmetrical bionic flow channel.

(3) As shown in Fig.13, the pressure difference in the two different types of flow channel presents a state of fluctuation and slow change, the difference of pressure fluctuation and steady change in the main flow channel of the two types of bionic flow channel may be one of the cases which cause the difference of water distribution finally. In

other words, the fluctuation of pressure has some influence on the process of water drainage inside the flow channel, the evidence can also be obtained from other studies [38].

(4) It can also be known by the pressure analysis that the pressure difference in the main flow channel of symmetrical and asymmetrical is more smaller when the distance is more larger between the branch flow channel and gas inlet. In conclusion, to avoid the pressure drop too low to drain liquid water easily, the number of branches along the main flow channel shouldn't be too many in design of symmetrical and asymmetrical leaf bionic flow channel. Moreover, no matter what kinds of orientations of the symmetrical and asymmetrical leaf bionic flow channel, the liquid water in the bionic flow channel is easier to be drained when the flow channel is in the position of perpendicularity.

Totally, the results of the present work would be beneficial in design of bionic flow channel for PEMFC.

Acknowledgments

The authors would like to thank the National Science Foundation of China [No.51575413] and the Wuhan Science and Technology Bureau in China [No.2018010401011329] for funding this study.

References

1. K Jiao, X Li, PROG ENERG COMBUST. **37**, 221-291 (2011)
2. I Manke, C Hartnig, N Kardjilov, Fuel Cells. **10**, 26-34 (2010)
3. M Saito, A Kikuko Hayamizu, T Okada, J PHYS CHEM B. **108**, 16064-16070 (2005)
4. CH Chen , CY Lee, S Lee, YM Liu, INT J HYDROGEN ENERG. **39**, 18337-18342 (2014)
5. Lee C, Lee Y, INT J HYDROGEN ENERG. **37**, 4448-4456 (2012)
6. K Inman, X Wang, INT J HYDROGEN ENERG. **39**, 19691-19700 (2014)
7. N David, KV Schilling, PM Wild, N Djilali, INT J HYDROGEN ENERG. **39**, 17638-17644 (2014)
8. N David, N Djilali, MICROFLUID NANOFLUID. **13**, 99-106 (2012)
9. K Nishida, T Murakami, S Tsushima, S Hirai, Electrochemistry. **75**, 149-151 (2007)
10. H Masuda, K Ito, T Oshima, K Sasaki, J POWER SOURCES. **177**, 303-313 (2008)
11. S Lee, DH Rhee, WH Pyen, HH Cho, J MECH SCI TECHNOL. **25**, 957-961 (2011)
12. T Chen, S Liu, S Gong, C Wu, INT J ENERG RES. **37**, 1680-1688(2013)
13. A Su, YC Chiu, FB Weng, INT J ENERG RES. **29**, 409-425 (2010)
14. YM Ferng, A Su, SM Lu, INT J ENERG RES. **32**, 12-23 (2010)
15. WJ Yang, SJ Kang, YB Kim, INT J ENERG RES. **36**, 1051-1064 (2012)
16. HB Han, M Ni, H Meng, Entropy. **18**, 17(2016)
17. Song Bao-Wei, Ren Feng, Hu Hai-Bao, Qiao-Gao H, J POWER SOURCES. **278**, 703-717 (2015)
18. B Han, H Meng, INT J HYDROGEN ENERG. **38**, 5053-5059 (2013)
19. AD Le, B Zhou, J POWER SOURCES. **193**, 665-683 (2009)
20. A Theodorakakos, T Ous, M Gavaises, J COLLOID INTERF SCI. **300**, 673-687 (2006)
21. KG Maler, Ecs Transactions. **50**, 183-196 (2013)

22. JY Cai, T Chen, T Yang, J Xiao, J POWER SOURCES. **209**, 90-104 (2012)
23. Y Cai, T Yang, PC Sui, J Xiao, INT J HYDROGEN ENERG. **41**, 16220-16229 (2016)
24. H Ruan, C Wu, S Liu, T Chen, HEAT MASS TRANSFER. **52**, 1-10 (2016)
25. B Ramos-Alvarado, A Hernandez-Guerrero, F Elizalde-Blancas, INT J HYDROGEN ENERG. **36**, 12965-12976 (2011)
26. JP Kloess, X Wang, J Liu, Z Shi, L Guessous, J POWER SOURCES. **188**, 132-140 (2009)
27. R Roshandel, F Arbabi, G K Moghaddam, RENEW ENERG. **41**, 86-95 (2012)
28. T Chen, Y Xiao, T Chen, Energy Procedia. **28**, 134-139 (2012)
29. N Guo, MC Leu, M Wu. 607-623 (2011)
30. HS Kim, K Min, J MECH SCI TECHNOL **28**, 3837-3843 (2014)
31. XQ Wang, P Xu, AS Mujumdar, C Yap, INT J THERM SCI. **49**, 272-280 (2010)
32. Fluent 6.1 User's Guide, Fluent Inc.
33. J U Brackbill, D B Kothe, C Zemach, J COMPUT PHYS. **100**, 335-354 (1992)
34. X Zhu , P C Sui, N Djilali, MICROFLUID NANOFLUID. **4**, 543-555 (2008)
35. K Jiao , B Zhou, J FUEL CELL SCI TECH. **5**, 41011 (2008)
36. B Sundén , M Faghri, Energy Resources (Apr). 175-213 (2005)
37. N Guo, M C Leu , U O Koylu , INT J HYDROGEN ENERG. **39**, 21185-21195 (2014)
38. J W Choi, Y S Hwang, S W Cha, S K Min, Fuel & Energy Abstracts. **35**, 12469-12479 (2010)

Effects of temperature on oxidation behaviours of 35CrMo in high temperature flue gas environment

Chengchao Cui[1], *Shuzhong* Wang[1,*], *Jianqiao* Yang[1], *Baoquan* Zhang[1], *Zhuohang* Jiang[1], *Dong* Wang[1], and *Jianna* Li[1]

[1]Key Laboratory of Thermo-Fluid Science and Engineering of MOE, School of Energy and Power Engineering, Xi'an Jiaotong University, Xi'an 710049, PR China

Abstract. The pipelines made by alloy 35CrMo are widely used in the process of flue gas injection. Therefore, corrosion behaviours of alloy 35CrMo have been investigated at varied temperatures, namely 120 °C, 150 °C, 200 °C and 250 °C, with same experimental pressure of 9 MPa and flus gas environment. Scanning electron microscopy was employed to examine the morphologies and microstructures of the oxide films. The results indicated that moderate temperature stands an essential role in the reaction mechanism and aggressive effects. In addition to increase in the diffusion rate of both alloy ions and corrosive gas, temperature can also reform the morphology of oxides by resulting in larger oxide particles and thicker oxide films, plus the transmission from needle-like oxides to spherical oxides.

1 Introduction

Flue gas injection is a tertiary recovery method in which the flue gas produced by boiler in heavy oil thermal recovery is processed and pressurized and then injected into the reservoir, mixing with residual crude oil to displace the crude oil. Besides approximately 79 ~ 85% N_2 [1], this gas mixture, which could lead to serious corrosion on carbon steels and alloys used in casings and pipelines, still contains 10 ~ 15% CO_2 and a little aggressive gas. Pan et al. [2] have conducted in-plant corrosion tests of five steel in a heating boiler to investigate the desulfurized flue gas corrosion coupled with deposits after flue gas desulfurization (FGD) unit and concluded that surface temperature of the steel was proved to be the key factor in the corrosion process.

The reaction mechanism and aggressive effects of flue gas on metals and alloys vary with different flue gas temperature ranges. At low flue gas temperature [3], when water vapour interacts with acid materials at the low temperature surface of metal wall, condensation would be achieved, leading to corrosion and decrease in apparatus life. At high flue gas temperature [4], sulphur, chlorine and alum salt corrosion are the main types of corrosion emerging at the surface on the side of gas, in which sulphur element corrosion is most common and relatively more serious. However, there are less literatures with regard

* Corresponding author: szwang@aliyun.com

to the effects of flue gas on carbon steels and alloys at specific temperature between high and low flue gas temperature at present. Consequently, to propose some reliable suggestions for choosing proper materials of casings and pipelines in oil filed, it is necessary and valuable to investigate the reaction mechanism and aggressive effects of flue gas on metals and alloys at moderate temperature.

The pipelines made by alloy 35CrMo are widely used in the process of flue gas injection. Therefore, with the flue gas generated by a boiler in Liaohe oil field in Liaoning Province of China acting as aggressive medium, corrosion behaviours of alloy 35CrMo have been investigated at different temperatures in this paper. Scanning electron microscopy (SEM) [5] was employed to examine the morphologies and microstructures of the oxide films. The results suggest an essential role played by moderate temperature in the reaction mechanism and aggressive effects. Besides increase in the diffusion rate of both alloy ions and corrosive gas, temperature can also change the appearances of oxides by leading to bigger oxide particles, thicker oxide films and the transmission from needle-like oxides to spherical oxides.

2 Experimental and instrumentations

Table 1 and Table 2 are the composition of the flue gas and alloy 35CrMo respectively. Alloy 35CrMo was cut into cubic pieces with dimensions of 8 mm x 6 mm x 5 mm. SiC sandpapers were used to smooth the cut materials, which were then soaked in ultrasonic wave cleaner with acetone for 30 min to degrease. Finally, cleaned by deionized water, these samples were put into the vacuum drying box to avoid air corrosion. Moreover, high–temperature tubular furnace (OTF-1200X-S, Kejing Co., Ltd) was the main equipment to proceed experiments and SEM was the crucial analysis tool.

In order to investigate the effect of temperature on corrosion behaviours of alloy 35CrMo, four discrete temperature points, namely 120 ℃, 150 ℃, 200 ℃ and 250 ℃, and four different time points namely 24 h, 48 h, 72 h and 96 h were set, with the same experimental pressure of 9 MPa and flue gas environment. Detailed experiments are listed in Table 3.

Table 1. Compositions of flue gas

Species	O_2	CO_2	NO_2	H_2	H_2S	N_2
Vol.%	7.000	11.000	0.005	0.001	0.001	Balance

Table 2. Composition of metal species in 35CrMo

Species		C	Si	Mn	Cr	Mo	P	S	Ni	Fe
Compositions (wt. %)	35CrMo	0.32	0.26	0.56	0.92	0.16	-	-	-	Balance

Table 3. Conditions used for corrosion tests

Run No.	Sample	Pressure (MPa)	Exposure time(h)	Temperature (℃)	Corrosion medium
1	35CrMo	9	24	120	Flue gas
2	35CrMo	9	48	120	Flue gas
3	35CrMo	9	72	120	Flue gas
4	35CrMo	9	96	120	Flue gas
5	35CrMo	9	24	150	Flue gas
6	35CrMo	9	48	150	Flue gas

7	35CrMo	9	72	150	Flue gas
8	35CrMo	9	96	150	Flue gas
9	35CrMo	9	24	200	Flue gas
10	35CrMo	9	48	200	Flue gas
11	35CrMo	9	72	200	Flue gas
12	35CrMo	9	96	200	Flue gas
13	35CrMo	9	24	250	Flue gas
14	35CrMo	9	48	250	Flue gas
15	35CrMo	9	72	250	Flue gas
16	35CrMo	9	96	250	Flue gas

3 Results and discussion

Experimental samples are morphologically analysed. The samples exposed at different temperatures at 9 MPa for 96 h were taken as examples to investigate the effect of temperature on the corrosion behaviours of alloy 35CrMo.

3.1 Increase in diffusion rate

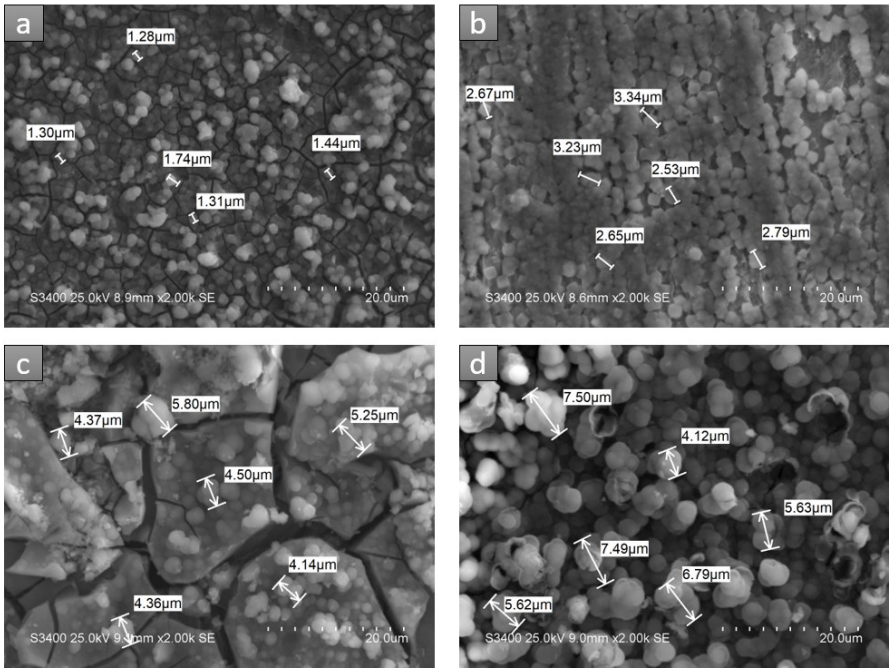

Fig. 1. Corrosion morphology of alloy 35CrMo exposed at (a) 120 ℃, (b) 150 ℃, (c) 200 ℃ and (d) 250 ℃ at 9 MPa for 96 h.

Fig. 1 shows varied corrosion morphology of alloy 35CrMo exposed at four different temperatures at 9 MPa for 96 h. According to Fig. 1(a), there are dense spherical oxides on the sample's surface after exposure at 120 ℃ for 96 h and no serious oxidation or dissolution is detected. At 150 ℃, a continuous corrosion film has been found at the surface and the diameter of spherical oxide is larger than that at 120 ℃. In Fig. 1(c), the oxidation film is thicker and the distance between cracks can be seen. With mean diameter changing

from 4.74 μm at 200 ℃ to 6.19 μm at 250 ℃, the phenomenon of larger spherical oxides and wider cracks appearing in Fig. 1(c) becomes more distinct in Fig. 1(d). The influence of moderate temperature range, represented by four distinct temperatures, is mainly reflected in the promotion of diffusion. It can be observed from the morphology that the size of spherical oxides and the thickness of oxide films are increasing with increasing temperature, which indicates that higher temperature can accelerate the diffusion rate of both alloy ions and corrosive gases.

3.2 Changes in the appearance of oxides

In addition to increase in diffusion, temperature can also affect the stability of oxides, which is reflected by the change of the morphology. At relatively high temperature, oxygen and solute change from lattice diffusion to grain boundary diffusion. Oxides are easy to precipitate and then grow up along the grain boundary, bringing on rod-like and lamellar structure. At higher temperature, iron ions and atoms directly spread out from the lattice, resulting in the emergence of larger spherical particles. Fig. 2 indicates the corrosion morphology of 35CrMo at 150 ℃ and 250 ℃ and both take on totally different oxidation appearance. At 150 ℃, diffusion mostly happens in intergranular space, leading to the generation of needle-like oxides, which possess high density and strong corrosion resistance. On the contrary, the oxidation appearance of the right picture shows that oxides have turned to sphere.

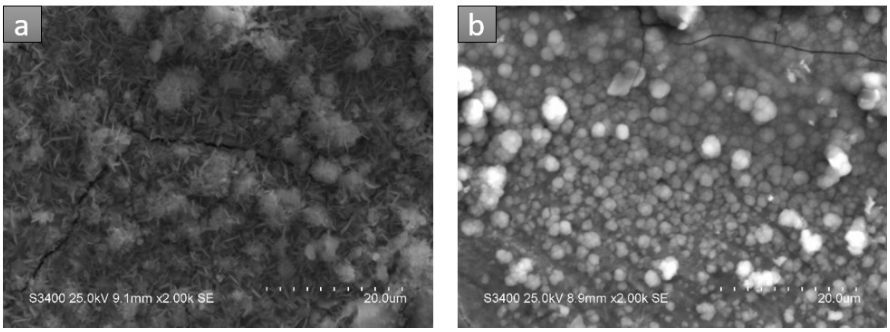

Fig. 2. Corrosion appearance of 35CrMo exposed at (a) 150 ℃ and (b) 250 ℃ at 9 MPa for 48 h

4 Conclusions

In this paper, after exposure in flue gas for 24 h, 48 h, 96 h and 120 h respectively, the effects of moderate temperature on alloy 35CrMo used for casing and pipeline in oil field are studied at same pressure and flue gas environment. Then, by using scanning electron microscopy (SEM), corrosion morphology analyses are achieved and main conclusions are listed as follows.

The typical corrosion behaviour of low temperature corrosion initiated by SO_2 and high temperature corrosion initiated by SO_2 and CO_2 did not appear at four chosen temperature points (120 ℃, 150 ℃, 200 ℃ and 250 ℃). With the increase of temperature, the nucleation rate of oxide particles almost keeps constant, but the growth rate of oxide particles is accelerated, resulting in larger particle size. As we already mentioned in the increase in the diffusion rate, the diffusion activation energies of iron ions and atoms, oxygen ions in the matrix and oxides are diverse, and temperature is one of the key factors to satisfy the need of the diffusion activation energy of these elements. That is to say, the

increase of temperature will improve the diffusion ability of iron ions and atoms and oxygen, so that the reactions take place that should not have happened.

Besides, temperature will affect the stability of oxides, and the consequences will be reflected on the morphology. At low temperature, oxygen and solute change from lattice diffusion to grain boundary diffusion. The oxides are easy to precipitate and grow up along the grain boundary, leading to rod-like and lamellar structures. At high temperature, the intensified diffusion of iron ions and atoms changes the appearance of oxides by resulting in bigger oxide particles and thicker oxide films, even the transmission from needle-like oxides to spherical oxides.

This research is supported by the Fundamental Research Funds for the Central Universities [xjj2018201] and [xjj2018006], the Projects from National Natural Science Foundation of China [51871179].

References

1. L. Li, Y. Zhan, C. Fu, Review of heavy oil recovery methods, Silicon Valley, **12**, 86-87 (2008)
2. P. Pan, H. Chen, Z. Liang, Q. Zhao, Desulfurized flue gas corrosion coupled with deposits in a heating boiler, Corros Sci, **131**, 126-136 (2018)
3. L. Chao, *Optimization of corrosion resistant materials in low-temperature boiler flue gas*, (North China Electric Power University, Beijing, 2015)
4. Q. Fan, *Boiler Principle* (China Electric Power Press, Beijing, 2008)
5. J. Yang, S. Wang, X. Tang, Effect of low oxygen concentration on the oxidation behaviour of Ni-based alloys 625 and 825 in supercritical water, J. Supercrit. Fluids, **131**, 1-10(2018)

Effect of Components Thickness on Heat and Mass Transfer Phenomena in Single Cell of PEFC Operated at High Temperature

Akira Nishimura[1,*], *Satoru* Kamiya[1] , *Tatsuya* Okado[1], *Yusuke* Sato[1] and *Masafumi* Hirota[1]

[1]Divison of Mechanical Engineering, Mie University, 514-8507 Tsu, Japan

Abstract. Since the heat transfer characteristics in Polymer Electrolyte Fuel Cell (PEFC) influences its power generation performance, this study clarifies the temperature characteristics to in-plane direction in single PEFC. In addition, since we expect the heat and mass transfer as well as power generation characteristic are enhanced by decreasing PEM and GDL's thicknesses, it is effective to investigate the impact of components thickness on them under high temperature operation. This study aims to clarify how to influence PEM and GDL's thicknesses on not only heat and mass transfer characteristics but also power generation characteristic under high temperature, e.g., 90 ℃. The present study measured temperature distributions to in-plane direction on cathode separator back of cell by thermograph with power generation changing initial operation temperature as well as relative humidity of inflow gases. As a result, the increase in generated power and the even temperature distribution were obtained due to the decrease in GDL's thickness. Since the moisture transfer was promoted with decreasing the thickness of PEM, the power generation performance was improved. It was clarified that the impact of GDL's thickness was larger than that of PEM's thickness. **Keywords:** PEFC, thermal management, measurement by thermograph, high temperature target, components thickness

1 Introduction

PEFC (formally, it is Polymer Electrolyte Fuel Cell) is generally operated using polymer electrolyte membrane (PEM) such as Nafion at the temperature from 60 ℃ to 80 ℃ [1, 2].

In japan, the operation temperature is requested to be increased up to 90 ℃ for the usage of stationary PEFC from 2020 to 2025 [3]. If we can operate PEFC under higher temperature condition, the merits can be believed as follows: (1) electrochemical kinetics are enhanced for anode and cathode electrodes; (2) the cooling stack system can be downsized by utilizing the larger temperature gap between stack of PEFC and coolant; (3) the tolerability of CO is improved and the lower quality reformed hydrogen can be available [4]. If we want to develop the PEFC system at higher temperature condition, it is necessary to clarify

* Corresponding author: nisimura@mach.mie-u.ac.jp

heat and mass transfer mechanisms for increase in the power generated and the system stability.

The present study focuses on the temperature distribution to in-plane direction in a cell of PEFC since PEM (Proton Exchange Membrane) is decomposed thermally by local hot spot and PEM is destroyed due to thermal stress caused by non-uniform temperature distribution [5, 6]. In addition, some problems, e.g., water flooding, membrane dehydration and cell failure because of superheating are caused by temperature distribution at each point [7]. Therefore, it is necessary to manage the heat transfer in PEFC, especially under high temperature operation. Although it is known that thermocouple is used for temperature measurement, thermocouple influences the power generation as well as accuracy of measured temperature remarkably because of gases leakage [8, 9]. From this consideration, a thermograph is promising temperature measurement way under the power generation condition with more accuracy and non-disturbance of temperature and mass distribution since it can measure by a non-contract and in-situ procedure. According to past studies, temperature distributions measured by thermograph were reported only at relatively lower temperature below 60 ℃ and with dry gas supply [6, 10, 11]. There was no study revealing the temperature distribution at high temperature over 80 ℃, except the research carried out by the authors [12, 13].

Furthermore, there is a few study investigating the effect of PEM and GDL (Gas Diffusion Layer)'s thicknesses on heat and mass transfer characteristics as well as power generation characteristic at high temperature such as 90 ℃ though PEM and GDL's thicknesses influence them [14, 15, 16]. Since it is believed to promote not only the heat and mass transfer but also power generation performance by decreasing PEM and GDL's thicknesses, it is effective to investigate the impact of components thickness on them under high temperature operation for the management of heat transfer in the cell.

Therefore, this study aims to clarify the impact of PEM and GDL (Gas Diffusion Layer)'s thicknesses on not only temperature and mass distributions but also power generated at high temperature such as 90 ℃. This study measured the temperature distributions to in-plane direction on cathode separator back by means of thermograph with power generation changing pre-setup initial temperature of cell (= the temperature of inflow gas) and relative humidity of inflow gas. To evaluate the performance of PEFC, the voltage and local current were also measured.

2 Experimental

2.1 Set-up and method

This study used one cell of PEFC (MC-25-SC-NH produced by Reactive Innovations). This study adopted Nafion 115, Nafion211 (produced by DuPont Corp.) whose thicknesses were 127 μm and 25 μm as PEM. In addition, this study also used TGP-H-060 and TGP-H-030 (produced by Toray Corp.) whose thicknesses were 190 μm and 110 μm as GDL. Table 1 exhibits the specifications of cell components. Fig 1 shows the procedure of temperature measurements. The dimension of the hole for observation was 50 mm and 50 mm which was same as the electrode. The hole whose dimension was 40 mm and 50 mm was opened in hot water passage plate, where the water for heating didn't flow exactly.

We measured the temperature distribution to in-plane direction on the cathode separator back by the hole for observation and thermograph (Thermotracer TH9100WL produced by NIPPON AVONICS Co., Ltd.). In addition, we analysed the temperature data using the

dedicated software (TH91-702 produced by NIPPON AVIONICS Co., Ltd.). We fitted a black body tape (HB-250 produced by OPTIX) on the separator back to prevent measurement inaccuracy caused by surface roughness and reflection variation. Since it was necessary to know the emissivity of black body tape used for power generation experiment, we measured it pre-experimentally. From the pre-experiment, it was clear that the impact of the observation window on power generation output was very little. The pre-set initial temperature of one cell was 70 ℃ and the relative humidity of both inflow gases was 80 %RH (with and without hole for observation) as pre-experimental conditions [12, 13]. According to the results of the pre-experiment, it was revealed that voltage drops due to observation window during the anode and cathode observation experiments loading the current density of 0.80 A/cm^2 were only 4 % and 7 %, respectively.

Table 1. Specifications of cell components used in this study.

Components	Dimension	Information
PEM (Polymer Electrolyte Membrane)	Width is 50.0 mm, height is 50.0 mm, thicknesses are 0.127, 0.025 mm.	Nafion115, Nafion211 (Produced by DuPont Corp.)
Catalyst layer	Width is 50.0 mm, height is 50.0 mm (fitted on PEM).	Pt loaded on carbon (Loading ratio of Pt is 20 wt%.)
GDL (Gas Diffusion Layer)	Width is 50.0 mm, height is 50.0 mm, thicknesses are 0.190, 0.110 mm.	TGP-H-060, TGP-H-030 (Produced by Toray Corp.)
Gas separator	Width is 75.4 mm, height is 75.4 mm, thickness is 2.00 mm (The area whose width is 50.0 mm and height is 50.0 mm is for gas supply.)	Made by carbon graphite, Serpentine flow
Hot water passage plate	Width is 75.4 mm, height is 75.4 mm, thickness is 2.00 mm.	Made by carbon graphite
Current collector	Power generation area is 6937 mm^2, thickness is 2.00 mm.	Made by copper coated with gold
End block	Width is 110 mm, height is 110 mm, thickness is 12.7 mm.	Made by alumina

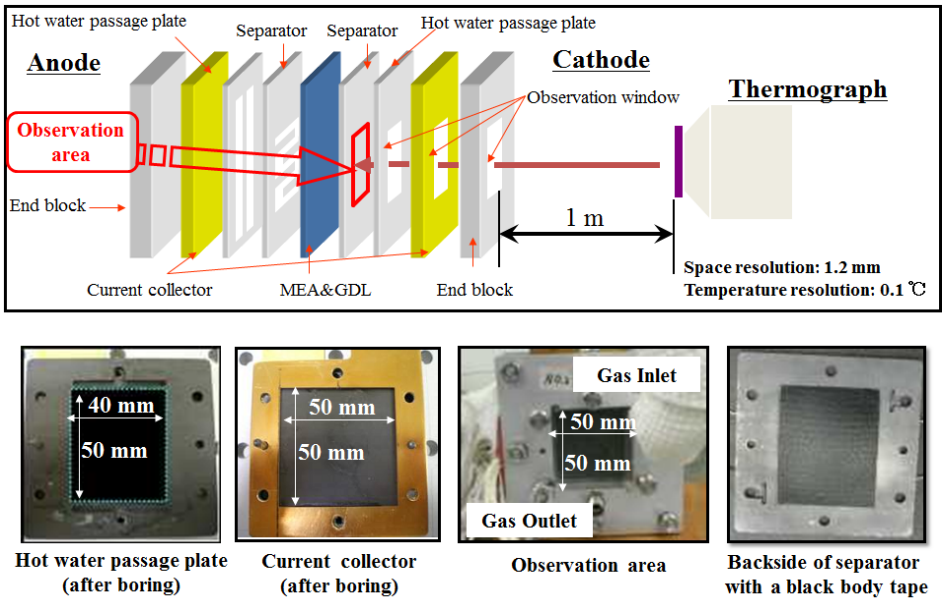

Fig. 1. Cell structure to measure temperature by thermograph.

We covered all sides of the cell without the observation window side and the opposite side by heat insulator. We measured the temperature distribution to in-plane direction caused by reaction heat by means of thermograph and set the current density at 0.80 A/cm^2 since the temperature of one cell could be kept over the pre-set initial temperature without heat input from electric heater [12, 13]. According to the brochure of manufacture, PEM, GDL and separator have the thermal conductivities of 0.195, 1.7 and 25 W/(m · K), respectively. On the other hand, hot water passage plate, current collector and end block have the thermal conductivities of 25, 380 and 220 W/(m·K), respectively. Therefore, the thermal conductivities of the latter located outside of separator are much larger than those of the former, resulting in no impact on the temperature distribution by ambient air [12, 13]. When the hot water passage plate which was assembled in advance was not installed, the gas leakage had occurred. Therefore, we installed hot water passage plate to prevent gas leakage though the water for heating was not flowed.

Table 2 shows the experimental operation conditions and parameters. Fig. 2 illustrates the experimental set-up. To keep the same as pre-set initial temperature of cell (T_{ini}), we controlled the temperatures of inflow gases. We also controlled the relative humidity of inflow gases by humidifiers and dew point meters (MHT337FC produced by VAISALA). We set the flow rates of inflow gases at the stoichiometric ratios of 1.5, 2.0 and 3.0. In the present study, we applied pure H_2 and pure O_2 for the anode and the cathode. We controlled the flow rate of inflow gases using the mass flow controller (5850E produced by BROOKS INSTRUMENT). The flow rate of inflow gas whose stoichiometric ratio is 1.0 is defined by Eq. (1).

$$C_{H2} = I/nF \tag{1}$$

where C_{H2} indicates the molar flow rate of H_2 (mol/s), I indicates the load current (A) = (C/s), n indicates the valence ion (= 2) (-), F indicates Faraday constant (= 96,500) (C/mol). C_{H2} is same as the amount of H_2 whose stoichiometric ratio is 1.0. From Eq. (2), C_{O2} indicates the molar flow rate of O_2 (mol/s) which equals to a half of C_{H2}.

$$H_2 + 1/2O_2 = H_2O \quad (2)$$

We controlled the load current of PEFC by the electric device (PLZ603W produced by KIKUSUI ELECTRONICS CORP.). We measured the total voltage according to the load current controlled by the electric load device.

We heated the cell for start-up by electric heaters (Silicon rubber heater MG produced by OM Heater) installed around the end block. We also heated H_2 and O_2 at T_{ini} before suppling into the cell in this start-up process. After attaining at T_{ini}, we started the power generation changing the load. The flow rates of inflow and outflow gases as well as temperature distribution were maintained a static state over 30 min keeping to load the current.

Table 2. Experimental operation conditions.

Pre-set initial temperature (T_{ini}) (°C)	80, 90	
Load current (A) (Current density (A/cm^2))	0 - 20 (0 - 0.80)	
Inflow gas conditions		
	Anode	Cathode
Gas characteristics	H_2 whose purity is 99.995 vol%	O_2 whose purity is 99.995 vol%
Temperature of inflow gas (°C)	80, 90	80, 90
Relative humidity of inflow gas (%RH)	40, 80	40, 80
Pressure of inflow gas (absolute) (MPa)	0.4	0.4
Flow rate of inflow gas (NL/min) (Stoichiometric ratio (-))	0.210, 0.280, 0.420 (1.5, 2.0, 3.0)	0.105, 0.140, 0.210 (1.5, 2.0, 3.0)

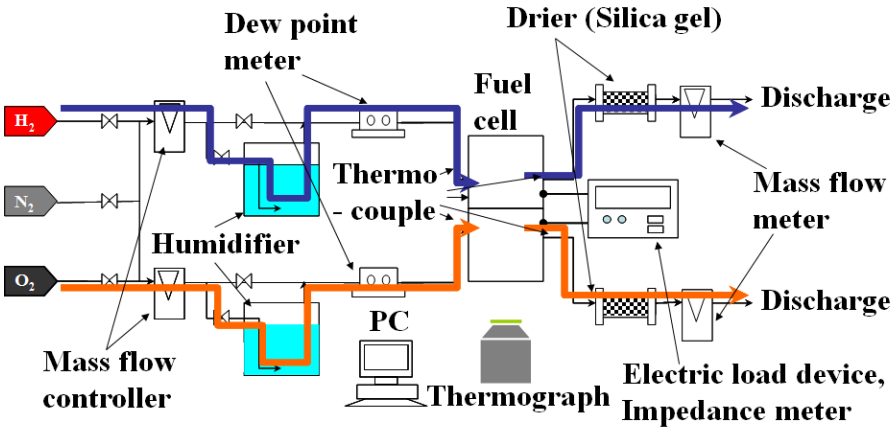

Fig. 2. Schematic diagram of experimental set-up.

2.2 Evaluation procedure of temperature image

The present study analysed the temperature image, which was obtained using the thermograph, by dividing into segment. Fig. 3 indicates the image of temperature distribution to in-plane direction divided into the area which has the vertical length of 10 mm and the horizontal length of 10 mm. The number of areas was 20 from A to T according to the gas flow along gas channel. We calculated the mean temperature in each area using the temperature image. We averaged temperatures of the areas of A and T by removing the area where the heat insulator covering the gas pipe disturbed to detect the infrared ray by thermograph.

This study applied the temperature difference $T_i - T_{ave}$ (°C) to evaluate the temperature distribution to in-plane direction objectively. T_i indicates the average temperature in each area (A to T). T_{ave} indicates the average temperature in all areas.

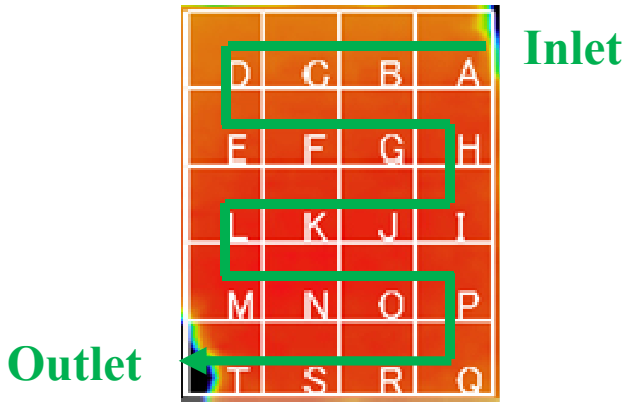

Fig. 3. Segmentation of the temperature image.

3 Results and discussion

3.1 Impact of GDL thickness

Figs. 4 and 5 show polarization curves of two different GDLs under various relative humidity conditions at T_{ini} = 80 and 90 °C, respectively. Nafion115 was used as PEM in these experiments. According to these figures, TGP-H-030 showed a small voltage drop under high current density condition compared with TGP-H-060 regardless of T_{ini} and relative humidity. It is believed that the moisture transfer was promoted due to thin GDL (TGP-H-030), resulting that the good humidification was obtained even under high temperature and low humidity condition. Therefore, it can be considered that the promotion of moisture transfer contributes to the increase in the power generated.

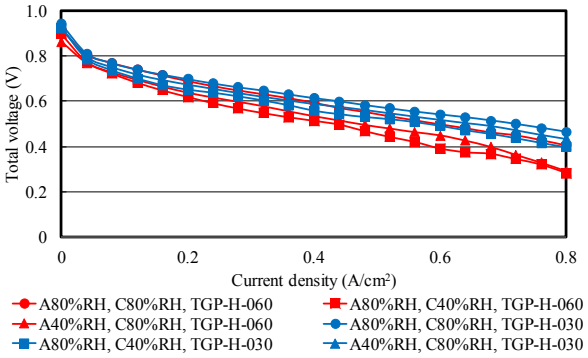

Fig. 4. Polarization curves of two different GDLs under various relative humidity conditions in the case of T_{ini} = 80 ˚C.

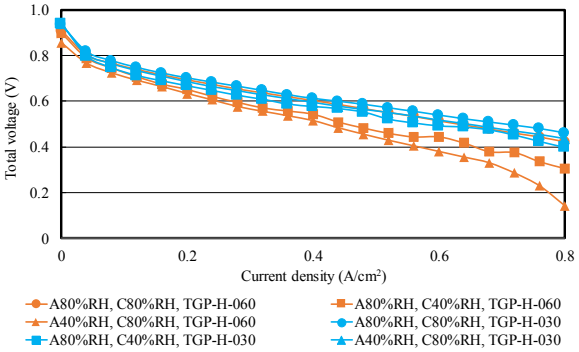

Fig. 5. Polarization curves of two different GDLs under various relative humidity conditions in the case of T_{ini} = 90 ˚C.

Figs. 6 and 7 show the temperature distribution to in-plane direction on cathode side with Nafion115 changing GDL and relative humidity of inflow gas in the case of T_{ini} = 80, 90 ˚C. Results for the stoichiometric ratio of 1.0 are shown in these figures since there is a few difference among various stoichiometric ratio conditions. According to these figures, it is seen that the temperature rose from the inlet to the outlet in the case of TGP-H-060. As the generated water accumulated, the PEM was humidified well with the gas flow, resulting in the improvement of power generation performance. As to TGP-H-030, the temperature distribution was relatively flat regardless of T_{ini} and relative humidity condition. According to the brochure of GDL [17], the gas permeability of TGP-H-060 and that of TGP-H-030 are 1900 ml·mm/(cm^2·hr·mmAq) and 2500 ml·mm/(cm^2·hr·mmAq), respectively. Since the gas permeability increased with decreasing the thickness of GDL, the gas was diffused uniformly, resulting that the temperature variation was reduced. Consequently, it is clarified that the generated power was increased by decreasing GDL's thickness. In addition, the temperature distribution became even because of decreasing GDL's thickness.

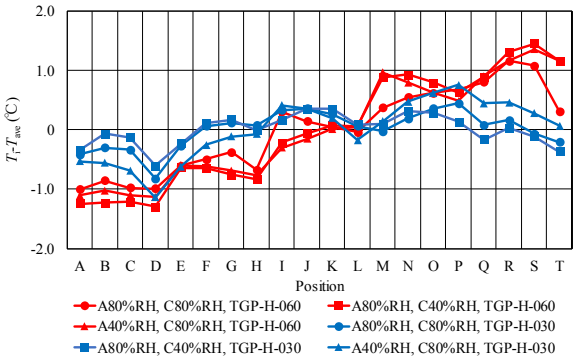

Fig. 6. Comparison of temperature distribution to in-plane direction on the cathode side in the case of T_{ini} = 80 ℃ using Nafion115 among different GDLs.

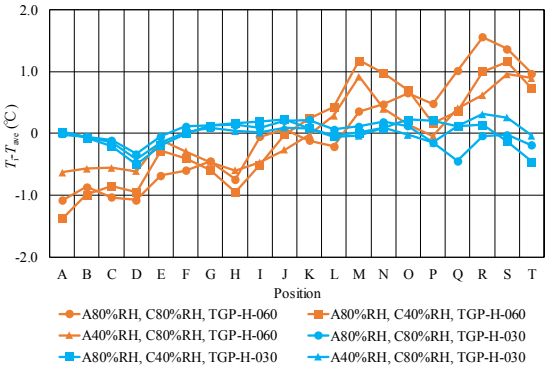

Fig. 7. Comparison of temperature distribution to in-plane direction on the cathode side in the case of T_{ini} = 90 ℃ using Nafion115 among different GDLs.

3.2 Impact of PEM thickness

Fig. 8 shows polarization curves of two different PEMs under various relative humidity conditions in the case of T_{ini} = 90 ℃. According to Fig. 8, it is seen that the voltage was higher wholly and the voltage drop under low humidity conditions was smaller for Nafion211 compared with Nafion115. Thinner PEM has an advantage of power generation performance which is the same as the previous study carried out at 80 ℃ [14]. The moisture transfer was promoted with decreasing PEM's thickness, resulting that the power generation performance was improved, especially under high current density condition which would cause the flooding and plugging easily.

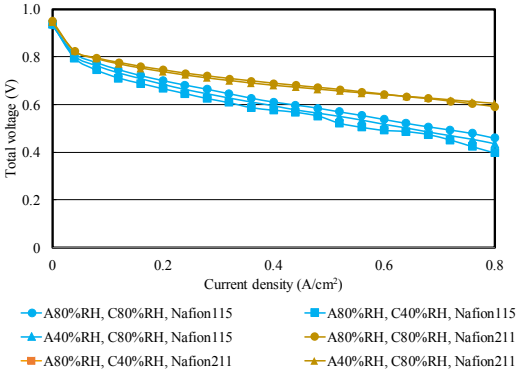

Fig. 8. Polarization curves of two different PEMs under various relative humidity conditions in the case of T_{ini} = 90 ˚C.

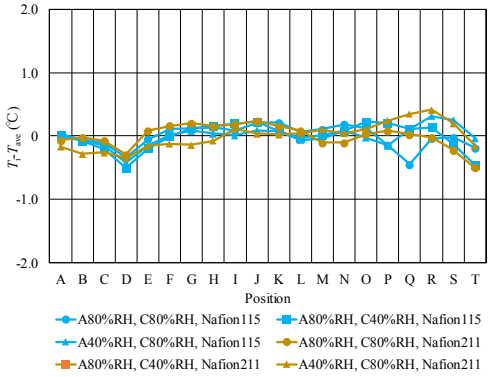

Fig. 9. Comparison of temperature distribution to in-plane direction on the cathode side in the case of T_{ini} = 90 ˚C using TGP-H-030 among different PEMs.

Fig. 9 shows the temperature distribution to in-plane direction on cathode side in the case of T_{ini} = 90 ˚C with TGP-H-030 changing PEM and relative humidity of inflow gas. From Fig. 9, the temperature distribution was flat irrespective of relative humidity condition as well as PEM. It is believed that the moisture transfer for both PEM was sufficiently promoted due to thin GDL. Consequently, it is revealed that the impact of GDL's thickness was larger than that of PEM's thickness.

4 Conclusion

In this study, the impact of PEM and GDL's thicknesses on heat and mass transfer characteristics as well as power generation characteristic was analysed to realize high temperature operation such as 90 ˚C. As a result, this study obtained the conclusions as follows:

(1) Thin GDL (TGP-H-030) showed a small voltage drop under high current density condition compared with thick GDL (TGP-H-060) regardless of T_{ini} and relative humidity since the moisture transfer was promoted.
(2) The temperature rose from the inlet to the outlet for thick GDL, while the temperature distribution was relatively flat regardless of T_{ini} and relative humidity condition for thin GDL.
(3) The increase in generated power and the even temperature distribution were obtained due to the decrease in GDL's thickness.
(4) The voltage was higher wholly and the voltage drop under low humidity conditions was smaller for Nafion211 compared with Nafion115. Since the moisture transfer was promoted with decreasing PEM's thickness, the power generation performance was improved.
(5) When using thin GDL, the temperature distribution was flat irrespective of relative humidity condition as well as PEM.
(6) It is revealed that the impact of GDL's thickness was larger than that of PEM's thickness.

References

1. G. Zhang, S. G. Kandlikar, Int. J. Hydro. Ener. **37**, 2412-2429 (2012)

2. K. Agbossou, M. Kolhe, J. Hamelin, T. K. Bose, IEEE Trans. Ener. Conv. **19**, 633-640 (2004)

3. New Energy and Industrial Technology Development Organization (NEDO), http://www.nedo.go.jp/news/press/AA5_100889.html (accessed on September 4, 2018)

4. Q. Li, R. He, J. O. Jensen, N. J. Bjerrum, Chem. Mat. **15**, 4896-4915 (2003)

5. K. Tsuji, Hydro. Ener. Sys. **33**, 93-96 (2008)

6. M. Wang, H. Guo, C. Ma, J. Pow. Sour. **157**, 181-187 (2006)

7. G. Zhang, L. Guo, L. Ma, H. Liu, J. Pow. Sour. **195**, 3597-3604 (2010)

8. T. Ogawa, N. Hohara, T. Chikahisa, Y. Hishimura, *Proc. 41st National Heat Transfer Symposium of Japan*, 235-236 (2004)

9. T. Ogawa, T. Chikahisa, K. Kikuta, *Proc. Thermal Engineering Conference*, 483-484 (2003)

10. A. Hakenjos, H. Muenter, U. Wittstadt, C. Hebling, J. Pow. Sour. **131**, 213-216 (2004)

11. T. Ogawa, N. Hohara, T. Chikahisa, Y. Nishimura, Therm. Sci. Eng. **23**, 93-94 (2004)

12. A. Nishimura, M. Yoshimura, A. M. Mahadi, M. Hirota, M. Kolhe, Mech. Eng. J. **3**, 1-14 (2016)

13. A. Nishimura, M. Yoshimura, S. Kamiya, M. Hirota, E. Hu, J. Eng. Pow. Eng. **11**, 706-718 (2017)

14. T. E. Springer, T. A. Zawodzinski, S. Gottesfeld, J. Electrochem. Soc. **138**, 2334-2341 (1991)

15. Z. Penga, I. Tolj, F. Barbir, Int. J. Hydro. Ener. **41**, 17585-17594 (2016)

16. J. Yablecki, A. Bazylak, J. Pow. Sour. **217**, 470-478 (2012)

17. TORAY, http://www.torayca.com/lineup/composites/com_009_01.html (accessed on September 6, 2018)

Effects of cesium-substituted silicotungstic acid doped with polybenzimidazole membrane for the application of medium temperature polymer electrolyte fuel cells

Kyaw Zay Ya[1], Pascal Nbelayim[1], Wai Kian Tan[2], Go Kawamura[1], Hiroyuki Muto[1,2], and Atsunori Matsuda[1*]

[1]Department of Electrical and Electronic Information Engineering, Toyohashi University of Technology, 1-1 Hibarigaoka, Tempakhu-cho, Toyohashi, Aichi 441-8580, Japan
[2]Institute of Liberal Arts and Sciences, Toyohashi University of Technology, 1-1 Hibarigaoka, Tempaku-cho, Toyohashi, Aichi 441-8580, Japan

Abstract. Inorganic-organic composite membranes were prepared by using partly cesium-substituted silicotungstic acid (CHS-WSiA) and polybenzimidazole (PBI, MRS0810H) for medium temperature polymer electrolyte fuel cells (MT-PEFCs). Cesium hydrogen sulfate ($CsHSO_4$, CHS) and silicotungstic acid ($H_4SiW_{12}O_{40}$, WSiA) were milled to obtain 0.5CHS-0.5WSiA composites by dry and wet mechanical millings. *N,N*-dimethylacetamide (DMAc) was used as a disperse medium in the preparation of the inorganic solid acids by wet mechanical milling and also a casting agent for fabrication of membrane. Finally, flexible and homogeneous composite membranes with several phosphoric acid doping levels (PADLs) were obtained. The wet mechanical milling using DMAc was found to effectively promote good substitution of H^+ ion in WSiA by Cs^+ ion of CHS and promoted the formation of smaller grain sizes of composites, compared with dry milling. A high maximum power density of 378 $mWcm^{-2}$ and a good constant current stability test were obtained from a single cell test using the PBI composite membrane containing 20 wt% of 0.5CHS-0.5WSiA from wet milling and phosphoric acid doping level (PADL) of 8 mol, at 150 ^oC under an anhydrous condition. Wet milling CHS-WSiA crystallites were highly dispersed in PBI to give homogenized membranes and played a significant role in the enhancemance of acidity by increasing the number of proton sites in the electrolyte membrane. After the addition of CHS-WSiA into PBI membrane, the acid and water retention properties were improved and incorporated as new proton conduction path by adsorbing phosphoric acid in these composite electrolyte membranes. These observations suggest that composite membranes with 8 mol of PADL are good promising PA doped-membranes with effective electrochemical properties for the medium temperature fuel cells.

1 Introduction

Presently, environmental safety is of significant importance for human beings as well as the lives of future generations. One of the negative impacts of the environment is the large

*[1]Corresponding author: matsuda@ee.tut.ac.jp

usage of electrical energy which increases day by day. In our daily lives, people need energy, and the primary sources of energy are provided via the combustion of fossil fuels, which leads to high levels of air pollution and the emission of greenhouse gasses [1]. To solve these challenges, new energy production technologies have to be developed for future energy production. So, fuel cells are the great promise for new energy production. The fuel cell can make directly conversion from chemical energy to electrical energy as an electrochemical cell between fuels. Fuel cells are one of power generation with high interest because they can perform to enhance power conversion efficiency with a reduction of pollution levels. In particular, the electrolyte membrane is a main component in fuel cell performance to generate electrical power [2]. Polymer electrolyte membrane fuel cells (PEMFCs) contain perfluorosulfonic acid electrolyte such as Nafion® which is one of the most production methods of clean energy and are explored for usage as power sources for energy converters. They present positive characteristics, such as high performance like power density and conductivities, good efficiency and tolerance of pollutant levels. But, PEMFCs need humid condition for proton generation with low fuel cell performance and efficiency under the operating temperature (< 100 ^{o}C). So, to enhance the fuel cell performance and power efficiency for PEMFCs, a high operating temperature and kinematic reaction are required for high fuel cell efficiency [3-10]. After increasing the operating temperature (>100 ^{o}C) for PEMFCs, they are improved with high kinematic reaction, higher tolerance for impurities in the fuel stream, and affable thermal-water maintainance. Polybenzimidazole (PBI) is the most attractive water insoluble polymer among the non-fluorinated ionomers (non-PFI) under active development because it shows good properties not only electronic but also as an ionic insulator. In addition, PBI have also attracted positive attention because of their high mechanical properties and thermal stablility. However, after pristine PBI membrane is doped with phosphoric acids (PA), mechanical strength of PBI membrane was reduced with the higher the acid content in PBI. And hence, PBI membranes with large amount of acid doping might happen higher acid leaching comparing with lower amount of acid doping PBI membrane in fuel cell applications. Inorganic composite doped-PBI membranes can make high tolerance acid leaching problems and enhance the proton conduction path in PBI [11-15].

Partially cesium-substituted heteropoly acids have attracted good interest due to their high catalytic properties with high proton conductivity in many acid-type reactions. Acidic or anhydrous inorganic compounds were mainly used for the performance enhancing of inorganic solid-state proton conductor. Inorganic solid-state composites produced by high mechanical milling treatment shows a high potential method that improves the proton conductivity of inorganic composite materials and reduces particle sizes [16-22]. Hence, fabrication of inorganic composites have been focused on the factors of low-cost, high-performance, medium temperature (at around 150 ^{o}C)-resistant for high temperature PEMFCs (MT-PEMFCs). Introducing solid acid composites (e.g. $CsHSO_4$-$H_4SiW_{12}O_{40}$) into the PBI membrane performs to improve absorption capability of PA and supports to prevent acid leaching of PA at high temperature [23].

In this research, CHS-WSiA composite was created to enhance the anhydrous proton conductivity and reduce the particle sizes via wet mechanical milling as inorganic fillers for the application of membrane fabrication. For the MT-PEMFCs, proton conductivities and cell performances of CHS-WSiA/PBI membranes were improved after fabrication of composites doped-PBI.

2 Experimental Procedure

Reagent grade cesium hydrogen sulfate ($CsHSO_4$, CHS) (Sokawa Chemical Co.Ltd., Japan) and silicotungstic acid ($H_4SiW_{12}O_{40}$, WSiA) (Wako Pure Chemical Industries, Japan) were purchased to fabricate CHS-WSiA composite materials. To synthesize 0.5CHS-0.5WSiA dry composite materials, the planetary dry milling was carried out under a dry nitrogen atmosphere using a planetary ball mill (Purverisette 7, Fritsch) with an agate pot (45 mL) and agate balls (10 balls of 10 mm diameter) at 720 rpm and a rotation ratio of 1:1 for 1 h. After dry milling, these composites were collected from the mechanical milling pot and were heated at 80 ^oC in a vacuum oven overnight to obtain dry and fine composite powders. On the other hand, to fabricate 0.5CHS-0.5WSiA wet composites, *N,N*-Dimethylacetamide (DMAc, 5 mL) (Wako; 99 %) was used as solvent/disperse media at 300 rpm for 1 h. After mechanochemical wet milling, the composite precursors were dried at 60 ^oC overnight in an oven to remove hydrated water and DMAc from the sample. Then, it was also heated at 80 ^oC for 3 h in a vacuum oven to obtain more dry and fine composite powders. A schematic diagram for *x*CHS-(1-*x*)WSiA composites produced by wet mechanical milling method was shown in Fig 1[24,25].

For electrolyte membrane fabrication, DMAc (43.23 g) and polybenzimidazole solution (PBI, MRS0810H) (1wt%, 4.8 g) were used to cast pristine PBI membrane.

Before membrane casting, a magnetic stirrer and a sonicator were used to stirr PBI solution at 500 rpm for 1 h and sonicate for 30 min. Then, petri dish (φ = 9.7 cm) was used to cast PBI membrane solution under the temperature (60-120 ^oC) for 24 h drying. Hot-water durability test was also performed for PBI membrane to eliminate residual materials and DMAc solvent at 90 ^oC for 5 h. Finally, it was dried to evaporate hydrated water from membrane under dry temperature (at 60 ^oC) overnight.

20 wt% of CHS-WSiA composites was added into PBI solution to fabricate CHS-WSiA/PBI membranes under the same fabrication method of pristine PBI membrane, at weight percent (PBI:CHS-WSiA, 5:1 wt%), before casting.

Finally, PA doping of CHS-WSiA/PBI membranes and pristine PBI membrane was performed by immersing into 85 % of PA (Wako) and heated at 60 ^oC for desired PA doping levels (PADLs). Prior to conductivity and fuel cell measurement, PA doped membranes were heated at 60 ^oC for 1 h to eliminate excess PA and water.

X-ray diffraction (XRD; RINT 2200, Rigaku) patterns of the mechanochemically fabricated Cs-substituted WSiA composites from dry and wet milling were evaluated at room temperature (RT).

The morphologies of the CHS-WSiA composite powders, CHS-WSiA/PBI membranes, and pristine PBI membrane were measured by using field emission scanning electron microscopy (FE-SEM; S-4800, Hitachi).

AC impedance spectroscopy measurement was performed to evaluate temperature-dependent proton conductivities of all membranes over a frequency range of 10^7-1 Hz (Solartron; SI 1260) under dry nitrogen condition. Before conductivity measurement, composite samples and electrolyte membranes were kept at 150 ^oC for 1 h under N_2 atmosphere. For membrane electrode assemblies (MEAs), commercially 0.5 mg cm^{-2} Pt-loaded carbon papers were used as electrodes. Pt-loaded carbon sheets were prepared the sizes (1 × 1 cm^2) and (1.5 × 1.5 cm^2) for anode and cathode, respectively.

The membranes with PA doping were sandwiched by the Pt-loaded carbon catalysts to set MEAs measurement condition. 100 mL min^{-1} of H_2 and 100 mL min^{-1} of O_2 were applied to supply during FC evaluation. Operating temperature was selected at 150 ^oC for single fuel cell test under dry condition [24, 26].

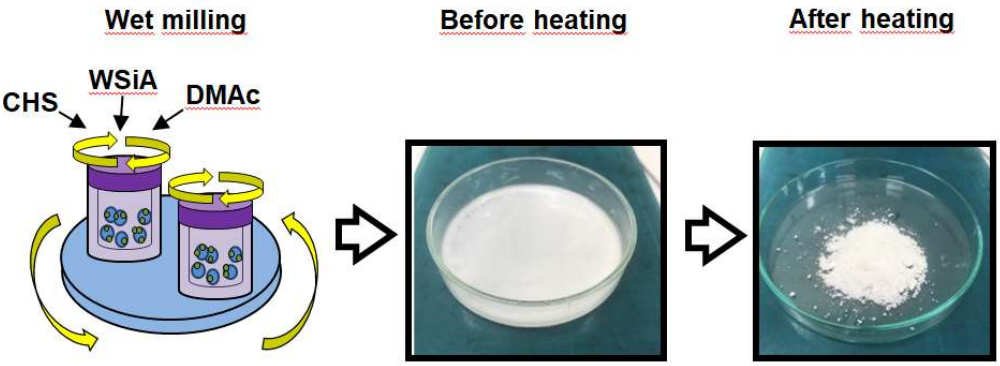

Fig. 1. Schematic diagram for 0.5CHS-0.5WSiA composites produced by wet mechanical milling method.

3 Results and discussion

3.1 Characterization of 0.5CHS-0.5WSiA composites via dry and wet mechanical milling

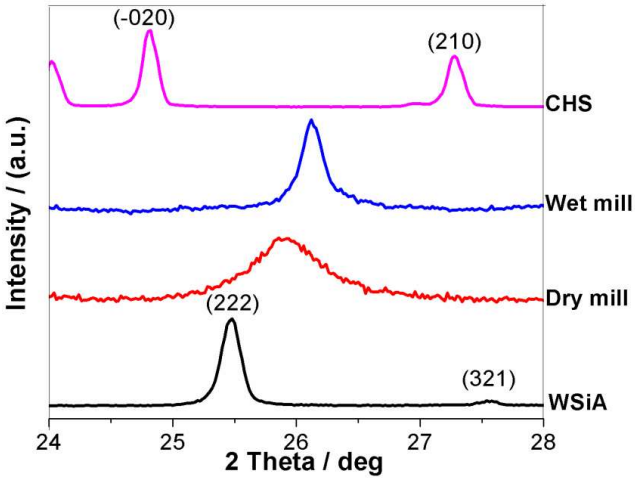

Fig. 2. Powder XRD patterns of WSiA, CHS, 0.5CHS-0.5WSiA (dry milling) and 0.5CHS-0.5WSiA(wet milling) composites.

From XRD measurement, 0.5CHS-0.5WSiA (dry and wet milling) inorganic composites are shown in Fig. 2. Prior to mechanical milling, diffraction peaks of CHS and WSiA in Fig. 2 were well matched with standard JCPS library file. After mechanical dry milling to fabricate $Cs_xH_{4-x}SiW_{12}O_{40}$, noticeable changes are detected in the XRD results from 25.6 ^{o} to 26 ^{o}; and it showed broad diffraction peak comparing with composite fabricated from mechanical wet milling. After mechanical wet milling, the diffraction peak of composite slightly shifted to higher angle; that compared with composite from mechanical dry milling. Both composites synthesized by dry and wet milling showed the highest intensities with the high peak shifting to higher angles which indicates that the H^+ ion in WSiA was partly substituted with large Cs^+ ion in CHS to fabricate $Cs_xH_{4-x}SiW_{12}O_{40}$ via mechanical dry and wet milling.

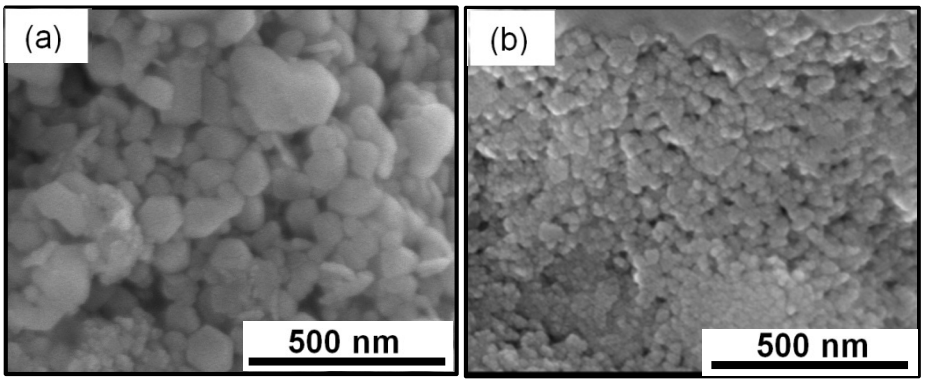

Fig. 3. FE-SEM images of (a) 0.5CHS-0.5WSiA (dry milling) and (b) 0.5CHS-0.5WSiA (wet milling) composites.

Fig. 3(a) and 3(b) show FE-SEM images of 0.5CHS-0.5WSiA (dry milling) and 0.5CHS-0.5WSiA (wet milling) composites. After mechanochemical dry and wet milling, it was seen that the chemical reaction was formed between CHS and WSiA to produce Cs-substituted WSiA composite materials with high proton percolation. 0.5CHS-0.5WSiA (dry milling) and 0.5CHS-0.5WSiA (wet milling) composites showed surface homogeneous and spherical structure as fine composite powders. While 0.5CHS-0.5WSiA (dry milling) composite showed grain sizes at about 50 nm, 0.5CHS-0.5WSiA (wet milling) composite showed at about 20 nm as the grain units. The grain sizes of 0.5CHS-0.5WSiA (wet milling) composites were smaller than 0.5CHS-0.5WSiA (dry milling) composites via a high chemical reaction between CHS and WSiA with the help of DMAc solvent. Composite samples with small particles will support to be a large active surface area and take more acid, which shows good properties of the composites. 0.5CHS-0.5WSiA (wet milling) composites showed good distribution which is more compact than 0.5CHS-0.5WSiA (dry milling) because of the effective DMAc solvent's treatment. According to mechanochemical wet milling, this solvent helps to make an effective chemical reaction between the raw samples and supported to achieve a high proton conduction path in composites.

3.2 **Characterization of CHS-WSiA/PBI and pristine PBI membranes**

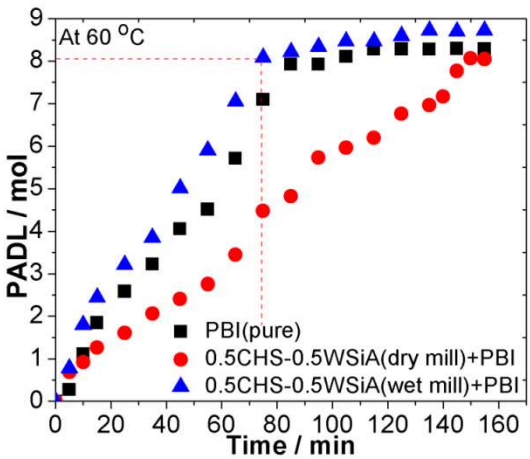

Fig. 4. Time-dependent of PADL for pristine PBI, 0.5CHS-0.5WSiA(dry mill)/PBI, and 0.5CHS-0.5WSiA(wet mill) /PBI membranes, respectively.

Different PADL values of CHS-WSiA/PBI and pristine PBI membranes with different doping time were shown in Fig. 4. For CHS-WSiA(wet)/PBI electrolyte film, after 35 min, PADL value was reached to 4 mol, and 6 mol for 55 min, and then reached to 8 mol during 70 min for FC evaluation. Then, it was slightly increased to be 8 mol over 70 min during PA doping time. 8 mol of PADL was selected to apply for membrane characterization and FC evaluation. On the other hand, after 65 min, 4 mol of PADL was achieved for the CHS-WSiA(dry)/PBI membrane, and 6 mol for 105 min, and then, reached to 8 mol PADL during 150 min. For pristine PBI, it showed 4 mol of PADL within 8 min, and reached to 6 mol during 70 min, and then saturates 8 mol PADL after 85 min. Especially, PA dopants in composite PBI membranes and pristine PBI exist in different forms. For instance, they exist not only chemically reacted PA with nitrogens of imidazole rings in PBI but also physically adsorbed PA in PBI as free acids [10]. CHS-WSiA (wet)/PBI membrane with nonosized-composite materials showed good hygroscopic properties and maintained a large amount of PA after PA doping.

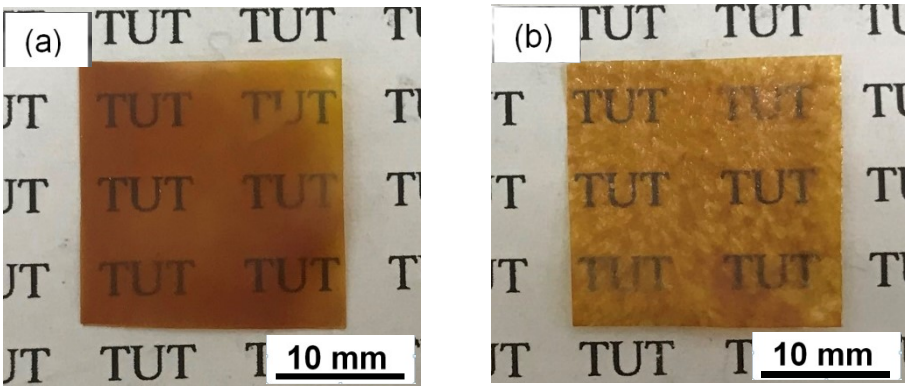

Fig. 5. Photographs of (a) 0.5CHS-0.5WSiA (dry mill) /PBI membrane and (b) 0.5CHS-0.5WSiA (wet mill) /PBI composite membranes.

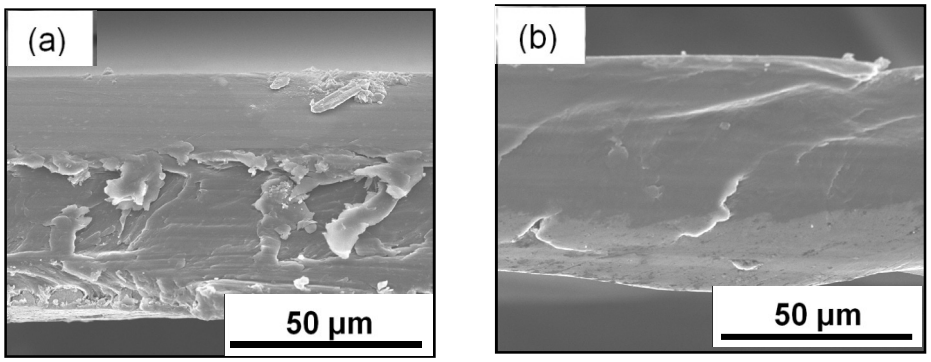

Fig. 6. Cross-sectional FE-SEM images of (a) 0.5CHS-0.5WSiA (dry mill)/PBI and (b) 0.5CHS-0.5WSiA(wet mill)/PBI composite membranes.

Photographs of 0.5CHS-0.5WSiA(dry mill) and 0.5CHS-0.5WSiA(wet mill) composite electrolyte membranes are shown in Fig. 5. They both were seen to be good transparent and homogenous appearances. FE-SEM morphologies of cross-sectional measurements of the composite membranes were shown in Fig. 6 with the typical thickness of 50-70 μm for the composite membranes; and they showed inorganic composite materials were thoroughly dispersed in PBI matrix after fabrication of CHS-WSiA/PBI composite membranes. These observations suggested that the homogeneous and thin membranes with sufficient thickness were convenient to apply for anhydrous conductivity measurements and FC performance evaluation.

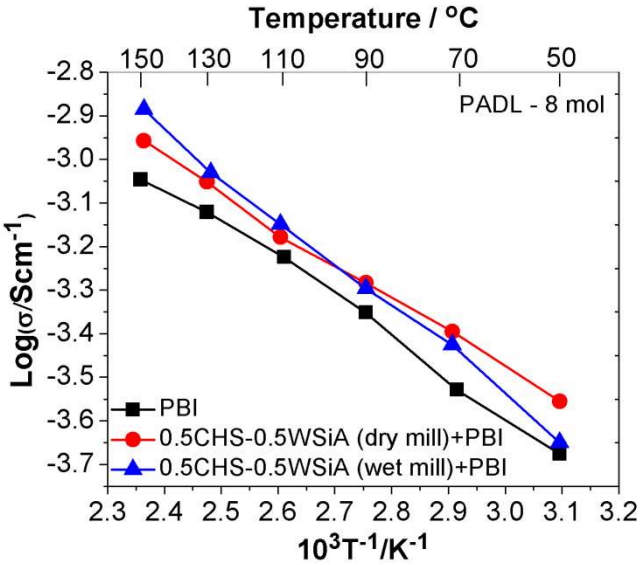

Fig. 7. Temperature dependence of conductivity of pristine PBI membrane, 0.5CHS-0.5WSiA (dry mill)/PBI and 0.5CHS-0.5WSiA(wet mill) /PBI composite membranes under anhydrous condition.

Anhydrous proton conductivities of pristine PBI and CHS-WSiA/PBI composite electrolyte membranes were measured along the temperature range 50-150 ^{o}C. Figure 7 shows the temperature-dependent conductivity measurements of pristine PBI and composite PBI membranes with 8 mol of PADL. The conductivity's trends of all membranes were increasing with increasing the temperature in the range 50 to 150 ^{o}C. However, the conductivity values of the CHS-WSiA/PBI membranes were observed that they showed higher than that of the pristine PBI. The proton conductivities of pristine PBI was ranged from 2.11×10^{-4} to 8.99×10^{-4} S cm^{-1} and the proton conductivities of CHS-WSiA (dry)/PBI and CHS-WSiA(wet)/PBI showed from 2.79×10^{-4} to 1.104×10^{-3} S cm^{-1} and 1.78×10^{-4} to 1.302×10^{-3} S cm^{-1} respectively. Especially, CHS-WSiA(wet)/PBI membrane showed high conductivity above 110 ^{o}C that compared with CHS-WSiA(dry)/PBI membrane and pristine PBI. These observations suggested that CHS-WSiA composite membranes with nano-scale composites maintain acid and water retention properties comparing with pristine PBI membrane for enhancing the proton conductivity after adsorbing PA.

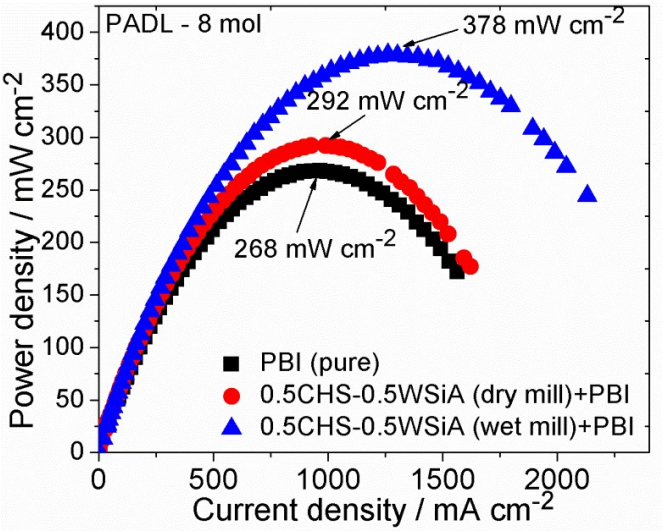

Fig. 8. Power density curves of pristine PBI membrane, 0.5CHS-0.5WSiA (dry mill) /PBI and 0.5CHS-0.5WSiA(wet mill) /PBI composite membranes under anhydrous condition.

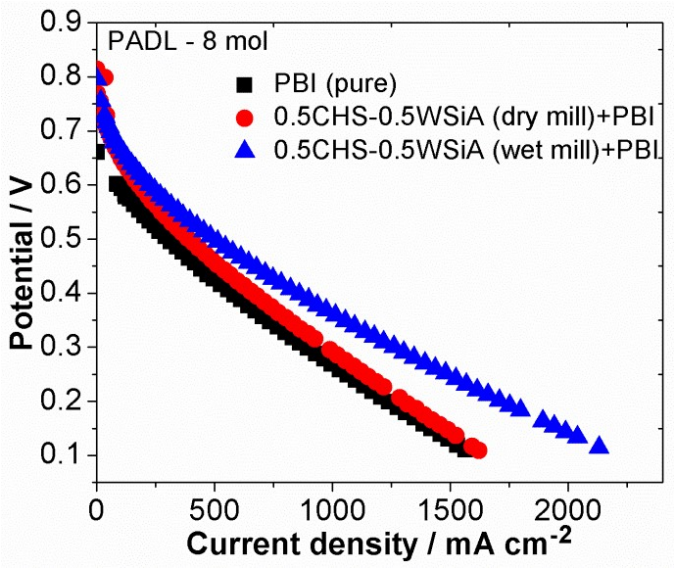

Fig. 9. Polarization curve of pristine PBI membrane, 0.5CHS-0.5WSiA (dry mill) /PBI and 0.5CHS-0.5WSiA(wet mill) /PBI composite membranes under anhydrous condition.

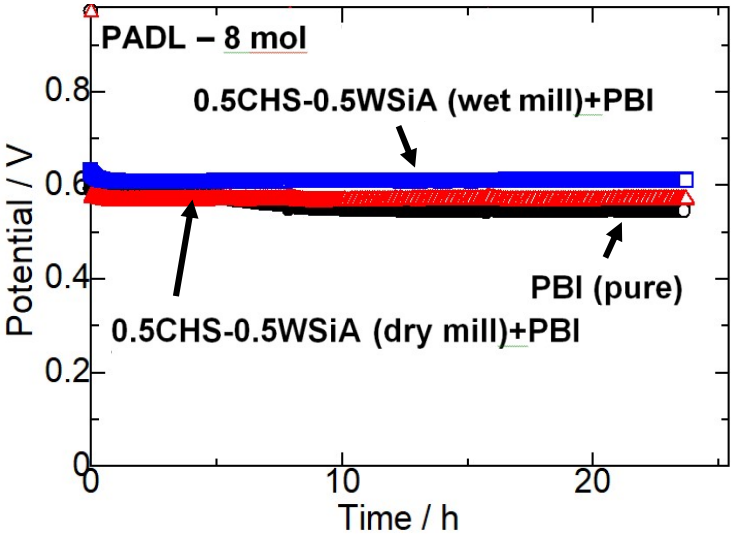

Fig. 10. Constant current density measurement of pristine PBI membrane, 0.5CHS-0.5WSiA (dry mill)/PBI and 0.5CHS-0.5WSiA(wet mill) /PBI composite membranes under anhydrous condition.

The fuel cell evaluation of electrolyte membranes was performed according to their results (shown in Fig. 8 and Fig. 9) ; with highest power density values of 268, 292, and 378 mW cm^{-2} for pristine PBI, CHS-WSiA(dry)/PBI, and CHS-WSiA(wet)/PBI, respectively. While CHS-WSiA/PBI membranes showed the open circuit voltages (> 0.8 V) for low gas permeability, pristine PBI showed the open circuit voltage less than 0.8 V. To make the comparison between CHS-WSiA/PBI membranes and pristine PBI in Fig. 8 and 9, it can be seen that all the CHS-WSiA/PBI membrane fuel cells showed good performance compared with pristine PBI. Thus, the CHS-WSiA components in the PBI matrix emphatically adsorbed and retained the PA acid groups in their CHS-WSiA/PBI composite membranes to enhance proton conduction mechanism and prevent acid leaching problem.

The current stability tests of 20 wt % of CHS-WSiA/PBI composite membranes and pristine PBI were measured to make confirmation of the acid retention properties and thermal stability of the CHS-WSiA composites/PBI matrix (shown in Fig. 10). The stability tests of composite membranes and pristine PBI were performed as fixed current measurements (0.2 A/cm^{-2}, 24 h). While 20 wt % CHS-WSiA/PBI composite membranes showed constant potential condition throughout the constant current measurement (0.2 A cm^{-2}), the pristine one was observed for the degradation of potential after 8 h measurement. These observation of cell performances suggested that inorganic composites partly supported to the PA acid retention of the adsorbed PA ligands via to new proton conduction of CHS-WSiA composites/PBI matrix.

Thus, the grain nanostructures of the CHS-WSiA composites with grain nano-sized particles by wet milling in the PBI matrix supported to be homogeneously dispersed in the membrane matrix and also created new proton conduction path after adsorption of PA [26].

4 Conclusions

CHS-WSiA composites were successfully fabricated via dry and wet mechanical milling, and characterized using XRD, FE-SEM, and proton conductivity measurements. The

diffraction peaks of these composites shifted to a higher angle via an ion-exchange reaction from a mechanochemical efffect. The grain sizes (about 20 nm) of CHS-WSiA composite obtained by wet milling are smaller than the composite obtained by dry milling. From conductivity measurement, CHS-WSiA composite (wet milling) showed higher conductivity of about 10^{-3} S cm^{-1}, compared to the raw substances at low temperatures. Inorganic-organic CHS-WSiA/PBI membranes were observed for enhanced adsorption and retention properties of PA in the medium temperature (100-200 ^{o}C) fuel cell evaluation via new proton conduction path of CHS-WSiA composites. CHS-WSiA/PBI membranes showed higher performances with 378 mW cm^{-2} for CHS-WSiA(wet)/PBI and 292 mW cm^{-2} for CHS-WSiA(dry)/PBI in comparing with 268 mW cm^{-2} of pristine PBI membrane. For constant current test, CHS-WSiA/PBI composite membranes showed stable potential over 24 h period while the potential of pristine PBI was decreased after 8 h. Among membranes, CHS-WSiA(wet)/PBI showed fast PA doping compared with CHS-WSiA(dry)/PBI and pristine PBI. Addition of inorganic solid acid complex with high proton conductivity caused fast proton transfer in these composites/PBI electrolyte membranes. Both CHS-WSiA/PBI electrolyte membranes showed proton conductivities higher than pristine PBI. A new proton conduction path was also proposed in these composite membranes due to the inorganic solid composites's effect in the PBI matrix. CHS-WSiA(wet)/PBI showed the highest power density and best durability test with high potential stability among these electrolyte membranes because it showed a stable performance even in a second cycle fuel cell performance measurement by suppressing of PA leaching.

Acknowledgements

This research work was done by the supports from JSPS Grants-in-Aid for Scientific Research A (26249097), JSPS Grants-in-Aid for Scientific Research A (18H03841), and AUN/SEED-Net (JICA).

References

1. N. Abdullah, S.K. Kamarudin, J. Power Sources. **278,** 109-118 (2015).
2. M. Mizuno, S. Hayashi, Solid State Ionics, **167,** 317-323 (2004).
3. O. Barron, H. Su, V. Linkov, B. G. Pollet, S. Pasupathi, J App Electrochem. **44,** 1037-1045 (2014).
4. Q. Li, R. He, J. O. Jensen, N. J. Bjerrum, Fuel cells. **4**, 147-159 (2004).
5. J. Loboto, P. Cañizares. M.A. Rodrigo, J.J. Linares, J. A. Aguilar, J. Membr. Sci. **306,** 47-55 (2007).
6. A. Matsuda, T. Kanzaki, K. Tadanaga, M. Tatsumisago, T. Minami, Electrochim. Acta. **47**, 939-944 (2001).
7. A. Matsuda, T. Kanzaki, K. Tadanaga, M. Tatsumisago, T. Minami, Solid State Ionics. **139**, 113-119 (2001).
8. N. Nakamoto, A. Matsuda, K. Tadanaga, T. Minami, M. Tatsumisago, J. Power Sources. **138,** 51-55 (2004).
9. K. Tadanaga, H. Yoshida, A. Matsuda, T. Minami, M. Tatsumisago, Electrochim. Acta. **50,** 705-708 (2004).
10. Y. Oono, T. Fukuda, A. Sounai, M. Hori, J. Power Sources. **195,** 1007-1014 (2010).
11. J. Lablo, P. Cañizares, M. A. Rodrigo, D. Úbeda, F. Javier Pinar. J. Membr. Sci. **369,** 105-111 (2011).

12. F. J. Pinar, P. Cañizares, M. A. Rodrigo, D. Ubeda and J. Lobato, RSC Advances. **2,** 1547-1556 (2012).
13. S. Yuk, D-H. Lee, S. Choi, G. Doo, D. W. Lee, H-Tak. Kim, Electrochim Acta. **270**, 402-408 (2018).
14. J. Halter, S. Thomas, S. K. Kær, T. J. Schmidt, F. N. Büchi. J. Power Sources. **399**, 151-156 (2018).
15. D. Ergun, Y. Devrim, N. Bac, I. Eroglu. J. Applied Polymer Science. **124,** E267-E277 (2012).
16. S-Y. Oh, T. Yoshida, G. Kawamura, H. Muto, M. Sakai, A. Matsuda, J. Mat. Chem. **20,** 6359-6366 (2010).
17. Y. Daiko, H. Takagi, K. Katagiri, H. Muto, M. Sakai, A. Matsuda, Solid State Ionics. **179,** 1174-1177 (2008).
18. S. Shanmugam, B. Viswanathan, T.K. Varadarajan, J. Membr. Sci, **275,** 105-109 (2006).
19. S.Y. Oh, T. Yoshida, G. Kawamura, H. Muto, M. Sakai, A. Matsuda, J. Power Sources. **195,** 5822-5828 (2010).
20. A. Matsuda, V.H. Nguyen, Y. Daiko, H. Muto, M. Sakai, Solid State Ionics. **181,** 180-182 (2010).
21. E. Y. Safronova, A.K. Osipov, A. E. Baranchikov, A.B. Yaroslavtsev. Inorg. Mat. **51**, 1157-1162 (2015).
22. Suryani, Y-L. Liu, J. Membr. Sci. **332,** 121-128 (2009).
23. A. Matsuda, S-Y. Oh, V.H. Nguyen, Y. Daiko, G. Kawamura, H. Muto. Electrochim. Acta. **56,** 9364-9369 (2011).
24. J. Mbah, B. Krakow, E. Stefanakos, J. Wolan, Electrochem. and Solid-State Letters. **12,** E12-E16 (2009).
25. C. Xu, X. Wu, X. Wang, M. Mamlouk, K. Scott, J. Mater. Chem. **21,** 6014-6019 (2011).
26. K. Z. Ya, K. Kumazawa, G. Kawamura, H. Muto, A. Matsuda, J. Ceram. Soc. Jpn. **126,** 789-793 (2018).

A Type of Hysteretic Nonlinear Model of Piezoelectric Sensor

Qing-xin Zhang [1] , *Zhi-wen* Zhu [2] , and *Xin-miao* Li [1,*]

[1]Beijing institute of structure and environment engineering, 1 Nan Da Hong Men Road, Beijing 100076, P.R.China

[2]Tianjin key laboratory of nonlinear dynamics and control, 92 Weijin Road, Tianjin 300072, P.R.China

Abstract. In this paper, a type of hysteretic constitutive model of piezoelectric sensor was proposed. Nonlinear differential terms were developed to express the hysteresis phenomena of displacement-voltage relationship of piezoelectric ceramics. Based on the model, the dynamic model of a PZT sensor was established. The nonlinear dynamic behaviours of a PZT sensor were analyzed, and the relationship between the outside excitation and the voltage of a PZT sensor was obtained. Theoretical results show that there are many kinds of frequencies in the output voltage, which are caused by the PZT's hysteresis characteristics.

1 Introduction

Piezoelectric ceramics is a kind of smart material, which has high control accuracy and high response speed [1]. Piezoelectric sensors are widely used in engineering. The piezoelectric ceramics used widely is PZT. Usually, piezoelectric sensor is regarded as linear [2]. In fact, all kinds of piezoelectric ceramics have the hysteretic characteristics more or less [3]. To obtain the accurate response of piezoelectric sensor, an accurate physical model of piezoelectric ceramics is necessary.

Due to PZT's hysteretic characteristics, many PZT's constitutive model is equations with piecewise functions [4]. Indeed, equations with piecewise functions can express the hysteresis. However, the dynamic model of PZT structures is usually the differential equations, and the modern mathematics methods can't deal with the differential equations with piecewise functions [5]. It means that the common PZT's constitutive model can't be analysed by theory. In this paper, nonlinear differential terms were developed to describe the hysteresis phenomena of PZT's displacement-voltage curves. The physical model of a PZT sensor was established, and its nonlinear dynamic characteristics were analysed. Finally, the relationship between the outside excitation and the output voltage of PZT sensor was obtained.

2 PZT Model

* Corresponding author: lxmtju@163.com

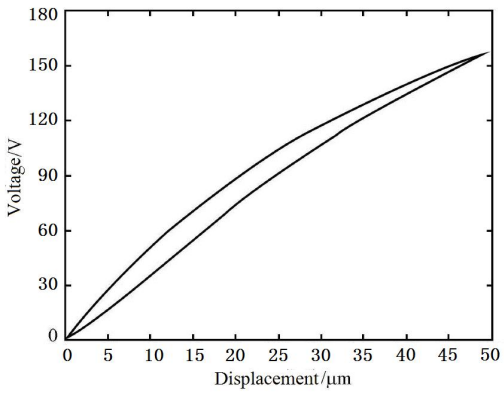

Fig. 1. PZT's displacement-voltage curves

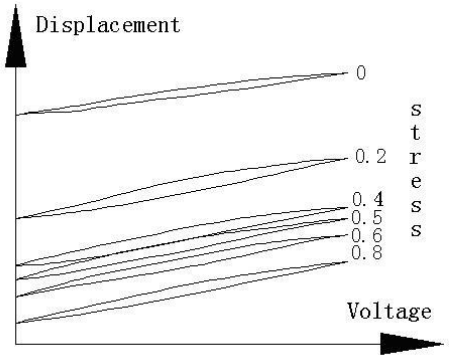

Fig. 2. Voltage-displacement curves with pre-stress

The PZT's displacement-voltage curves were in Fig.1. The relationship between strain and voltage can be shown as follows:

$$U = \phi\varepsilon + \chi\varepsilon^2 + \alpha\varepsilon^3 + \beta(\rho\varepsilon - \varepsilon^2)\dot{\varepsilon} \tag{1}$$

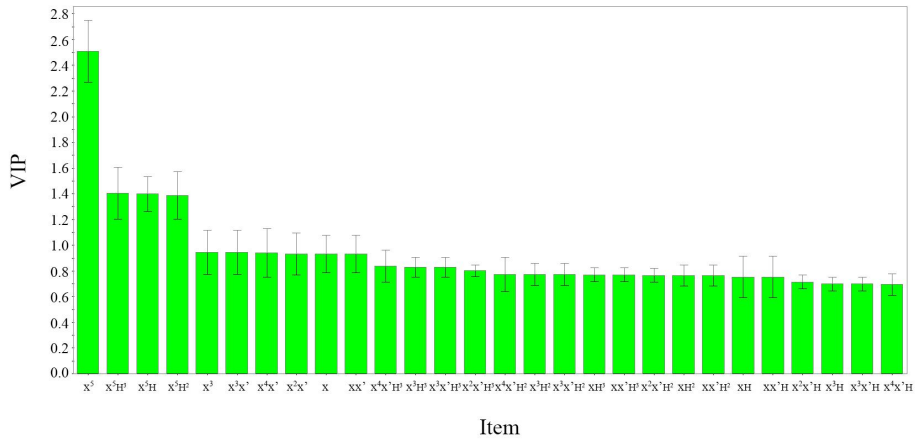

Fig. 3. Results of principal component analysis

In fact, piezoelectric layer was pre-tightened in the piezoelectric sensor, and the stress σ will influence the PZT's strain, which is shown in Fig.2. The results of principal component analysis were in Fig.3, and the VIP values of every term were in Tab.1. Thus, the reduced constitutive model is:

$$U = a_0 + a_1\varepsilon + a_2\varepsilon\dot{\varepsilon} + a_3\varepsilon^2\dot{\varepsilon} = a_1\varepsilon + a_2\varepsilon\dot{\varepsilon} + a_3\varepsilon^2\dot{\varepsilon} + a_4\sigma + a_5\sigma^2 + a_6\sigma^3 \tag{2}$$

where a_i are the coefficients of terms and can be obtained in fitting method, $a_0 = a_4\sigma + a_5\sigma^2 + a_6\sigma^3$ was constant term which was caused by pre-stress σ. Especially, a_1 is the linear coefficient of strain ε, which can be shown in other physical parameters.

Table 1. VIP of each term

Term	VIP	Term	VIP
ε	1.20443	$\varepsilon^2 \cdot \dot{\varepsilon} \cdot \sigma$	0.655907
ε^2	0.844829	$\varepsilon \cdot \sigma^2$	0.765879
ε^3	0.993686	$\varepsilon^2 \cdot \sigma^2$	0.655907
$\varepsilon \cdot \dot{\varepsilon}$	1.20443	$\varepsilon^3 \cdot \sigma^2$	0.971131
$\varepsilon^2 \cdot \dot{\varepsilon}$	1.04483	$\varepsilon \cdot \dot{\varepsilon} \cdot \sigma^2$	0.765879
σ	2.08006	$\varepsilon^2 \cdot \dot{\varepsilon} \cdot \sigma^2$	0.655907
σ^2	1.22828	$\varepsilon \cdot \sigma^3$	0.948518
σ^3	1.30299	$\varepsilon^2 \cdot \sigma^3$	0.848281
$\varepsilon \cdot \sigma$	0.846878	$\varepsilon^3 \cdot \sigma^3$	0.819562
$\varepsilon^2 \cdot \sigma$	0.423017	$\varepsilon \cdot \dot{\varepsilon} \cdot \sigma^3$	0.948518
$\varepsilon^3 \cdot \sigma$	0.809895	$\varepsilon^2 \cdot \dot{\varepsilon} \cdot \sigma^3$	0.848281
$\varepsilon \cdot \dot{\varepsilon} \cdot \sigma$	0.846878		

The charge of piezoelectric patch Q is

$$Q = \iint D_3 dydz = D_3 A \tag{4}$$

where D_3 is the electric displacement, A is the area of piezoelectric patch.

Considering that $D_3 = d_{33} T_3$, $T_3 = \frac{k_2 x_2}{A}$, $x_2 = h\varepsilon$, we obtained:

$$Q = d_{33} T_3 A = d_{33} k_2 x_2 = d_{33} k_2 h\varepsilon \tag{5}$$

where d_{33} is the piezoelectric strain constant, T_3 is the stress in X direction, h is the thickness of piezoelectric patch.

Thus,

$$U = \frac{Q}{C} = \frac{d_{33} k_2 h\varepsilon}{C} = \frac{d_{33} k_2 h\varepsilon}{\frac{\varepsilon_0 \varepsilon_r A}{h}} = \frac{d_{33} h^2 k_2}{\varepsilon_0 \varepsilon_r A} \varepsilon = a_1 \varepsilon \tag{6}$$

where U is the voltage, C is the capacitor, $C = \frac{\varepsilon_0 \varepsilon_r A}{h}$, ε_0 is the vacuum permittivity, ε_r is the relative dielectric constant of PZT.

From Eq.6, we obtained

$$a_1 = \frac{d_{33} h^2 k_2}{\varepsilon_0 \varepsilon_r A} \tag{7}$$

Eq.7 can be used to examine the accuracy of fitting result. From Figs.4 and 5, we can see that the constitutive model has good accuracy.

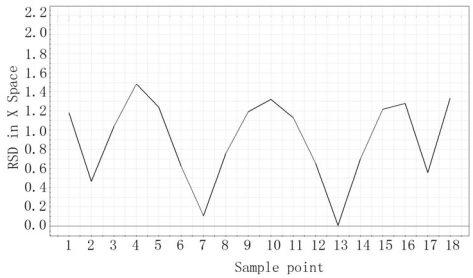

Fig. 4. Results of DModX

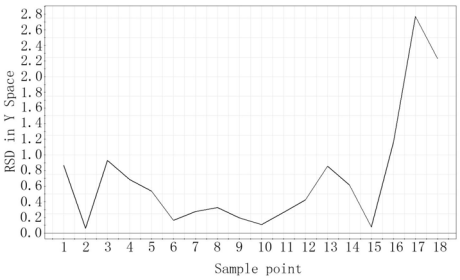

Fig. 5. Results of DModY

3 Modeling of Piezoelectric Sensor

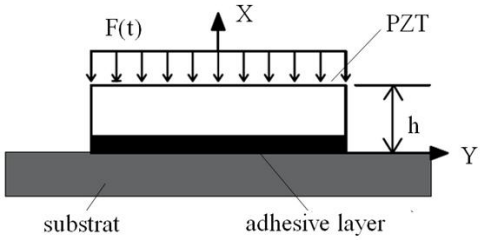

Fig. 6. Structure of piezoelectric sensor

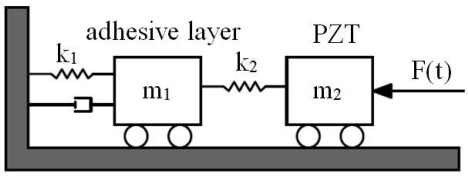

Fig. 7. Physical model of piezoelectric sensor

The structure of a piezoelectric sensor was shown in Fig.6, where PZT was glued with the substrate. The model of a piezoelectric sensor was in Fig.7, where m_1 is mass of adhesive layer, m_2 is mass of PZT, k_1 is equivalent connection stiffness of adhesive layer, k_2 is stiffness of PZT, c_1 is damping of adhesive layer, $F(t)$ is outside perturb. The mathematic model of piezoelectric sensor is:

$$\begin{bmatrix} m_1 & 0 \\ 0 & m_2 \end{bmatrix}\begin{pmatrix} \ddot{x}_1 \\ \ddot{x}_2 \end{pmatrix}+\begin{bmatrix} c_1 & 0 \\ 0 & 0 \end{bmatrix}\begin{pmatrix} \dot{x}_1 \\ \dot{x}_2 \end{pmatrix}+\begin{bmatrix} k_1+k_2 & -k_2 \\ -k_2 & k_2 \end{bmatrix}\begin{pmatrix} x_1 \\ x_2 \end{pmatrix}=\begin{pmatrix} 0 \\ F(t) \end{pmatrix} \tag{8}$$

where x_1 is the deformation of adhesive layer, and x_2 is the deformation of PZT. To harmonic exciation,

$$x_2 = h\varepsilon = \frac{\sqrt{[k_2(m_1+m_2)-\omega^2 m_1 m_2]^2+\omega^2 c_1^2(m_1+m_2)^2}}{\sqrt{a^2+b^2}}\overline{F}\cos\omega t \tag{9}$$

where x_2 is displacement of piezoelectric patch in X direction,

$$a = \omega^4 m_1 m_2 - \omega^2(2k_2 m_1 + k_1 m_2 + k_2 m_2) + 2k_2(k_1+k_2)$$

$$b = \omega^2 c_1(m_1+m_2) + \omega c_1(3k_2 - k_1)$$

Let

$$n_1 = \frac{\sqrt{[k_2(m_1+m_2)-\omega^2 m_1 m_2]^2+\omega^2 c_1^2(m_1+m_2)^2}}{\sqrt{a^2+b^2}}$$

Thus,

$$\begin{aligned} U &= a_0 + a_1\varepsilon + a_2\varepsilon\dot{\varepsilon} + a_3\varepsilon^2\dot{\varepsilon} \\ &= a_0 + \frac{a_1 n_1}{h}\overline{F}\cos\omega t + \frac{a_3 n_1^3\omega}{4h^3}\overline{F}^3\sin\omega t - \frac{a_2 n_1^2\omega}{2h^2}\overline{F}^2\sin 2\omega t + \frac{a_3 n_1^3\omega}{4h^3}\overline{F}^3\sin 3\omega t \\ &= a_0 + U_0 + U_1 \end{aligned} \tag{10}$$

where

$$U_0 = \frac{a_1 n_1}{h}\overline{F}\cos\omega t \quad ,$$

$$U_1 = \frac{a_3 n_1^3\omega}{4h^3}\overline{F}^3\sin\omega t - \frac{a_2 n_1^2\omega}{2h^2}\overline{F}^2\sin 2\omega t + \frac{a_3 n_1^3\omega}{4h^3}\overline{F}^3\sin 3\omega t \, .$$

Eq.10 can be used in design of piezoelectric sensor:

1) $a_0 = a_4\sigma + a_5\sigma^2 + a_6\sigma^3$ was the constant term which was caused by stress σ;
2) $U_0 = \frac{a_1 n_1}{h}F = \frac{a_1 n_1}{h}\overline{F}\cos\omega t$. It means that U_0 is linear with F;
3) U_1 was the error, which should be eliminated. In engineering, this term can be reduced by adjusting the parameters or active control.

5 Conclusion

In this paper, a type of hysteretic constitutive model of piezoelectric sensor was proposed. Nonlinear differential terms were developed to express the hysteresis phenomena of displacement-voltage relationship of piezoelectric ceramics. Based on the model, the dynamic model of a PZT sensor was established. The nonlinear dynamic behaviours of a PZT sensor were analysed, and the relationship between the outside excitation and the voltage of a PZT sensor was obtained. We can see that there are many kinds of frequencies in the output voltage, which are caused by the PZT's hysteresis characteristics.

Acknowledgements

The authors thank the support of Tianjin RPAFAT through Grant No. 16JCYBJC18800, and Cast-Bisee 511 Program through Grant No. CAST-BISEE2017-006.

References

[1] N.W. Hagood, W.H. Chung and A.V. Journal of Intelligent Material Systems and Structures **1** (1990).

[2] P.Ge, M. Precision Engineering **20** (1997).

[3] M.H. Shen. Computers and Structures **57** (1995).

[4] L.N. Sun, C.H. Ru and W.B. Rong. Journal of Micromechanics and Microengineering **14** (2004).

[5] M. Deshpande, L. Saggere. Sensors and Actuators A-Physical **136** (2007).

[6] C.H. Ru, L.G. Chen and B. Shao. Control Engineering Practice **17** (2009).

Nonlinear dynamic characteristics of SMA gripper under bounded noise

Xin-miao Li [1] , *Zhi-wen* Zhu [2] , and *Qing-xin* Zhang [1,*]

[1]Beijing institute of structure and environment engineering, 1 Nan Da Hong Men Road, Beijing 100076, P.R.China

[2]Tianjin key laboratory of nonlinear dynamics and control, 92 Weijin Road, Tianjin 300072, P.R.China

Abstract. A kind of constitutive model of SMA is proposed in this paper, and the nonlinear dynamic response of a SMA gripper under bounded noise is studied. The harmonic driving signals and the random disturbance made up of bounded noise. The dynamic model of the system is established by Hamilton principle. The numerical and experimental results show that there is stochastic resonance in the system; the system's vibration amplitude reaches the most when the outside excitation is moderate.

1 Introduction

Shape memory alloy (SMA) is a type of smart material, which has shape memory effect. SMA gripper is used in medical field widely [1]. To enhance the accuracy of SMA gripper, its dynamic characteristics should be studied. Many researchers have studied SMA gripper [1–7]. Kohl et al. studied a SMA gripper's dynamic response and control [2]. Just et al. applied position control to a SMA gripper and obtained high control accuracy [3]. To SMA materials, Graesser et al. proposed a three-dimensional SMA constitutive model [4]. Ivshin et al. developed a SMA thermo-mechanical model [5]. Although many achievements have been reported, most of them focused on the constitutive model, and the results of dynamic response of SMA gripper are absent.

SMA gripper used in medicine are controlled by harmonic currents to achieve the opening and closing action. However, SMA gripper are usually under stochastic excitation in the working process. Although the stochastic excitation is weak, it will affect the gripper's motion. The harmonic control force and the stochastic excitation generate a bounded noise, which cause the different dynamic characteristics from the harmonic system.

* Corresponding author: zhqx@spacechina.com

2 SMA constitutive model

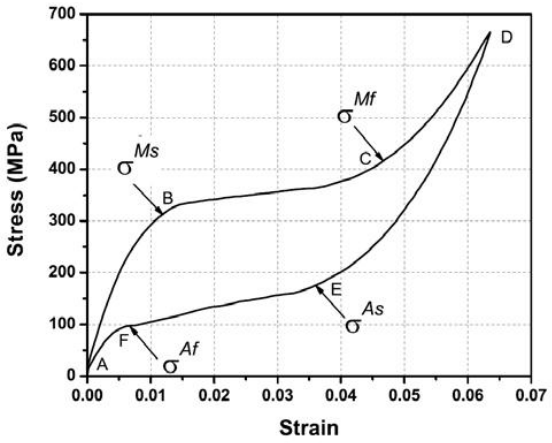

Fig. 1. Strain-stress curves of the SMA.

The experimental results of SMA are shown in Figure 1. The length of Ti-Ni SMA film is 7mm, the width is 1.5mm, and the thickness is 0.1mm. The SMA's austenite finish temperature is 34℃. Thus, the hysteretic phenomenon is induced by the superelastic behavior of SMA. Zhu et al. established a SMA's constitutive model as follows [8]:

$$\sigma = \sigma_1 + \sigma_2 = a_1\varepsilon + a_2\varepsilon^2 + a_3\varepsilon^3 + (a_4\varepsilon + a_5\varepsilon^2 + a_6\varepsilon^3 + a_7\varepsilon^4)\dot{\varepsilon} \quad (1)$$

where σ is the stress, ε is the strain. To SMA shown in Figure 1, a_1 =10000, a_2 =-32, a_3 =5.7.

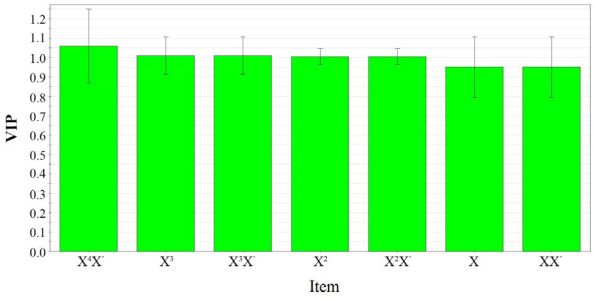

Fig. 2. Variable importance of each term.

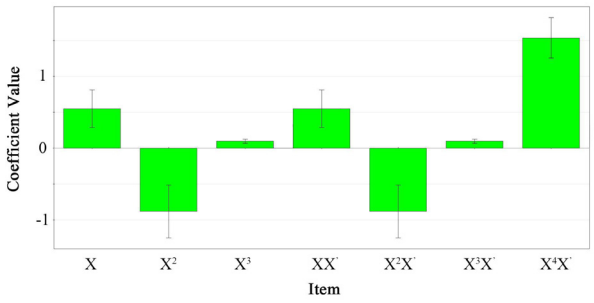

Fig. 3. Coefficient values of each term.

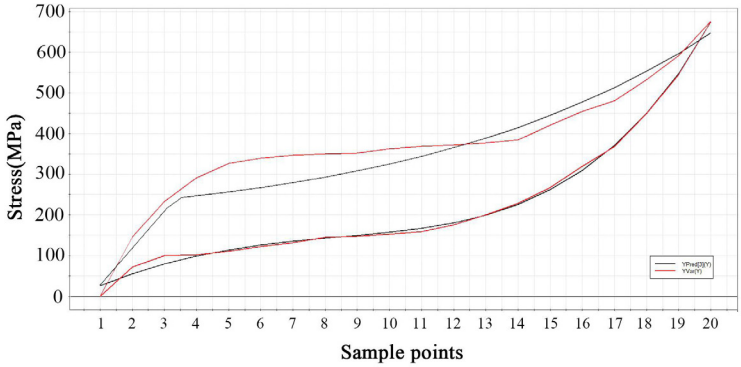

Fig. 4. Results of forecast test for the fitting effect of Eq. (1) on strain-stress data of SMA.

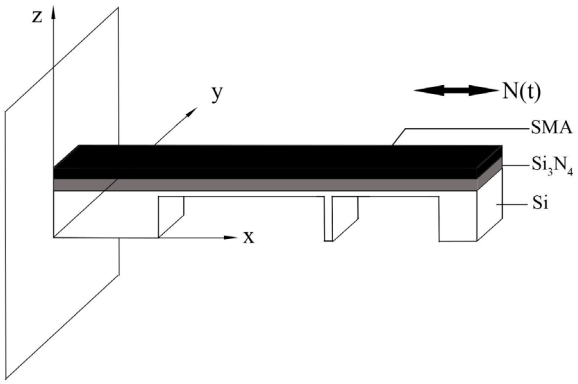

Fig. 5. Results of forecast test for the fitting effect of Eq. (1) on strain-stress data of SMA.

The results of prediction test to Eq. (1) are shown in Figure 4, and the mechanical model of a SMA gripper under bounded noise is shown in Figure 5, where $N(t) = F\sin(\Omega t + \chi + \sigma B(t))$ is the bounded noise. The Hamilton's variational principle is:

$$\delta S = \int_{t_1}^{t_2} \delta(T_1 + T_2 - U_1 - U_2 + W_d + W)dt = 0 \tag{3}$$

where $T_1 = \frac{1}{2}\int_0^L \rho_1 A_1 (\frac{\partial u}{\partial t})^2 dx$, $T_2 = \frac{1}{2}\int_0^L \rho_2 A_2 (\frac{\partial u}{\partial t})^2 dx$,

$U_1 = \int_0^L \frac{E_1 I_2}{2}(\frac{\partial^2 u}{\partial x^2})^2 dx + \frac{E_1 A_1}{8L}[\int_0^L (\frac{\partial u}{\partial x})^2 dx]^2$, $U_2 = \frac{1}{2}E_2 A_2 \int_0^L (\frac{\partial u}{\partial x})^2 dx$,

$W_d = -\int_0^L cu\frac{\partial u}{\partial t}dx$, $W = \int_0^L \delta u N dx$.

Thus, the dynamic model of a SMA gripper is:

$$m\frac{\partial^2 u}{\partial t^2}+[c+\int_0^L E_1A_1(a_4u+a_5u^2+a_6u^3+a_7u^4)dx]\frac{\partial u}{\partial t}+b_1\frac{\partial^2 u}{\partial x^2}$$
$$+b_2\frac{\partial^4 u}{\partial x^4}-b_3\frac{\partial^2 u}{\partial x^2}\int_0^L(\frac{\partial u}{\partial x})^2dx=N+\frac{1}{2}(E_2A_2\frac{\partial^2 u}{\partial x^2}+\rho_2A_2\frac{\partial^2 u}{\partial t^2}) \quad (4)$$

where $m=\frac{\rho_1A_1l}{L}+\rho_2A_2$, $b_1=\frac{a_1E_2A_2}{3}+\frac{\varepsilon_{33}^sE_3A_1}{2}$, $b_2=a_2E_2I_2$, $b_3=\frac{E_1A_1}{8L}$.

The equation of the system's response are:

$$\begin{cases}\ddot{u}_1+b_1u_1+b_2u_1^3+\gamma u_1u_2^2+(2\eta+b_3u_1^2+b_4u_1^4)\dot{u}_1=e\sin(\Omega t+\theta+\sigma B(t))\\ \ddot{u}_2+c_1u_1+c_2u_1^3+\gamma u_1u_2^2+(2\eta+c_3u_1^2+c_4u_1^4)\dot{u}_1=g\sin(\Omega t+\theta+\sigma B(t))\end{cases} \quad (5)$$

where η is the damping coefficient, $b_1=\frac{a_1\pi^2(\frac{9}{a^2}+\frac{1}{b^2})^2-\frac{\pi^2}{b^2}N_0}{\rho h}$, $c_1=\frac{a_1\pi^2(\frac{1}{a^2}+\frac{9}{b^2})^2-\frac{\pi^2}{a^2}N_0}{\rho h}$, $b_2=\frac{a_3\pi^4}{4\rho hab}(\frac{27a}{b^3}+\frac{b}{a^3})$, $c_2=\frac{a_3\pi^4}{4\rho hab}(\frac{a}{b^3}+\frac{27b}{a^3})$, $b_3=\frac{a_5\pi^6}{16\rho hab}(\frac{81a}{b^4}+\frac{b}{a^4})$, $c_3=\frac{a_5\pi^6}{16\rho hab}(\frac{a}{b^4}+\frac{81b}{a^4})$, $b_4=\frac{a_7\pi^8}{64\rho hab}(\frac{243a}{b^4}+\frac{b}{a^4})$, $c_4=\frac{a_7\pi^8}{64\rho hab}(\frac{a}{b^4}+\frac{243b}{a^4})$, $e=\frac{F\pi^2(\frac{9}{a^2}+\frac{1}{b^2})^2}{\rho h}$, $g=\frac{F\pi^2(\frac{1}{a^2}+\frac{9}{b^2})^2}{\rho h}$; γ is the coupling coefficient.

Let $u_1=q$, the first equation of Eqs.5 can be shown as follows:

$$\ddot{q}+b_1q+b_2q^3+(2\eta+b_3q^2+b_4q^4)\dot{q}=e\sin(\Omega t+\theta+\sigma B(t)) \quad (6)$$

3 Nonlinear dynamic characteristics of a SMA gripper

When the noise intensity $\sigma=0$, the outside excitation becomes harmonic excitation, and the dynamic model can be shown as follows:

$$\ddot{q}+b_1q+b_2q^3+(2\eta+b_3q^2+b_4q^4)\dot{q}=e\sin(\Omega t+\theta) \quad (7)$$

The solution of Eq. (7) is:

$$q=q_0\cos(\omega t+\theta)+q_1\cos(\omega t+\theta)+q_2\cos 3(\omega t+\theta)+$$
$$q_3\sin(\omega t+\theta)+q_4\sin 3(\omega t+\theta)+q_5\cos 5(\omega t+\theta) \quad (8)$$

where, $q_0=\frac{e}{\overline{\omega}}b_1$, $q_1=\frac{3e^3}{4\overline{\omega}}b_2$, $q_2=-\frac{e^3}{4\overline{\omega}}b_2$, $q_3=\frac{3e^3}{4\overline{\omega}}b_3\omega$, $q_4=\frac{e^3}{4\overline{\omega}}b_3\omega$, $q_5=\frac{e^5}{16\overline{\omega}}b_4\omega$, $\omega=\sqrt{b_1}$, $\overline{\omega}=\sqrt{(\Omega^2-\omega^2)^2+(2\eta\omega)^2}$.

When the noise intensity $\sigma\neq 0$, the outside excitation becomes bounded noise, and Eq. (6) becomes a stochastic nonlinear differential equation. The averaged Ito equation of Eq. (6) are:

$$\begin{cases} dA = m_1(A,\Delta')dt \\ d\Delta' = m_2(A,\Delta')dt + \sigma dB(t) \end{cases} \tag{9}$$

where

$$\Delta' = \Omega t + \sigma B(t) + \chi - \Theta$$

$$m_1(A,\Delta') = -\pi(b_3 A^2 + \frac{1}{4} b_4 A^4) - \frac{eA}{2\eta}\cos\Delta'$$

$$m_2(A,\Delta') = 2\pi\Omega - \frac{1}{\eta}(\frac{3}{4}\pi b_2 A^3 - \frac{e}{2}\sin\Delta')$$

The system's averaged equation is:

$$\frac{\partial f}{\partial t} = -\frac{\partial}{\partial A}(m_1 f) - \frac{\partial}{\partial \Delta'}(m_2 f) + \frac{\sigma^2}{2}\frac{\partial^2 f}{\partial \Delta'^2} \tag{10}$$

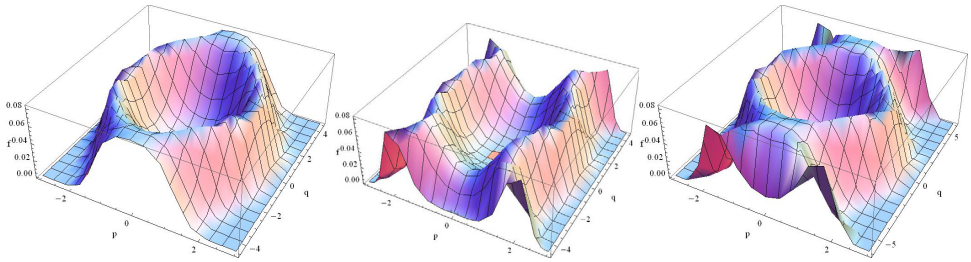

(a) $\sigma = 0.1$ (b) $\sigma = 0.5$ (c) $\sigma = 0.8$

Fig. 6. Stationary probability density of the system's response.

The numerical results of the system's response are presented in Figure 6, and the experimental results of SMA gripper under bounded noise are shown in Figures 7-9, where the frequency Ω =30Hz. Ti–Ni alloy is chosen as SMA film. The length of the micro gripper is 10cm, and its width is 1cm. The length of SMA thin film is 3cm, its width is 1cm, and its thickness is 0.4 mm. The stochastic resonance phenomenon occurs in the process.

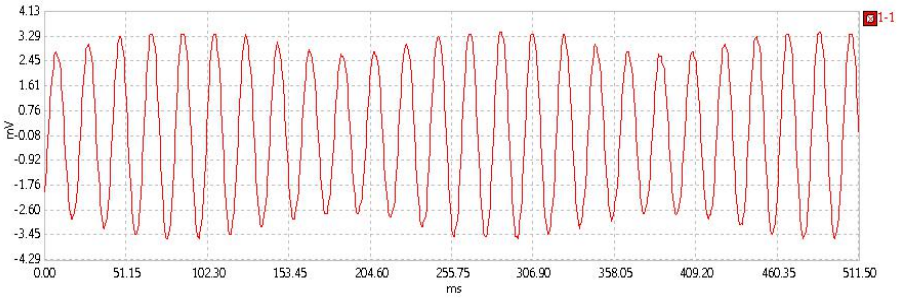

Fig. 7. Response of SMA gripper when $\sigma = 0.1$.

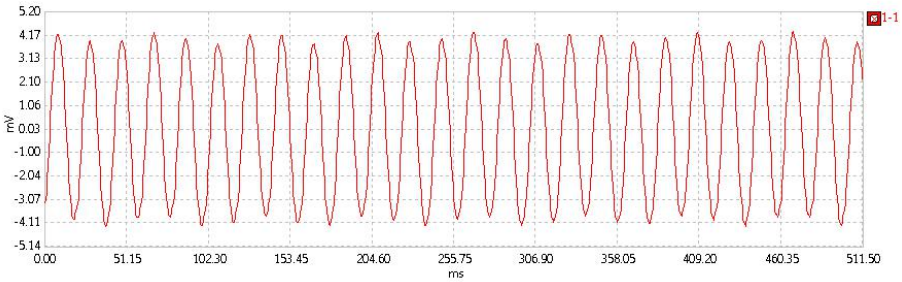

Fig. 7. Response of SMA gripper when $\sigma = 0.5$.

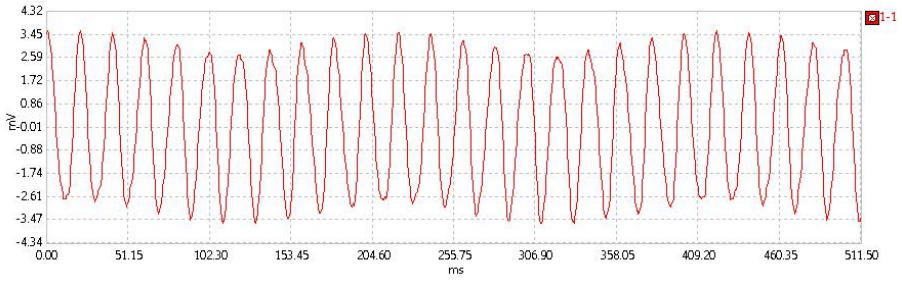

Fig. 7. Response of SMA gripper when $\sigma = 0.8$.

4 Conclusion

A kind of constitutive model of SMA is proposed in this paper, and the nonlinear dynamic response of a SMA gripper under bounded noise is studied. The harmonic driving signals and the random disturbance made up of bounded noise. The dynamic model of the system is established by Hamilton principle. The numerical and experimental results show that there is stochastic resonance in the system; the system's vibration amplitude reaches the most when the outside excitation is moderate.

Acknowledgements

The authors gratefully acknowledge the support of NSFC through Grant Nos. 11872266 and 51875396, Chinese Aviation Science Foundation through Grant No. 2016ZA48001, Tianjin RPAFAT through Grant No. 16JCYBJC18800, and Cast-Bisee 511 Program through Grant No. CAST-BISEE2017-006.

References

[1] B. Winzek, S. Schmitz, and H. Rumpf. Materials Science and Engineering A **3** (2004),.
[2] M. Kohl, B. Krevet, and E. Just. Sensors and Actuators A-Physical **2** (2001).
[3] E. Just, M. Kohl, and S. Miyazaki. Journal de Physique IV **8** (2001).
[4] E.J. Graesser and F.A. Cozzarelli. Journal of Intelligent Material Systems and Structures **5** (1994).

[5] Y. Ivshin and T.J. Pence. Journal of Intelligent Material Systems and Structures **5** (1994).
[6] Z.W. Zhu, Q.X. Zhang and J. Xu. Thin Solid Films **4** (2014).

Comparative analysis of common full scale reactors for dry anaerobic digestion process

Khaled Elsharkawy, *Mohamed* Elsamadony[1], and *Hafez* Afify

Public Works Engineering Department, Faculty of Engineering, Tanta University, 31521 Tanta City, Egypt

Abstract. Organic solid wastes are produced with large amount wherever there are human activities. However, improper treated organic wastes made them as sources of diseases. On the other hand, these fractions contain nutrients and energy, so they have also valuable resources. As a result, exploring their potential as an energy source can be accomplish via anaerobic digestion process, in which, organics converted into hydrogen, methane and/or ethanol. Therefore, this manuscript introduces an overview of the common applied types of reactor that can handle these types of wastes in their solid state and recover them in term of biogas, as well as, stabilize the produced digestate to bio-fertilizers by compositing approach. A comparison also listed to demonstrate the optimum operational conditions and expected amount of biogas from each type.

1 Introduction

Incredible growing amount of solid waste is a crucial challenge worldwide. Consequently, environmental management of solid waste produced every year has to be safely disposed without any negative impact to the environment [1]. Anaerobic conversion of organic wastes to renewable source of energy appears to be one of the most promising methods [2, 3], since anaerobic digestion process can handle many types of organic solid waste such as organic faction of municipal solid waste (OFMSW) [4–6], industrial solid waste [7, 8] and agro-lignocellulosic waste [9–11]. These types of wastes are free of charge since they are waste and has to be disposed, plentiful, and composed of high organic fraction, which is preferable substrate to anaerobic consortium [12].

It must be noted that there are other technologies that have the ability to convert the organic wastes to energy form, i.e water electrolysis [13], as well as, thermo-catalytic reformation that can extract H_2 gas from organic molecules [14]. The main drawback face this technologies is the electricity requisite during operation which limited the net gain energy and reduce the efficiency of these process. As a result, biological treatment of organic waste gains great interest especially anaerobic digestion process (AD). This is because being anaerobic which means no aeration tools are required, in turn, operational and maintenance costs are significantly reduced, besides AD has the ability to extract all the carbon and hydrogen atoms from organic molecule and transfer them to the form of methane (CH_4) and carbon dioxide (CO_2), in addition using mixed culture bacteria at the process make AD able to deal with different types of organic wastes [15, 16]

.

AD process has been categorized into dry AD process that deal with waste contains total solid (TS) content larger than 20% (w/w) and wet AD which only loaded with TS lower than 10% (w/w). In this concern, dry AD found to be more efficient that wet type, since wet process requires large reactor capacity to handle the same amount of organic content due to the high water content. This surely will needs high energy for pumping, mixing and handling these amount of wet wastes. Furthermore, the produced digestate is larger than the dry process. Moreover, the net biogas production of dry will outweighs the wet production [17]. However, many different types of dry AD reactors were previously introduced, therefore an objective function must be applied to determine the optimum type to utilize for certain substrate [18] . Therefore, the aim of this manuscript is to describe the commercial types of dry AD reactors and compare between them in terms of operational conditions, advantages of each type and the estimated biogas production related to reactor capacity.

[1] Corresponding author: mohamed.elsamadony@f-eng.tanta.edu.eg

2 Anaerobic digestion pathway

Organic compounds utilized anaerobically through a variety of microorganisms that cooperated in order to generate a stable anaerobic digestion process [11]. AD process starts with hydrolytic bacteria that hydrolyze polymeric proteins and sugars into monomeric molecules. Afterwards, fermentative bacteria create organic acids, hydrogen and carbon dioxide from monomeric molecules as declared in Fig. 1. Hence, hydrogen and acetic acid can be utilized and/or produced by several microbial groups. Acetate formed during homoacetogenesis process from hydrogen and carbon dioxide reduction by autotrophic homoacetogens through the Wood–Ljungdahl pathway [19].
Completion of organic particulates consumption by anaerobic consortia occurred when organic acids and H_2 utilized by acetoclastic / hydrogenotrophic methanogens and generated methane and carbon dioxide [20].

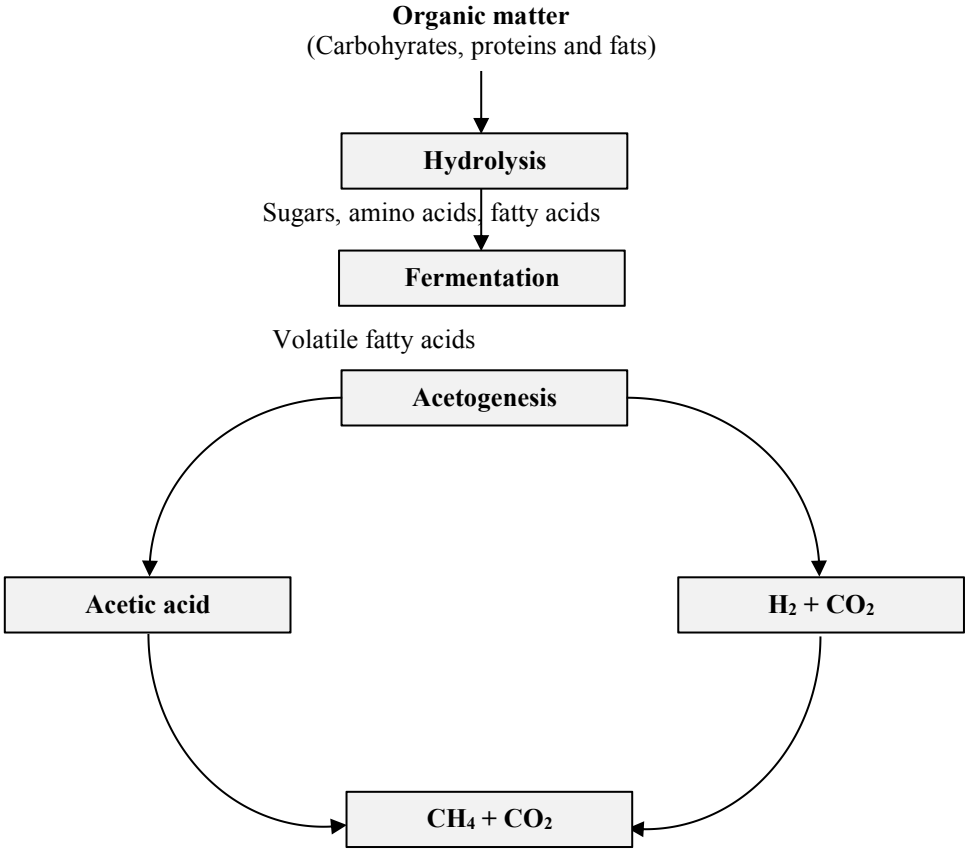

Fig. 1. Anaerobic degradation pathways of organic wastes.

3 One stage commercial dry anaerobic systems

Dry anaerobic system refers to systems that able to anaerobically treat organic waste with solid content in the range of 20 - 40%. These systems require a good mechanically pretreatment tool to sustain smaller particle size and robust pumps to handle impurities [21]. Table 1 illustrates a comparison between the most common three designs of Kompogas, Valorga and Dranco process.

Table 1
Comparison between one stage commercial dry anaerobic digesters [22].

Reactor type	**KOMPOGAS**	**VALORGA**	**DRANCO**
Country of incorporation	Switzerland	France	Belgium
Establish	1980	1982	1992

year			
No. of Plants	38	22	17
Capacity (ton/year)	1000-110000	10000-270000	3000-120000
Advantages	• Can deal with organics have solid content doesn't exceed 30% • Full waste stabilization and hygienisation. • Stable biogas production. • Digestate free of pathogens due to thermophilic conditions. • Avoiding short circuiting of organic waste.	• This technique does not require a large land area. • Baffles sustain a good contact and avoid dead zones. • High net gain energy with high methane content gas.	• Tolerate high solid wastes to the range of 30-45% and high organic loading rates of 5-8 kg_{VS}/m^3/day. • Small reactor volumes. • Vertical reactor avoiding waste accumulation. • Minimum surface area required for reactor installation. • Easy to operate with no mixing or gas injection. • Thermophilic operation which avoid pathogens formation.
Biogas Yield (m^3/kg)	0.08-0.16	0.103	0.11-0.14
Retention Time (Days)	18-23	15-30	20

Organic wastes in solid state have large scale which can't pass into the dranco system until they subjected to mechanical pretreatment to sustain a maximum particle size of 6 cm. On the other hand, anaerobic digestion process is remarkably diminished when TS exceeds 35%, therefore, dissolution using acidification process is required prior to introduce AD process. However, this step is unnecessary at Dranco system, since a digestate recirculation is applied with ratio 1/8 of raw organic waste / effluent digested waste in order to confirm proper inoculation (Fig. 2). Moreover, the dranco system runs under thermophilic condition (48 to 55 °C) via steam injection coupled with down flow mode as the mixture loaded to top of the digester using mixing recirculation pump. The designed operational conditions are hydraulic retention time (HRT), organic loading rate (OLR) and pH of 20 days, 5 to 8 kg_{VS}/m^3/day and 8, respectively, as well as, this type can tolerate organic waste with TS content at the range of 30 to 45% (w/w). Furthermore, no supplemented stirrer attached to this type of reactor which attributed to localized dead zones inside the reactor body, in turn, the performance may be affected since the amount of generated biogas reduced by around 30%. However, this design was applied at many countries with different capacities. The expected biogas yield is in the range of 110 to 140 m^3/ton and digestate amounted to be 0.4 ton/ton which further subjected to dewatering process and stabilized in composting bond. The net generated electricity after subtracting the utilized energy for operating the plant is approximately 150 kWh/ton [23].

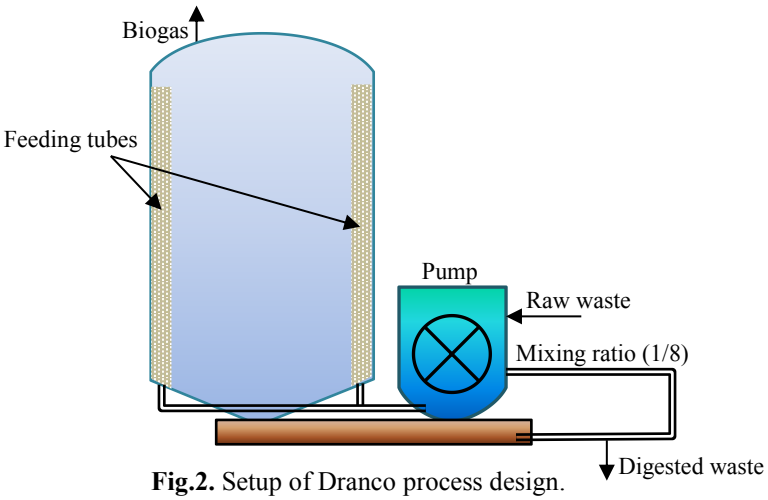

Fig.2. Setup of Dranco process design.

Kompogas reactor is similar to dranco design but with horizontal plug flow and inner slow rotators to provide homogeneous flow and avoid settling of heavier particles (Fig. 3). But the main disadvantage of this proposed design is take large surface area than dranco with same capacity. In addition, solid content lower than 23% and/or higher than 30% (w/w) is a problematic issue, since at TS of 23% heavy particle sink and accumulate at the bottom of the reactor while exceeding 30% block the horizontal flow and hinder the process. As a result, a careful control of the influent TS at the limit of 30% (w/w) is necessary. However, this design provides homogeneous flow avoiding short circuiting of organic waste. Moreover, the reactor runs at thermophilic condition 55-60 °C which guarantees killing pathogens at the effluent. The operational HRT ranged from 18 to 23 days and the harvested biogas is 80-160 m^3/ton [22].

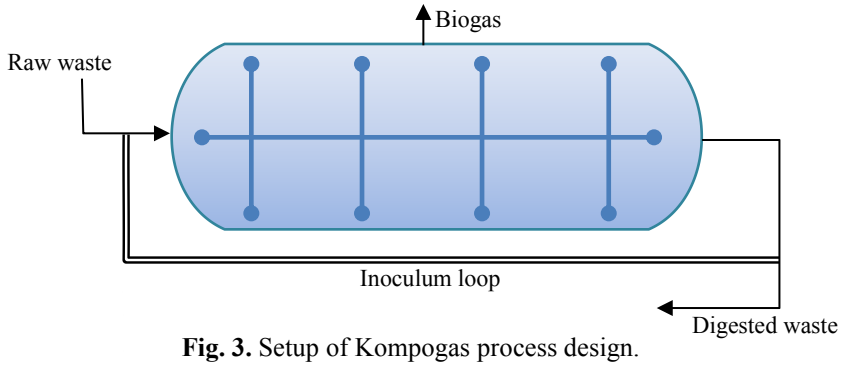

Fig. 3. Setup of Kompogas process design.

Valorga process (Fig. 4) started after the feedstock subjected to mechanical pretreatment to reduce the particle size to around 3 cm and mixed with returned effluent digestate and steam to provide mixture with temperature and solid content of 40 °C and 35% (w/w) before AD process. The operational condition for Valorga system are HRT ranged from 15 to 30 days and pH around 8 without external use of chemicals. In the case of pH decline, the reactor operates at batch mode until pH recovered then continuous feeding regime start again. The stirring process occurs by biogas reinjection to the reactor with high pressure of 5 bar at the bottom of the reactor [24, 25]

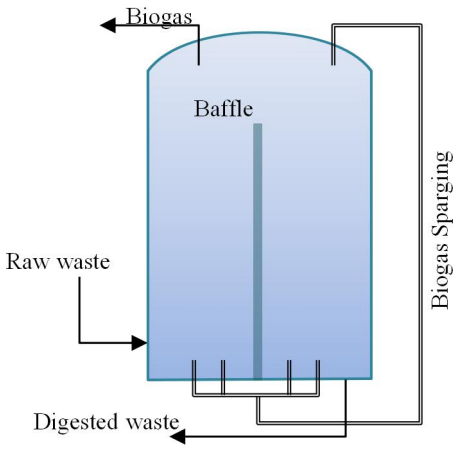

Fig. 4. Setup of Valorga process design.

Data collected from real installed reactors of each type have been displayed in Fig. 5 [22, 23], which presented the relation between the annual biogas productions versus the capacity of the reactor. Kompogas and Dranco process exhibited polynomial functions with correlation factors (R^2) of 0.94 and 0.99, respectively. On the other hand, Valorga process showed power relationship with R^2 of 0.94. Moreover, each system was suitable to certain loading capacity, whereas, Kompogas was better than other types when dealing with capacity lower than 50000 t/year. This was not the case when capacity exceeding this limit, in which, Dranco was the best at the medium loading capacity less than 100000 t/year, however, large capacity over the aforementioned limit exihibited a reduction in the performance of Kompogas and Dranco, while Valorga revealed maximum biogas generation.

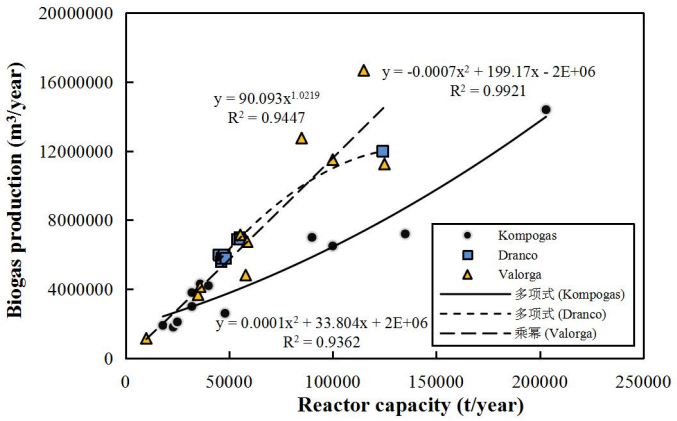

Fig. 5. Comparative production harvested from real full scale digesters

4 Conclusions

Dry anaerobic digestion is a pioneer strategy that able to disposal of organic solid wastes by converting them into biogas generation and fertilizer. There are three main types of reactor Kompogas, Dranco and Valorga, each one has its advantage and disadvantage. However, from energetic point of view, collected data exhibited that Kompogas is recommended at low reactor capacity lower than 50000 t/year, while Dranco is preferable at medium reactor capacity below 100000 t/year. However, Valorga found to have a superior performance in term of annual biogas generation at high reactor capacity exceeded 100000 t/year.

References

1. Elsamadony, M., Tawfik, A., Danial, A., Suzuki, M.: Use of Carica Papaya Enzymes for Enhancement of H2 Production and Degradation of Glucose, Protein, and Lipids. Energy Procedia. 75, 975–980 (2015).
2. Ismail, S., Elsamadony, M., Elreedy, A., Fujii, M., Tawfik, A.: Physico-chemical and microbial characterization of compartment-wise profiles in an anammox baffled reactor. J. Environ. Manage. 232, 875–886 (2019).
3. Ismail, S., Elsamadony, M., Fujii, M., Tawfik, A.: Evaluation and optimization of anammox baffled reactor (AnBR) by artificial neural network modeling and economic analysis. Bioresour. Technol. 271, 500–506 (2019).
4. Elsamadony, M., Tawfik, A., Danial, A., Suzuki, M.: Optimization of hydrogen production from organic fraction of municipal solid waste (OFMSW) dry anaerobic digestion with analysis of microbial community. Int. J. Energy Res. 39, 929–940 (2015).
5. Elsamadony, M., Tawfik, A.: Dry anaerobic co-digestion of organic fraction of municipal waste with paperboard mill sludge and gelatin solid waste for enhancement of hydrogen production. Bioresour. Technol. 191, 157–165 (2015).
6. Elsamadony, M., Tawfik, A., Suzuki, M.: Surfactant-enhanced biohydrogen production from organic fraction of municipal solid waste (OFMSW) via dry anaerobic digestion. Appl. Energy. 149, 272–282 (2015).
7. Farghaly, A., Elsamadony, M., Ookawara, S., Tawfik, A.: Bioethanol production from paperboard mill sludge using acid-catalyzed bio-derived choline acetate ionic liquid pretreatment followed by fermentation process. Energy Convers. Manag. 145, 255–264 (2017).
8. Mostafa, A., Elsamadony, M., El-Dissouky, A., Elhusseiny, A., Tawfik, A.: Biological H2potential harvested from complex gelatinaceous wastewater via attached versus suspended growth culture anaerobes. Bioresour. Technol. 231, 9–18 (2017).
9. Soltan, M., Elsamadony, M., Tawfik, A.: Biological hydrogen promotion via integrated fermentation of complex agro-industrial wastes. Appl. Energy. 185, 929–938 (2017).
10. Elsamadony, M., Tawfik, A.: Maximization of hydrogen fermentative process from delignified water hyacinth using sodium chlorite. Energy Convers. Manag. 157, 257–265 (2018).
11. Wazeri, A., Elsamadony, M., Tawfik, A.: Carbon emissions reduction by catalyzing H2 gas harvested from water hyacinth fermentation process using metallic salts. Energy Procedia. 152,

1254–1259 (2018).
12. Dias, T., Fragoso, R., Duarte, E.: Anaerobic co-digestion of dairy cattle manure and pear waste. Bioresour. Technol. 164, 420–3 (2014).
13. Turner, J., Sverdrup, G., Mann, M.K., Maness, P., Kroposki, B., Ghirardi, M., Evans, R.J., Blake, D.: Renewable hydrogen production. Int. J. Energy Res. 32, 379–407 (2008).
14. Irmak, S., Öztürk, İ.: Hydrogen rich gas production by thermocatalytic decomposition of kenaf biomass. Int. J. Hydrogen Energy. 35, 5312–5317 (2010).
15. Tawfik, A., Salem, A.H.: Optimization of hydrogen production from pretreated rice straw waste in a mesophilic up- fl ow anaerobic staged reactor. Int. J. Energy Res. (2013).
16. Wazeri, A., Elsamadony, M., Roux, S. Le, Peu, P., Tawfik, A.: Potentials of using mixed culture bacteria incorporated with sodium bicarbonate for hydrogen production from water hyacinth. Bioresour. Technol. 263, 365–374 (2018).
17. Romero Aguilar, M. a., Fdez-Güelfo, L. a., Álvarez-Gallego, C.J., Romero García, L.I.: Effect of HRT on hydrogen production and organic matter solubilization in acidogenic anaerobic digestion of OFMSW. Chem. Eng. J. 219, 443–449 (2013).
18. Elsheikh, M.A., Saleh, H.I., Rashwan, I.M., El-Samadoni, M.M.: Hydraulic modelling of water supply distribution for improving its quantity and quality. Sustain. Environ. Resour. 23, 403–411 (2013).
19. Mu, V.: Energy Conservation in Acetogenic. Appl. Environ. Microbiol. 69, 6345–6353 (2003).
20. Tawfik, A., Elsamadony, M.: Development of Dry Anaerobic Technologies of Bio-waste and Unlock the Barriers for Valorization. In: Purohit, H.J., Kalia, V.C., Vaidya, A.N., and Khardenavis, A.A. (eds.) Optimization and Applicability of Bioprocesses. pp. 267–282. Springer Singapore, Singapore (2017).
21. Elsamadony, M., Tawfik, A.: Potential of biohydrogen production from organic fraction of municipal solid waste (OFMSW) using pilot-scale dry anaerobic reactor. Bioresour. Technol. 196, 9–16 (2015).
22. Rapport, J., Zhang, R., Jenkins, B.M., Williams, R.B., Schwarzenegger, A., Adams, L.S., Brown, M.R., Chair, B., Chesbro, W., Member, B., Petersen, G., Mulé, R.: Current Anaerobic Digestion Technologies Used for Treatment of Municipal Organic Solid Waste. (2008).
23. De Baere, L.: The Dranco Technology: A unique digestion technology for solid organic waste. Org. Waste Syst. Pub. Brussels, Beligium. 1–8 (2010).
24. Benbelkacem, H., Bollon, J., Bayard, R., Escudié, R., Buffière, P.: Towards optimization of the total solid content in high-solid (dry) municipal solid waste digestion. Chem. Eng. J. 273, 261–267 (2015).
25. Benbelkacem, H., Garcia-Bernet, D., Bollon, J., Loisel, D., Bayard, R., Steyer, J.P., Gourdon, R., Buffière, P., Escudié, R.: Liquid mixing and solid segregation in high-solid anaerobic digesters. Bioresour. Technol. 147, 387–394 (2013).

Enrich waste activated sludge digestibility via natural enzyme supplementation

Mohamed Elsamadony[1]

Public Works Engineering Department, Faculty of Engineering, Tanta University, 31521 Tanta City, Egypt

Abstract. Upgrading of low biodegradable waste activated sludge (WAS) accomplished through supplement the hydrolysis step with natural enzymes source. Whereas, WAS is rich in particulate fractions in terms of total chemical oxygen demand (tCOD), total suspended solids (TSS) and volatile suspended solids (VSS) of 15.78, 14.92 and 12.15 g/L, respectively. Therefore, carica papaya enzymes were utilized to break down the peptide ponds in protein molecules such as papain and protease, as well as, lipases that catalyzed the degradation of lipids. The optimum mixture between papain, protease, and lipase enzymes was found to be 3: 1: 2 while the optimum enzyme concentration was 8%. This conditions was attributed to enhance the H_2 productivity form WAS by 97.8%

1 Introduction

Large amount of wastewater generated daily from municipal and industrial activities which requires a proper treatment through physical and biological process. In this concern, abundant waste activated sludge (WAS) accumulates from secondary sedimentation tank located at wastewater treatment plants [1–3]. The classical technologies for stabilizing and managing this waste amounted about 40 to 60% of the operational cost, because the complex structure of particulate organic fractions originated at WAS [4]. Anaerobic digestion (AD) process represents an interesting choice to get rid of such a waste with add value in term of renewable energy source [5–8]. Whereas, AD has the ability to convert organic waste to energy carrier gases i.e. hydrogen and methane gases [9–14].

However, WAS is rich with protein and lipids fractions which that forms about 80% of the particulate organic fractions [15]. Therefore, pretreatment methods were applied on WAS prior to introduce to AD process to increase its solubility and make it easy to anaerobes to feed on [6]. One of the most common methods is the enzymatic hydrolysis, since it has the ability to reduce the lag phase, enhance the WAS digestibility and improve the liberation of extracellular polymeric substances (EPS) [16]. This is because enzymes such as amylase, protease and lipase degrade the complex polymeric substance and facilitate its transportation to subsequent acidogenesis microorganisms [17]. Protease and lipase producing microorganisms such as *Bacillus sp.* and *Acinetobacter calcoaceticus*, respectively revealed a decline of lipid concentration by 99% after twelve days when treating lipid rich wastewater under aerobic condition [18]. Moreover, the supplementation by lytic enzymes exhibited a COD degradation of 87% of pot ale residues via AD process. This was not the case when no enzymes were added, since only 13% were achieved [19].

On the other hand, commercial enzymes are too expensive which obstacle the practical application of the enzyme use at WAS pretreatment. Therefore, the aim of this study was to explore the availability of using a nature source to extract essential enzymes for WAS solubility such as papain, protease and lipase enzymes. This was accomplished by using Carica papaya plants. Furthermore, single and combined effect of the extracted enzymes on WAS hydrolysis were assessed. In addition, the concentration of the optimum enzymes mixture was tested and the maximum hydrogen potential was evaluated.

2 Material and methods

[1] Corresponding author: mohamed.elsamadony@f-eng.tanta.edu.eg

2.1. Waste activated sludge and enzymes extracted

Waste activated sludge (WAS) was collected from wastewater treatment plant located at Tanta city from the secondary sedimentation tank. The characteristics of the used WAS were as follows: pH, tCOD, sCOD, TSS and VSS equal to 6.82, 15.78, 0.93, 14.92 and 12.15 g/L, respectively. Papain (Pn), protease (Pt) and lipase (Lp) enzymes were extracted from the latex and peels according to methods explained earlier at the following [20–22].

2.3. Experimental setup

Three batch assays were carried out to estimate sing and mixed enzymes on WAS hydrolysis, as well as, determining the optimum concentration of the ideal mixture. 100 mL WAS were loaded to 250 mL serum bottles then loaded with enzymes according to procedure listed at Table 1. Afterwards, the bottles were purged with N_2 gas to maintain anaerobic condition at cultivated at mesophilic condition (35 °C).

Table 1.
Batch anaerobic experiments of single and mixed enzymes effect.

Exp. 1: Single enzyme effect	Exp. 2: Mixed-enzymes effect with fixed concentration 3% (w/w)	Exp. 3: Effect of enzymes mixture of Pn : Pt: Lp (2:1:3) concentrations
No enzyme addition	Pn : Pt: Lp (2:1:1)	1% (w/w)
3% (w/w) Pn	Pn : Pt: Lp (1:2:1)	2% (w/w)
3% (w/w) Pt	Pn : Pt: Lp (1:1:2)	4% (w/w)
3% (w/w) Lp	Pn : Pt: Lp (3:1:1)	6% (w/w)
	Pn : Pt: Lp (1:3:1)	8% (w/w)
	Pn : Pt: Lp (1:1:3)	10% (w/w)
	Pn : Pt: Lp (3:2:1)	15% (w/w)
	Pn : Pt: Lp (1:3:2)	20% (w/w)
	Pn : Pt: Lp (2:1:3)	

2.4. Analytical methods

Total suspended solids (TS), volatile suspended solids (VS) and chemical oxygen demand (COD were quantified according to APHA [28]. Cumulative biogas was amounted using displacement method. Besides, H_2 content in the eveloved biogas was determined by a gas chromatograph (GC) using method mentioned at [10].

2.5. Solubilization efficiency (%) and Hydrolysis coefficient

Solubilization efficiency of COD_t was obtained to assess the enzymatic hydrolysis effect. The COD solublization was calculated using the following equation, where, α is solubilization efficiency (%)

$$\alpha = \frac{\text{Hydrolyzed COD}_s - \text{Influent COD}_s}{\text{Influent COD}_t - \text{Influent COD}_s} \quad (1)$$

Hydrolysis of organic polymers is often described by a first-order kinetic model, Where, K_h is the solubilisation rate constant

$$-\frac{dX}{dt} = K_h.X \quad (2)$$

$$\ln X = -K_h.t + b \quad (3)$$

3 Results and discussions

3.1. Single enzyme effect on WAS solubility

Fig. 1a and b revealed the effect single effect of each enzyme type on the WAS solublization efficiency. The maximum solubilization efficiency of 27.6% was recorded when papain enzyme was supplemented with concentration of 3% followed by lipase and protease enzymes with percentages of 18.5 and 13.6%, respectively. This is because papain is a strong protein enzyme degrader and more than 60% WAS's organic content is complex protein fraction; therefore, papain enzyme achieved the maximum solublization efficiency [17].

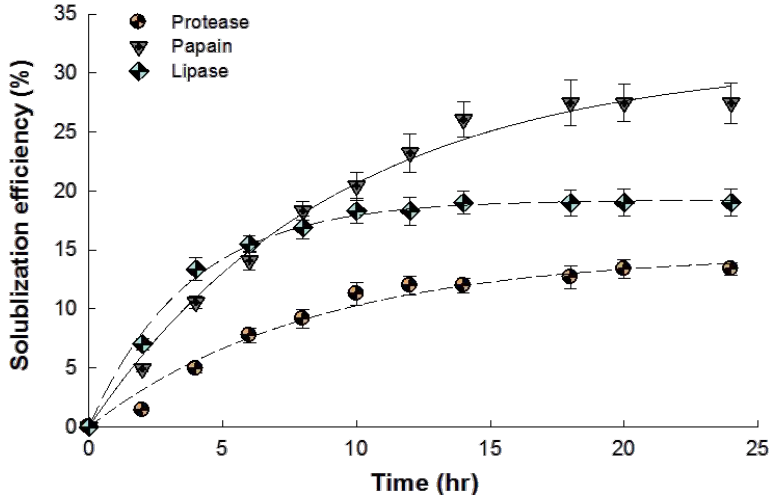

Fig. 1. Solublization efficieny (%) of WAS with single enzyme supplementation.

3.2. Mixed Enzymes effect on WAS solubility

In order to evaluate the synergistic effect of mixed enzymes supplementation, different mixtures of the three enzymes were examined. The optimum mixture was papain: protease: lipase enzymes ratios of 3:1:2. This mixture registered the highest solubilzation efficiency and hydrolysis rate constant of 47.2% and -0.03 h^{-1}, respectively. The synergistic effect between different enzymes were previously emphasized by Yang et al. [24], since they discovered that a significant reduction at VSS content was recorded when use a mixture 1 : 3 of amylase to protease exceeded the single effect of each of them.

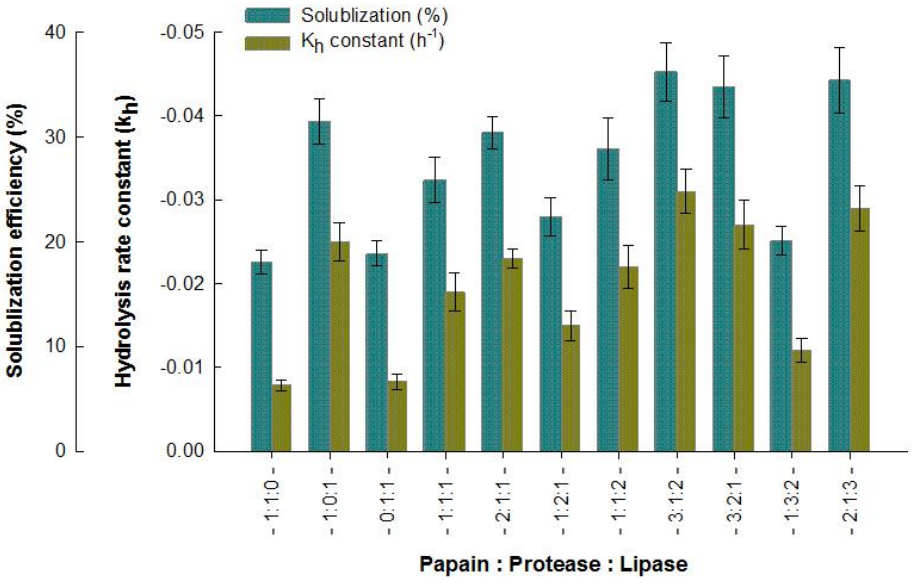

Fig. 2. Solublization efficieny (%) and hydrolysis rate constant of WAS under mixed enzyme supplementation.

3.2. Effect of enzyme concentration on WAS digestibility and H_2 productivity

Solublization efficiency found to be enzyme concentration dependent as explored from Fig. 3. However, after certain concentration a slight increase at solublization efficiency occurred. Similarly, hydrolysis rate constant were achieved the same trend. Maximum solublization efficiency was 52.6% at enzymes concentration of 20%, however, at concentration of 10% solublization efficiency was 47.9%. This means that with doubling the concentration, the solublization efficiency only incremented by 4.7%. On the other hand, H_2 potential were evaluated at different enzyme concentration, maximum H_2 productivity of 452.1 mL were noticed at enzyme concentration of 8% compared with only 228.6 mL at control batch (no enzymes were added). This is due to increasing the solubility of WAS structure, as well as, breaking down the complex compounds to simple compounds that anaerobes able to feed on and convert them into hydrogen. However, further enzyme concentration augmentation led to a reduction at H_2 productivity until reached 179.2 mL at concentration of 20%. This may as a result of enzymes is originally a protein molecule so at certain limit hinder the process, as well as, further dissolution of organics to tiny structure can penetrate the bacterial membrane and kill the anaerobes [16, 25].

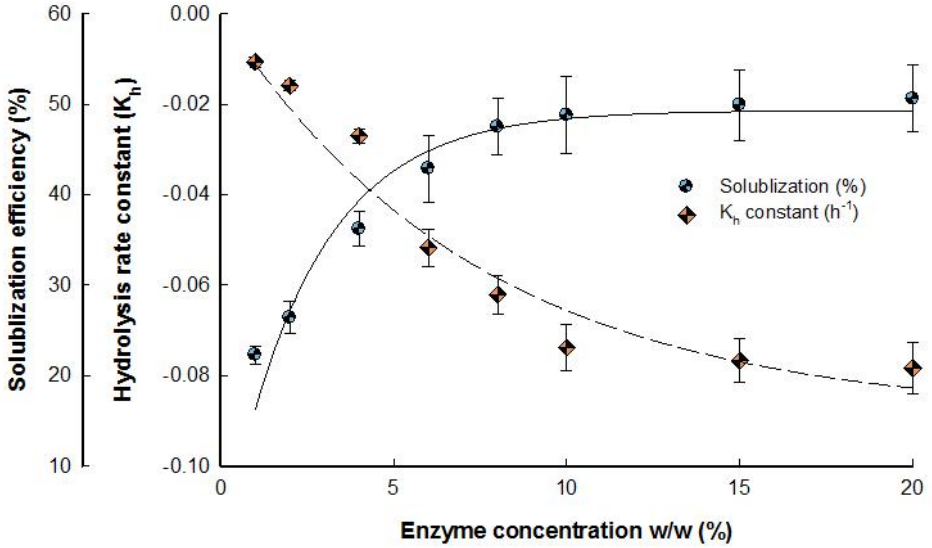

Fig. 3. Solublization efficieny (%) and hydrolysis rate constant of WAS versus enzymes concentration.

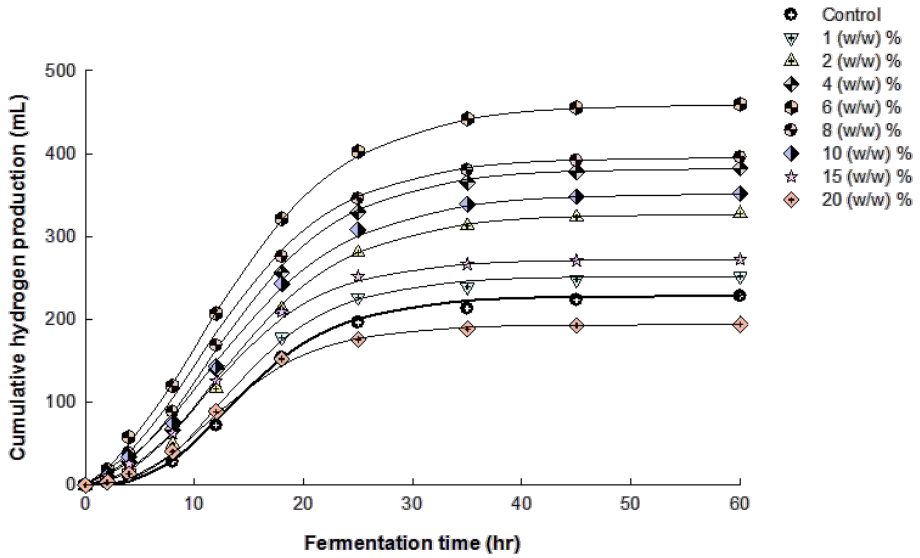

Fig. 4. Hydrogen potential harvested from WAS at different enzymes concentration.

4 Conclusions

Enzymes supplementation found to be an optimistic approach to enhance WAS solubility and improve hydrogen potential. Papain was the most effective enzyme, however, synergistic effect was found between the three tested enzymes with optimum ratio of papain: protease: lipase equal to 3: 1: 2. Moreover, the optimum enzyme mixture concentration was 8% which achieved the highest hydrogen potential of 452.1 mL.

References

1. Mostafa, A., Elsamadony, M., El-Dissouky, A., Elhusseiny, A., Tawfik, A.: Biological H2potential harvested from complex gelatinaceous wastewater via attached versus suspended growth culture anaerobes. Bioresour. Technol. 231, 9–18 (2017).
2. Elsheikh, M.A., Saleh, H.I., Rashwan, I.M., El-Samadoni, M.M.: Hydraulic modelling of water supply distribution for improving its quantity and quality. Sustain. Environ. Resour. 23, 403–411 (2013).
3. Tawfik, A., Elsamadony, M.: Development of Dry Anaerobic Technologies of Bio-waste and Unlock the Barriers for Valorization. In: Purohit, H.J., Kalia, V.C., Vaidya, A.N., and Khardenavis, A.A. (eds.) Optimization and Applicability of Bioprocesses. pp. 267–282. Springer Singapore, Singapore (2017).
4. Zhang, B., He, P. jing, L??, F., Shao, L. ming, Wang, P.: Extracellular enzyme activities during regulated hydrolysis of high-solid organic wastes. Water Res. 41, 4468–4478 (2007).
5. Farghaly, A., Elsamadony, M., Ookawara, S., Tawfik, A.: Bioethanol production from paperboard mill sludge using acid-catalyzed bio-derived choline acetate ionic liquid pretreatment followed by fermentation process. Energy Convers. Manag. 145, 255–264 (2017).
6. Elsamadony, M., Tawfik, A.: Maximization of hydrogen fermentative process from delignified water hyacinth using sodium chlorite. Energy Convers. Manag. 157, 257–265 (2018).
7. Ismail, S., Elsamadony, M., Elreedy, A., Fujii, M., Tawfik, A.: Physico-chemical and microbial characterization of compartment-wise profiles in an anammox baffled reactor. J. Environ. Manage. 232, 875–886 (2019).
8. Ismail, S., Elsamadony, M., Fujii, M., Tawfik, A.: Evaluation and optimization of anammox baffled reactor (AnBR) by artificial neural network modeling and economic analysis. Bioresour. Technol. 271, 500–506 (2019).
9. Wazeri, A., Elsamadony, M., Tawfik, A.: Carbon emissions reduction by catalyzing H2 gas harvested from water hyacinth fermentation process using metallic salts. Energy Procedia. 152, 1254–1259 (2018).
10. Soltan, M., Elsamadony, M., Tawfik, A.: Biological hydrogen promotion via integrated fermentation of complex agro-industrial wastes. Appl. Energy. 185, 929–938 (2017).
11. Elsamadony, M., Tawfik, A.: Dry anaerobic co-digestion of organic fraction of municipal waste with paperboard mill sludge and gelatin solid waste for enhancement of hydrogen production. Bioresour. Technol. 191, 157–165 (2015).
12. Elsamadony, M., Tawfik, A., Danial, A., Suzuki, M.: Optimization of hydrogen production from organic fraction of municipal solid waste (OFMSW) dry anaerobic digestion with analysis of microbial community. Int. J. Energy Res. 39, 929–940 (2015).
13. Elsamadony, M., Tawfik, A.: Potential of biohydrogen production from organic fraction of municipal solid waste (OFMSW) using pilot-scale dry anaerobic reactor. Bioresour. Technol. 196, 9–16 (2015).
14. Elsamadony, M., Tawfik, A., Suzuki, M.: Surfactant-enhanced biohydrogen production from organic fraction of municipal solid waste (OFMSW) via dry anaerobic digestion. Appl. Energy. 149, 272–282 (2015).
15. Wazeri, A., Elsamadony, M., Roux, S. Le, Peu, P., Tawfik, A.: Potentials of using mixed culture bacteria incorporated with sodium bicarbonate for hydrogen production from water hyacinth. Bioresour. Technol. 263, 365–374 (2018).
16. Donoso-Bravo, A., Fdz-Polanco, M.: Anaerobic co-digestion of sewage sludge and grease trap: Assessment of enzyme addition. Process Biochem. 48, 936–940 (2013).
17. Elsamadony, M., Tawfik, A., Danial, A., Suzuki, M.: Use of Carica Papaya Enzymes for Enhancement of H2 Production and Degradation of Glucose, Protein, and Lipids. Energy Procedia. 75, 975–980 (2015).
18. Mongkolthanaruk, W., Dharmsthiti, S.: Biodegradation of lipid-rich wastewater by a mixed bacterial consortium. Int. Biodeterior. Biodegradation. 50, 101–105 (2002).
19. Mallick, P., Akunna, J.C., Walker, G.M.: Anaerobic digestion of distillery spent wash:

Influence of enzymatic pre-treatment of intact yeast cells. Bioresour. Technol. 101, 1681–5 (2010).
20. Nitsawang, S., Hatti-Kaul, R., Kanasawud, P.: Purification of papain from Carica papaya latex: Aqueous two-phase extraction versus two-step salt precipitation. Enzyme Microb. Technol. 39, 1103–1107 (2006).
21. Chaiwut, P., Pintathong, P., Rawdkuen, S.: Extraction and three-phase partitioning behavior of proteases from papaya peels. Process Biochem. 45, 1172–1175 (2010).
22. PAQUES, F., PIO, T., CARVALHO, P., MACEDO, G.: Characterization of the lipase from Carica papaya residues. Brazilian J. food Technol. 11, 20–27 (2008).
23. APHA: Standard Methods for the Examination of Water and Wastewater. , Washington, DC, USA (2005).
24. Yang, Q., Luo, K., Li, X. ming, Wang, D. bo, Zheng, W., Zeng, G. ming, Liu, J. jin: Enhanced efficiency of biological excess sludge hydrolysis under anaerobic digestion by additional enzymes. Bioresour. Technol. 101, 2924–2930 (2010).
25. Romano, R.T., Zhang, R., Teter, S., McGarvey, J.A.: The effect of enzyme addition on anaerobic digestion of Jose Tall Wheat Grass. Bioresour. Technol. 100, 4564–4571 (2009).

Problems and Countermeasures in Environmental Cost Accounting: A Case Study of China's Coal Industry

Li-Xia Zeng[1], *Peng* He[2,*], *Jin-Ping* Shi[1]

[1]College of Economics and Management, Xiamen University of Technology, China

[2]School of Cultural Industries and Tourism, Xiamen University of Technology, China

Abstract. In recent years, many scholars have carried out research on improving the environmental cost accounting of coal enterprises. Through the research, the traditional product cost accounting and environmental cost accounting are standardized. But the current cost accounting system still exists problems like wrong calculation of the cost of environmental damage and fraudulent accounting problems. In order to enhance the enterprise's environmental protection consciousness and improve the level of cost control management for the enterprise to provide scientific decision basis, this paper aims to find out the main composition of coal enterprise environment cost, analysis of the problems existing in coal enterprise environment cost accounting and puts forward corresponding solutions.

1 Introduction

In the process of coal mining, coal enterprises not only cause serious pollution to the environment of the mining area, but also cause pollution to the environment outside the mining area. While having a tangible impact on the environment, the pollution also affects the growth of plants, which then exerts influence on the ecological environment. Compared with other industries, coal enterprises have more prominent problems in sustainable development, suffer from more damages in resource and environment destruction and have to pay more to protect resources and environment. Therefore, it is of great theoretical value and practical significance for the development of coal enterprises to correctly understand and study the environmental costs and to strengthen the control of environmental costs.

The Outline of the *13th Five-Year Plan* for National Economic and Social Development, promulgated and implemented by China in 2015, sets specific requirements for enterprises to assume social responsibility and control environmental pollution. The 19th CPC National Congress has put forward new goals and new requirements for building ecological civilization and protecting ecological environment. In recent years, in order to give full play to the role of ecological environmental protection in promoting supply-side structural reform and speeding up the upgrading of the industrial structure, many scholars have carried out studies on how to improve coal enterprises' environmental cost accounting and

* Corresponding author: 2010110404@xmut.edu.cn

coal cost accounting methods. Through the research, the traditional product cost accounting and environmental cost accounting are standardized. However, there are still some problems in the current cost accounting system, such as incomplete and false calculation of environmental damage costs that enterprises should bear. In order to enhance enterprises' awareness of environmental protection, improve the level of cost management, truly reflect the coal cost, provide scientific basis for companies' management departments to improve cost controlling level, and offer references for macroeconomic management departments to approve the environment protection costs that enterprises should bear, studies on perfecting environmental cost accounting based on the traditional product cost accounting system have been conducted and it has become one of the most important research topics in recent years.

2 Literature review

The environmental cost is a part of social costs. It is a historical category and the product of a certain social and historical period under a certain industrial structure. In the face of the worsening ecological environment, since the 1960s, the academic circles have focused on "the road of environmental economy" to realize environmental return, and they have set up the theory of "light green" and "deep green". Both of the theories try to solve ecological environment problems. The studies on environmental cost accounting began in the 1970s, marked by The Study of the Social Cost Transformation of Pollution Control written by Beamons in 1971 and Ma Lin's article Accounting Problems of Pollution written in 1973. The United Nations intergovernmental working group of experts on International Standards of Accounting and Reporting (ISAR) (1998) defines environmental costs as the costs which are incurred when an enterprise takes its social responsibility to repair, actively or passively, the environmental damages caused by its production, also including other relative costs for reaching environmental goals. These costs include environmental maintenance costs, environmental treatment costs, environmental pollution compensation costs, environmental development costs and environmental loss costs. Germany adopts the ecological accounting model for environmental cost accounting, that is, measuring the influence degree of various environmental loads by physical and chemical units using the principle of flow balance between the material and energy input into the enterprise and the product and waste output into the environment, and on this basis calculating environmental costs and analyzing the input-output effects. Environmental costs mandated by the United States Environmental Protection Agency in 2000 include: (a) traditional costs: the portion of traditional costs that relates to environmental protection; (b) potential hidden costs: costs incurred prior to the commencement of production and business operations, costs paid for complying with environmental laws and regulations, and costs incurred after enterprises cease production and operation activities; (c) contingent costs: expenses that may need to be paid in the future; (d) image-associated costs: the costs for fulfilling enterprise social responsibility.

The studies on environmental reports in Japan began in the 1990s. At the end of the 20th century, Japan proposed the concept of "Circular Economy Society". Enterprises began to pay more and more attention to environmental costs. The Ministry of Environment (formerly The Environment Department) successively published the Environmental Report and explained in detail. In 2005, the Australian practice field divided the costs of coal enterprises into raw coal production costs, construction costs of underground mines, environmental protection costs, and taxes and fees. In summary, it can be seen that the developed countries such as the United States, Japan, Germany and Australia have studied the definition, classification, measurement and information disclosure of enterprise environmental costs to varying degrees, and have achieved certain results. Foreign experts believe that enterprise environmental costs should be included in the accounting system.

However, since experts and scholars in various countries carry out studies based on their own countries' conditions, the focuses and research directions are different. Each one has its own merits, and the research results also differ. This is why a more unified theoretical system has not yet formed.

3 The main composition of environmental cost of coal enterprises

(a) Costs of coal consumption. Coal is a non-renewable resource that nature gives to human beings. The consumption of coal resources is irreversible. Human beings cannot re-create coal in their own way. Coal mining and processing by coal enterprises leads to the continuous shrink of this resource. Coal resources are valuable, and the resources themselves do not belong to coal enterprises at the very beginning. Therefore, coal enterprises should pay a certain amount of money to get coal resources for mining. This expenditure is the cost of coal resource consumption. This cost should be included into the environmental cost accounting of coal enterprises. This cost is paid mainly through the form of taxes and fees, such as mineral resources compensation fees and resource taxes.

(b) Exploration costs of coal resources. This cost is caused when coal enterprises conduct exploration activities at the target spots, estimate coal resource reserves and economic value before the coal mining. It mainly includes geological survey fees, mining rights fees and reserves estimation fees.

(c) Environmental prevention costs. Environmental prevention costs are paid by coal enterprises before they cause pollution and damage to the environment, or to reduce the costs of pollution and emissions, including costs from purchasing advanced air and water purification equipment, raising the processing level, and engineering fees of preventing surface subsidence and solid waste discharge, etc. The cost of emission testing is included as well.

(d) Environmental governance costs. Coal enterprises will cause damages of various degrees to nature during coal mining and processing, such as water pollution, air pollution, solid waste discharge and accumulation, surface subsidence and vegetation destruction. Coal enterprises need to pay a certain price to compensate for the environmental problems caused by themselves and restore the original appearance of nature as much as possible.

(e) Environmental impact costs. The coal mining process may cause surface subsidence, and the surrounding topography and soil quality will be affected to varying degrees. Coal enterprises need to bear the relocation costs of the nearby residents, the compensation fees for the damages caused to crops, the costs of filling the subsidence area, etc.

(f) Costs of ecological environment damage. While consuming various natural resources, coal enterprises are also destroying the ecological environment and the balance of ecosystems. They are disturbing the water cycle system, the forest system and other minerals. These damages should be compensated for by the coal enterprises, rather than other social entities.

(g) Environmental management and education costs. The environmental management costs mainly include the expenses incurred by the environmental protection department's daily environmental monitoring, certification and inspection. The environmental education costs

are caused by environmental knowledge lectures and trainings that coal enterprises organize to mobilize all employees to participate in environmental protection activities.

4 Problems in environmental cost accounting of Chinese coal enterprises

(a) Environmental cost measurement is unscientific. The measurement of environmental costs is a process of quantifying the confirmed result of environmental costs. It is a process which identifies and calculates the amount, quantity, and unit price through certain analysis and using certain measurement units and attributes. For some environmental costs that cannot be measured by currency, enterprises have not found a suitable, closely related and matching measurement method, and the same measurement method has been adopted for environmental costs of different nature. All these will inevitably lead to the inaccuracy of the measurement of enterprises' environmental costs. The environmental cost forecast is unscientific and incomplete, and some environmental damages that should be included in the product costs are excluded from enterprises' confirmed lists of environmental costs. Therefore, the final environmental costs can not fully reflect the real degree of environmental damages. As a result, it is not conducive for enterprises to do cost control and reduction in the later stage of work; managers can not correctly estimate the influence of environmental costs on the business operation according to the accounting results; governments can not make correct evaluations of the environmental damages caused by coal enterprises.

(b) The accounting mechanism of enterprise environmental costs has flaws. The vast majority of coal enterprises have not conducted complete and meticulous analysis and studies on environmental factors, and have not fully incorporated financial accounting into environmental costs accounting. The environmental costs thus can not be separated from the product costs generated in the normal production process. Enterprises can not effectively control the environmental costs, so it is difficult to avoid the corresponding risks. False accounting may happen in the existing cost accounting of coal enterprises due to the absence of a sound environmental cost accounting mechanism.

(c) Information disclosure is an important procedure of the environmental accounting information system. Only through disclosure procedure can enterprises transfer environmental cost information to information users. Environmental cost reports are of great significance for information users to correctly understand environmental cost information. However, the current environmental disclosure of coal enterprises can not meet the requirements of enterprise decision makers, and thus enterprises' internal and external decision-making is affected. The disclosed content is mainly about monetary information measured by historical cost, while in environmental accounting it is the non-monetary information that accounts for a majority. In addition, some items that can not be measured by historical cost are not disclosed in the accounting report either. In fact, the non-monetary information is an important supplement to environmental cost accounting, such as the measurement of pollutant emissions and waste disposal, explanations on enterprises' environmental policy and objectives, impacts of environment damaging or improving on enterprises' financial situations, operating results and cash flow, and the performance of enterprises in environmental fiduciary responsibilities. This kind of information can more comprehensively reflect the attitude of coal enterprises towards environmental issues, as well as their efforts and achievements in environmental protection and resource conservation.

(d) Accounting laws and regulations in environmental cost accounting is absent. In Accounting Law, Accounting Standards for Enterprises and other relevant accounting laws and regulations, there are no detailed provisions on enterprise environmental costs accounting. No unified requirements are made for the objects, measurement, principles and information disclosure of environmental cost accounting. Unified guidelines and standards are also absent. Enterprises can only follow the environmental protection requirements in relevant national policies, which is the reason why different enterprises have different treatment, reports and analysis. Due to the late start of environmental accounting in China, though in recent years many scholars have devoted themselves to the studies on the confirmation, measurement and record of environmental costs, the studies still stay at the theoretical level, and the empirical research on environmental costs is still insufficient. As a result, the confirmation and measurement of environmental costs and the setting of environmental cost accounting subjects are quite random, which affects accounting accuracy, integrity and scientificity.

(e) The management layer of coal enterprises fails to pay enough attention to the accounting and management of environmental costs, but put their emphasis on the pursuit of coal production and maximization of economic benefits. Sound environmental cost rules and regulations have not been established inside enterprises, and finance departments in enterprises have not set up special environmental cost accounting posts to carry out environmental cost control, so a well-founded environmental cost accounting and management system has yet to be formed. The consequence is that enterprises can not achieve coordination between profit growth and environmental benefits, which is contrary to sustainable development. The main goal of coal environmental cost accounting is to offer useful environmental cost information to the outside and to optimize the internal cost control. The environmental cost has little influence on the stock price of coal enterprises. The empirical research shows that the environmental cost has no direct impact on the stock prices of listed companies and the coal industry because China's capital market has not been mature enough. The environmental cost and environmental responsibility index have a weak positive correlation with the changes of stock prices. Therefore, the financial staff hold slack attitude towards environmental cost accounting and its improvement, and coal enterprises also ignore it correspondingly.

5 Countermeasures to strengthen environmental cost control of coal enterprises

(a) Optimizing the measurement of environmental costs.
The measurement of environmental cost in coal enterprises mainly has defects in measurement units, measurement attributes and metrological methods, so coal enterprises must optimize the measurement system. First of all, optimize the choice of measurement units and attributes. Generally, accounting measurement is based on currency, but due to the particularity of the environment, it is difficult to accurately respond to the problems in environmental costs with the currency-based measurement alone. Therefore, apart from the major currency-based measurement, coal enterprises also need labor indicators and physical indicators as supplement to measure environmental costs. At the same time, more measurement methods of environmental costs should be adopted, such as the application of historical costs, replacement costs and opportunity costs. Moreover, reasonable accounting subjects should be set up. According to the requirements of environmental cost accounting in coal enterprises, the accounting subjects include: environmental assets account, environmental debt account, environmental equity account, environmental cost account etc.

(b) Formulating the overall strategic plan of environmental governance by using value chain analysis .
The value chain analysis regards enterprises as a place where different activities interconnect with each other. The analysis factors in the environmental costs incurred in the process of production and operation. By analyzing the costs of various activities, the analysis links the costs and their related activities together. The value chain analysis includes: (i) the internal value chain analysis, which means equal attention should be paid to production and processes before and after production in order to find out the relationship between them and ultimately reduce the cost of coal products. (ii) the external value chain analysis, that is, the analysis of the relationship between suppliers and customers. Suppliers not only produce products or services used in the value chain, but also affects enterprises in other aspects. For example, the frequent delivery of goods from suppliers can reduce the inventory demand of enterprises. Customers also have their own value chains. The costs brought by the customers with small, uncertain orders are higher than those from the customers with large, pre-determined orders.

(c) Carrying out environmental pre-assessment of coal enterprises.
Environmental pre-assessment is an important part of environmental quality assessment. The implementation of environmental pre-assessment in coal enterprises plays an important role in the pre-control of environmental costs. The pre-evaluation takes the whole production process into consideration, allocates the possible environmental expenditures in the future and brings it into the product cost budget system. It puts forward various possible production schemes, and then evaluates them. In order to control the environmental cost, the scheme with the least environmental expenditure is selected from all the feasible programs to be implemented.

(d) Implementing the whole-process control.
Coal enterprises should carry out whole-process control of the environmental costs, which consists of ex-ante planning, interim control and ex-post control.
In ex-ante planning, the entire production process is factored in, possible environmental costs in the future are brought into the product cost budget system, a variety of feasible schemes are put forward, and then the value of each scheme is estimated and the best one is picked out to control environmental costs. The interim control is to control the process in which environment costs are generated. The main task of this stage is to track the production process, supervise and control the incurrence of environmental costs, collect and sort out the first-hand cost data, analyze the process of environmental cost incurrence, and coordinate the cost responsibility centers. Ex-post control refers to enterprises' remedy and compensation for pollution. Compared with ex-ante planning, ex-post control is a passive way of management.

(e) Strengthening the tracking and monitoring of the factors affecting the environment in coal enterprises' various production stages.
Coal enterprises should track and monitor the factors that affect the environment in all production stages, especially the quality of the discharged wastes. Enterprises should do their best to meet the discharge standard to avoid unnecessary accidents, losses, or fines.

(f) Establishing an accountability system for environmental protection.
Under the guidance of the scientific outlook on development, a long-term environmental protection accountability system should be established, and environment indicators should be incorporated into the assessment system for leaders. These measures can raise the awareness of enterprises and government leaders on environmental benefits, promote the

renewal and progress of environmental technology and achieve a win-win result of economic and environmental benefits.

(g) Adopting multiple channels to control the cost of environmental governance.
This measure includes the operation of environmental protection facilities, the operation of environmental projects, environmental pollution control and the management of environmental protection affairs. The waste gas, water and residue generated in production, if treated properly, may be changed into treasure, so as to reduce enterprises' costs and increase efficiency; otherwise they will increase the treatment cost. In addition, attention should be paid to environmental regional governance. Centralized sewage disposal should be used to reduce the environmental costs of the various enterprises in certain region.

(h) Strengthening the evaluation and assessment of environmental cost control.
The function of environmental cost control system is to evaluate the effect of environmental factors in enterprise operation. Enterprises cover the environmental costs for obtaining the corresponding environmental benefits, and this is also the motive for enterprises to control environmental costs. The investment of environmental costs can lead to two results: (i) environmental effects. The incurrence of enterprise environmental costs can reduce the emission of wasted pollutants; environmental accidents and potential environmental risks will decrease; staff awareness on environmental protection will be raised and a good corporate image can be established. (ii) Environmental benefits. These include: the reduction of environmental risks, the drop of the level of environmental resource consumption, the benefits from waste reuse, the reduction of expenses on emissions and fines, the rise in sales revenue due to the popularity of environmental protection products, reduction of interest costs thanks to preferential loans, tax reduction and exemption brought by environmental protection products and reuse of "the three kinds of wastes", more vitality in enterprises owing to rising stock prices in the capital market, brisk trade of products in the international market, the increase of trade efficiency and so on.

References

1. Walz, R. Development of environmental indicator systems: experiences from Germany. Environmental Management, **25(6)**, 613-623, (2000)
2. Epstein, M. J. Improving environmental management with full environmental cost accounting. Environmental Quality Management, **6(1)**, 11-22, (1996)
3. Letmathe, P., & Doost, R. K. Environmental cost accounting and auditing. Managerial Auditing Journal, **15(8)**, 424-431, (2000)
4. Russell, W. G., Skalak, S. L., & Miller, G. Environmental cost accounting: The bottom line for environmental quality management. Environmental Quality Management, **3(3)**, 255-268, (1994)

Methodology Development to Locate Hydrogen Stations for the Initial Deployment Stage

Kenshi Itaoka[1,*], *Seiichiro* Kimura[1], and *Katsuhiko* Hirose[1]

[1]Kyushu University, 744 Motooka, Nishi-ku, Fukuoka 819-0395, Japan

Abstract. Hydrogen station deployment needs to be progressed in response to the introduction of fuel cell vehicles (FCVs) to the commercial market. Since resources allocated for deployment are limited for either private companies who wish to install stations and governments who provide subsidies, efficient station allocation should be cognizant of the service of potential customers. Based on a literature review, the results of a social survey and data analysis, p-median is chosen to find optimum locations for hydrogen stations. Location and the amount on potential demand for FCV's in the early stage of deployment is estimated by a regression model. The result of GIS analysis for both 2020 and 2025 using p-median implies the importance of covering regional hub cities (such as prefectural capital cities) as well as metropolises. The coverage rate of potential FCV demand is around 60% at the national level, and exceeds 70 to 80 percent when limited to urban areas for the 400-station allocation. The geographical tendency of station locations allocated by the developed methodology provides guidance for hydrogen station location practice.

1 Introduction

In response to the introduction of fuel cell vehicles (FCVs) in the commercial market in 2015, the development of hydrogen station networks has been progressed in recent years in Japan. The Ministry of Economy, Trade and Industry (METI) issued the Strategic Roadmap for Hydrogen and Fuel Cells in 2014 (revised in 2016) [1] and identified a need for strategic development of hydrogen stations. While the Roadmap did not refer to a specific plan for such development, estimates based on current progress on hydrogen station construction indicate a certain shortage of ST, especially in urban areas.

Installing a hydrogen refueling station is much more expensive than installing a gas station. The initial investment for a hydrogen station is more than 4 hundred million yen. Not only private companies wish to locate hydrogen stations, but also governments provide subsidies to those companies which need to pay a lot of money for hydrogen station deployment. The more hydrogen stations are installed, the more convenient FCV infrastructure will be. However, resources to be allocated to hydrogen station deployment are limited because the business to run a hydrogen station is not profitable in the early stage of FCV deployment and governments have an uncountable number of policies which need to be budgeted. It is thus necessary to allocate stations efficiently to serve potential

* Corresponding author: k.itaoka@i2cner.kyushu-u.ac.jp

customers.

The key objective of this study is to develop a model to allocate hydrogen infrastructure both within and outside of Japan, so as to provide implications for efficient locations of hydrogen stations in the future.

2 Literature on Methods to Allocate Refueling Facilities

A number of studies on the methods to optimally allocate refueling facilities have been conducted since late last century, the majority of which were initiated by researchers in the United States. Established models for refueling-facility location planning can be categorized into the following two major types: (1) location-allocation (LA) solutions; and (2) flow-demand solutions.

The LA theory was originally proposed by Cooper [2] and has been applied to refueling facility planning since late 20th century. An LA problem is to locate a set of new facilities such that the distance from facilities to customers is minimized and an optimal number of facilities is placed in an area of interest while satisfying customer needs. For solving LA problems, numerous algorithms have been designed including *p*-median methods. The *p*-median method aims to find optimum locations of *p* facilities such that the total sum of the distances between each customer (*i*) and the nearest facility (*j*) is minimized. This method is based on the assumption that automotive users prefer to refuel near their home and that a single-purpose trip is made between the customer and the facility to satisfy demand.

This method was applied to some case studies conducted to allocate hydrogen stations in the State of California [3] [4]. It was also used in a series of studies to evaluate scenarios for deploying hydrogen fueled vehicles and supporting infrastructure conducted under the direction of the USA Department of Transport, in response of the requirements of the *Energy Policy Act* 2005 and recommendations made in the report "The Hydrogen Economy (2004)" prepared by the National Academy of Science.

The *p*-median method has also been applied with some modifications. For example, Lin et al. developed the 'fuel-travel-back' approach,' based on *p*-median model, and applied it to derive an optimal station roll-out scheme for Southern California (i.e. to investigate how to effectively locate a limited number of hydrogen stations in an early stage of hydrogen-fueled vehicle market) [5]. The 'fuel travel-back' approach uses nodes weighted by the quantity of fuel consumed on segments "pointing to" demand node (*i*) (instead of population) and with travel time between demand nodes (*i*) and candidate facility locations (*j*) substituted for distance.

All *p*-median based methods share a common feature of relatively simple and limited data requirements. The original *p*-median method requires data on customer locations and road networks only. The aforementioned 'fuel travel-back' approach uses data on spatial distribution of vehicle-miles traveled (instead of population), considering any point along road networks as a possible origin of a refueling trip. When the total travel time is minimized for all fuel (in gallon-minutes), the average refueling travel time is theoretically considered to be minimized.

The other type of solution, flow-demand solutions, analyzes refueling demands based on traffic flows. Hodgson argued that for many types of facilities, such as refueling facilities, convenience stores, automated teller machines, traffic flows exert a demand [6]. The unit of demand to be covered is, therefore, the path from an origin to a destination rather than considering demand as a set of nodes. This means that refueling should be assumed often as a secondary purpose of travel: customers tend to refuel on the way to somewhere else rather than making a single purpose trip solely to refuel their vehicles. Flow-demand solutions were considered to provide a behaviorally more realistic basis for

locating refueling facilities.

There are several methods developed to solve flow-demand problems. They can be classified into three methods: Traffic count method; Flow-Capturing Location Model (FCLM) or Flow Intercepting Location Model (FILM); and Flow Refueling Location Model (FRLM).

The traffic count method is to locate stations on high-traffic routes or within high-traffic areas. For example, roads with more than certain traffic volume (e.g. ≥ 20,000 traffic volume per day) are chosen to locate refueling facilities [7]. When refueling facilities are to be located in high-traffic areas, the total sum of vehicle kilometers traveled is calculated for each area unit and refueling facilities are located where a certain level of vehicle kilometers traveled is achieved [8]. This method is relatively simple yet has some shortfalls such as the double-counting issue. It is possible to count the same trips by the same drivers more than once if the trip travels multiple links, even though drivers might refuel only once, thus resulting in concentrating refueling facilities on several adjacent links of a high-volume major route (e.g. freeway).

Flow capturing methods such as FILM or FCLM were developed to avoid such double counting issues. FILM/FCLM locates a given number (p) of refueling facilities so as to maximize the total possible flows that are intercepted during their travel. Basic units of demand are flows on paths across a transportation network and the flows over the network arcs are explicitly considered. Flows are captured by various methods: some studies consider a refueling facility captures a flow only when the facility is directly on the path of the flow while others consider trips are captured by the facility even when these trips require minor detours to get to the facility. FILM/FCLM tends to capture more origin-destination (OD) flows on the shortest paths between OD pairs, however, for longer inter-city trips, one refueling facility anywhere along the path may not be enough to enable a vehicle with a limited driving range to complete the trip without running out of fuel.

Lim and Kuby further advanced FILM/FCLM to FRLM to maximize the number of trips that can potentially be refueled by p refueling facilities. Unlike FILM/FCLM, OD flows are covered by a combination of facilities rather than individual facilities [9]. FRLM counts a flow as refueled only if a combination of stations exists on a path that can successfully refuel the round trip between the origin and destination. At the metropolitan scale, if no round trips are longer than the assumed vehicle driving range, the FRLM reduces to the FILM/FCLM.

All FILM/FCLM/FRLM requires, in general, a matrix of OD flows, each of which must then be assigned to a particular likely path through the network. Such data are hard to work with and are not always available for all regions or scales required for analysis. Further, there are infinite number of OD pairs in reality, thus only simplified OD matrixes can be used.

3 Analytical Method

3.1 Targeting potential FCV customers

According to the diffusion of innovation theory proposed by Rogers [10], proactive adopters of any new innovations or ideas, who are categorized as “Innovators,” appear at early stages of the diffusion. His theory presented that a key to successful new market development is to approach Innovators. We do not discuss whether Rogers’ diffusion of innovation theory is applicable to FCVs in this paper, however it can be assumed that early customers of FCVs are not likely to be general citizens. It is thus critical to identify the features and locations of the Innovators in the FCV market.

The revised Strategic Roadmap for Hydrogen and Fuel Cells [1] set targets for the dissemination of FCVs as follows: approximately 40,000, 200,000 and 800,000 vehicles by 2020, 2025 and 2030, respectively. This means that the main FCV customer segments are still likely to be Innovators or Early Adaptors even around 2025, therefore a targeting approach will be required for successful dissemination.

An obvious feature of FCV in the commercial market is its price. The price of FCV is more than five (5) million Japanese yen before 2020 even with government subsidies. This price level is expected to be similar until 2020. Except for the driving components and fuel of the FCV, the new FCVs introduced in the market belong to the category of traditional luxury passenger cars. We consider potential customers, Innovators or Early Adaptors for FCV, are a part of luxury passenger car customers. For 2025, middle-class automotive buyers were assumed to be FCV potential buyers as the cost reduction of FCV car to around three (3) million yen; the same price level of popular hybrid cars such as the Prius, as expected according to communication with automobile companies.

3.2 Optimization method of location allocation of hydrogen stations

3.2.1 Reasoning of methodology choice

Our study team conducted a survey research on the daily refueling behaviors of existing automotive users in March 2016 (N=3,790). Respondents are randomly chosen from an Internet panel representing the general public who have a driver's license. The survey result shows that 71% of the respondents use refueling stations near their home while the remaining respondents prefer refueling stations along or near the routes between their home and their key driving destinations such as work places or shopping centers (Figure 1). The survey also asked travel time to the refueling stations usually used for respondents. The respondents showed the tendency to use five minutes intervals for their answer but we can see a rough tendency of proximity to the preferred refueling stations. The mean and the mode travel time to the refueling stations usually used for respondents are 9.5 minutes and five minutes, respectively (Figure 2). It should also be noted that more than 20% respondents travel over 15 minutes.

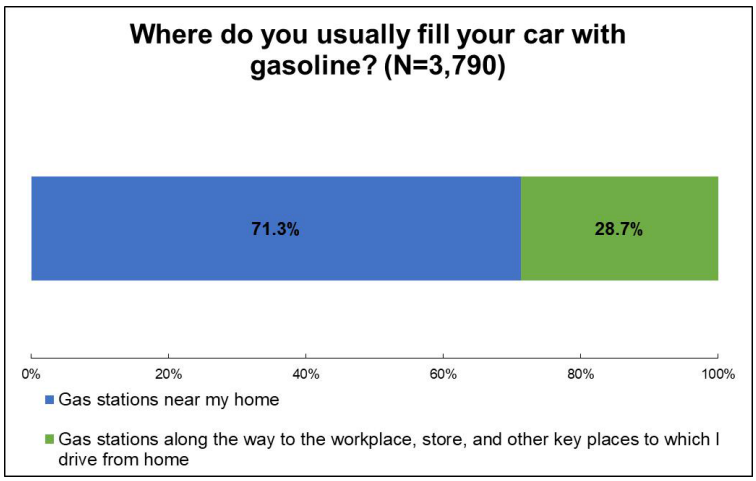

Fig. 1. Locations of gas stations where customers usually refuel

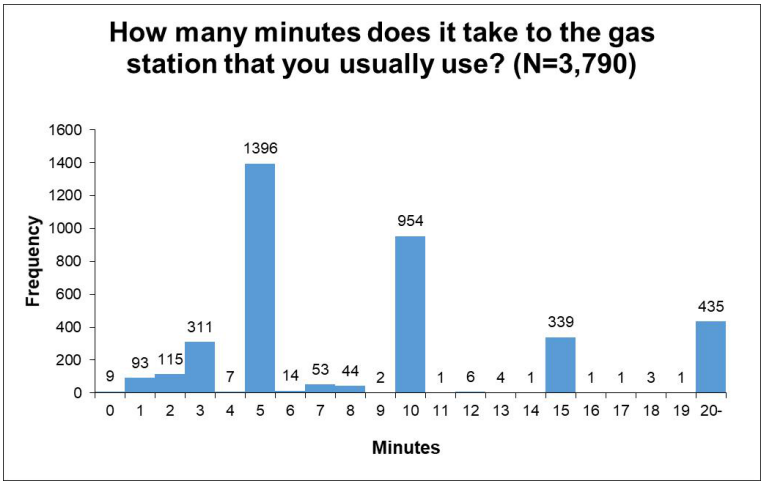

Fig. 2. Time spent at gas stations where customers usually refuel

3.2.2 Choice of optimization method of location allocation of hydrogen stations

We decided not to use the flow-demand solution model but P-median for optimizing geological locations of future hydrogen stations for the following reasons:

- The majority of current car users refuel their cars near their residence or office and the majority of trips users make are short distance. These imply proximity to stations is important for station location allocation, although car users do not necessarily show a strong priority toward proximity.
- The required level of geological resolution for station location cannot be obtained by flow-demand solution models but by P-median model. Only simplified OD matrixes such as intercity level OD matrixes are available for conducting flow capturing analyses. This means flow-demand solutions using such OD matrixes do not provide detailed locations within a city, yet the largest portion of car trips happen within cities in Japan.

Meanwhile, we realize that flow-demand solution models need to be used as a supplementary approach for determining the station locations to cater for mid-to-long distance trips.

3.3 Location estimation of potential customers of FCV

In order to identify the location and quantity of potential FCV customers with reasonable geographical resolution which is a 1km square grid, car sales data at the municipal level was used to conduct regression analyses.

Stepwise regression analysis was carried out, using the data of luxury car sales at the municipal level as a dependent variable and variables of general statistics including more than fifty candidate variables as independent variables, giving consideration to multi-collinearity. The regression model should not use intercept in the equation because an existence of intercept in the model equation means the existence of some amount of potential customers automatically in every 1km grid. The model fit and regression coefficients of the luxury car regression model are presented in Table 1 and Table 2, respectively.

The adjusted R-Square of 0.909 indicates a good model fit for the chosen regression

model (see Table 1). The stepwise regression process finally leaves two explanatory variables, number of employees and total consumer spending. The variable of number of employees that is the sum of the number of people employed in the area is considered to represent demand of corporate customers and the total consumer spending is considered to represent the demand of private customers. The standardized coefficients of explanatory variables, which is 0.625 for the number of employees and 0.374 for the total consumer spending (see Table 4), indicate the corporate demand explained more than 60% to the total luxury car demand reflecting real luxury car sales statics.

Table 1. Model fit of the luxury vehicle regression model

R	R Square*	Adjusted R Square	Std. Error of the Estimate
.953	.909	.908	16.790

Note: * For regression through the origin (models without an intercept), R-squared measures the proportion of variability in the dependent variable regarding the origin explained by regression

Table 2. Regression coefficients of the luxury vehicle regression model

	Unstandardized Coefficients		Standardized Coefficients		
	B	Std. Error	Beta	t	Sig.
Employees	.0004	.000	.625	44.360	.000
Total consumer spending	1.206E-07	.000	.374	26.559	.000

Similarly, a stepwise regression analysis was conducted using the car sales data at municipal level as well as general statistics, to estimate middle-class automotive demands in three dimensional geometry. The dependent valuable used in the calculation is the sales data of automobiles in the middle-class and higher price range. The model fit and regression coefficients of the middle-class automobile regression model are presented in Table 3 and Table 4, respectively.

As presented in Table 3, the adjusted R-Square is 0.935, i.e. the model fit is high. The independent variables that stepwise regression process decide in this model are the number of workers and number of employees. The number of workers that means the sum of the number people engaged in work in households within the area is considered to represent the volume of the private customer demand while the number of employees is considered to represent the demand of business customers (see Table 4). Although potential buyers of middle-class automobiles include corporate customers, private customers are the majority, which is reflected in the standardized coefficients and thus in the modelling result. For the luxury car market model, the coefficient of expenditures (i.e. income) explained the demand of private customers. However, the number of workers rather than expenditure can explain the demand of private customers in the middle-class automobile market model.

Table 3. Model fit of the mid-range vehicles (automobiles priced above the mid-range) regression model

R	R Square*	Adjusted R Square	Std. Error of the Estimate
.967	.935	.935	218.090

Note: * For regression through the origin (models without an intercept), R-squared measures the proportion of variability in the dependent variable regarding the origin explained by regression

Table 4. Regression coefficients of the mid-range vehicles (automobiles priced above the mid-range) regression model

	Unstandardized Coefficients		Standardized Coefficients		
	B	Std. Error	Beta	t	Sig.
Workers	.0118	.000	.903	81.611	.000
Employees	.0008	.000	.080	7.241	.000

3.4 Application of P-median to location allocation of hydrogen stations

The p-median problem is a type of discrete location model which places "p" facilities in a manner to minimize the sum of the demand-weighted distance between a demand node and the closest facility. In this study, we aimed to optimize the facility locations, when placing a given number of hydrogen stations (ST) within a defined area, by minimizing the total travel time cost (i.e. the sum of the potential demand node multiplied by time distance). The algorithm of the calculation is presented below:

The total distances between all users and the closest ST (r_{ij}), is expressed in the following equation:

$$r_{ij} = f(x_i,\ y_i)d_{ij} \tag{1}$$

where:
$a_i(x_i,\ y_i)$: a given demand node
$f(x_i,\ y_i)$: location of a user
d_{ij} : distance between a user $f(x_i,\ y_i)$ and the closest ST (s_j)

The distance (t_j) between a given ST (s_j) and demand nodes (1, 2, ⋯, j, ⋯、 m) within the ST's coverage is then calculated using Equation 2:

$$t_j = \sum_{i=1}^{m} r_{ij} = \sum_{i=1}^{m} f(x_i,\ y_i)d_{ij} \tag{2}$$

Therefore, When the number of ST to be placed is "N," the sum ($\boldsymbol{T_{total}}$) of the distances between demand nodes and the closest STs
When the total number of ST users in all defined areas are set as N_h, the average distance to the closest ST is expressed in Equation 3:

$$T_{avg} = \frac{1}{N_h} T_{total} = \frac{1}{N_h} \sum_{j=1}^{N} \sum_{i=1}^{m} f(x_i,\ y_i)d_{ij} \tag{3}$$

The objective function is set to minimize the average travel distance (T_{avg}). Equation 4 is then used to identify a ST location (s_j):

$$T_{avg}^{min} = \min_{S} \frac{1}{N_h} \sum_{j=1}^{N} \sum_{i=1}^{m} f(x_i,\ y_i)d_{ij} \tag{4}$$

As N_h is a constant factor, Equation 4 can be simplified as Equation (5):

$$T_{avg}^{min} = \min_{S} \sum_{j=1}^{N} \sum_{i=1}^{m} f(x_i,\ y_i) d_{ij} \quad (5)$$

In this model, existing STs are treated as mandatory locations, thus the number of existing ST locations ($O = \{o_k | k = 1, 2, \cdots, O\}$) is deducted from the total number of candidate ST location ($P = \{p_i |\ i = 1, 2, \cdots, L\}$) prior to running the model. Then, the calculation using Equation (3) was repeated for all possible sets of N in order to determine the optimum locations of new STs. This method is a combinational optimization procedure where N is selected from L-O. It is impossible to validate all possible combinations in reality as the number of possible combinations is massive. Therefore, we applied heuristics to this model in order to identify a result close enough to the optimum value and used three methods, randomized greedy algorithms [11]; vertex substitution heuristic [12]; and path relinking method [13]. Combinations of several heuristics are applied to enhance the solution accuracy. The optimum solution applying heuristics was calculated in the following procedures:

Step 1: Calculate the initial solution using randomized greedy algorithms, by which the initial solution is semi-randomized.
Step 2: Calculate a second solution applying the solution set obtained by Step 1 to vertex substitution heuristic.
Step 3: Calculate another second solution applying the solution set obtained by Step 1 except for solution set obtained by Step 2 to path relinking meta heuristics.
Step 4: Choose a more suitable solution between the two solutions identified through Steps 2 and 3.
Step 5: Repeat Steps 1 to 4 in a given number then choose the best optimal answer within identified candidate locations.

4 Analyses and discussion

4.1 Locating hydrogen stations for 2020 and 2025

The price of FVCs is likely to maintain the 2016 level until the mid-2020's although a gradual fall is anticipated in the future. As mentioned in Section 1.1, METI's Strategic Roadmap for Hydrogen and Fuel Cells estimated the number of hydrogen refueling stations in Japan to be 160 in 2020 and not to exceed 200 in the next five years. Therefore, the key FCV purchasers in 2020 are assumed to be potential luxury car buyer groups and the number of hydrogen station to be 200 in order to analyze the optimum facility locations using p-median problem.

The FCV price is expected to be lower to around three million yen by 2025 while the number of hydrogen station to increase to 320, according to the METI Roadmap. Regarding the station location analysis for 2025, the FVC purchaser group is thus assumed to be potential middle-class automobile buyer groups and the number of hydrogen station to be 400. As 92 stations are already at either the design, construction or operational stages as of the end of August 2016, the p-median analysis was conducted for the remaining 108 or 308 stations. The coverage of each station is set to be 15 minutes driving distance in rush hours for coverage analyses in the later section. The results of the optimum placement analyses are shown in Figures 3 to 7.

The results for both 2020 and 2025 indicate that hydrogen stations should be spread across the country to capture potential FCV customers effectively and to promote FCVs. Figures 3 illustrates that 94 percent prefectural capital cities are covered by the placement

of the 200-station by 2020 and fully covered by the 400-station allocation of 2025. This result identified the importance of covering regional hub cities (such as prefectural capital cities) as well as metropolises such as Tokyo, Nagoya and Osaka for capturing more potential FCV customers.

Furthermore, the results for 2020 indicated that 43 out of 108 new stations are to be placed outside of four (4) major metropolitan areas (i.e. Tokyo, Kanagawa, Saitama, Chiba, Osaka, Kyoto, Hyogo, Aichi and Fukuoka). As 19 of the exiting 92 stations have been placed outside of the four (4) metropolitan areas, approximately 30 percent of the total 200 stations need to be located outside of the metropolitan areas in order to capture more potential luxury car buyers. Likewise, 163 out of 308 new stations to be built by 2025 needs to be placed in the areas other than the metropolitan areas to optimize the capture of potential middle-class automotive purchasers. This means approximately over 40% of the total 400 stations needs to be placed outside of the four metropolitan areas to optimize the potential of FCV dissemination.

Figures 3 to 7 show that most of the 200 hydrogen stations are allocated to the central urban areas and other densely populated areas within the four major metropolitan areas and not many are placed in the corridors between those cities. However, the development of hydrogen stations in such gap areas is likely to be progressed during the 400-station placement. In other words, populated areas should be covered first to maximize capture of demand when the hydrogen station number is limited to 200. The corridors between major cities and the regional centers are recommended to be covered when the station number is increased to 400.

In reality, extra 200 stations will be added after completing the development of the first 200 stations when 400 stations are determined to be constructed in total. This study assumed different FCV prices, thus different target buyers (i.e. potential luxury car buyers for the allocation of 200 stations and potential middle-class vehicle buyers for 400 stations), for nominated years. Therefore, it is possible that some of the facility locations identified through the 200 station allocation analysis might not be identified in the 400 station allocation analysis. However, the result indicates no municipality where stations identified in the allocation of 200 stations are eliminated in the 400 station allocation.

The analysis results highlighted the importance of placing hydrogen stations in regional hub cities at a relatively early stage. It has also been confirmed that the hydrogen stations allocated to capture the needs of luxury car purchasers are unlikely to be redundant when the market is expanded to include middle-class automobile purchasers.

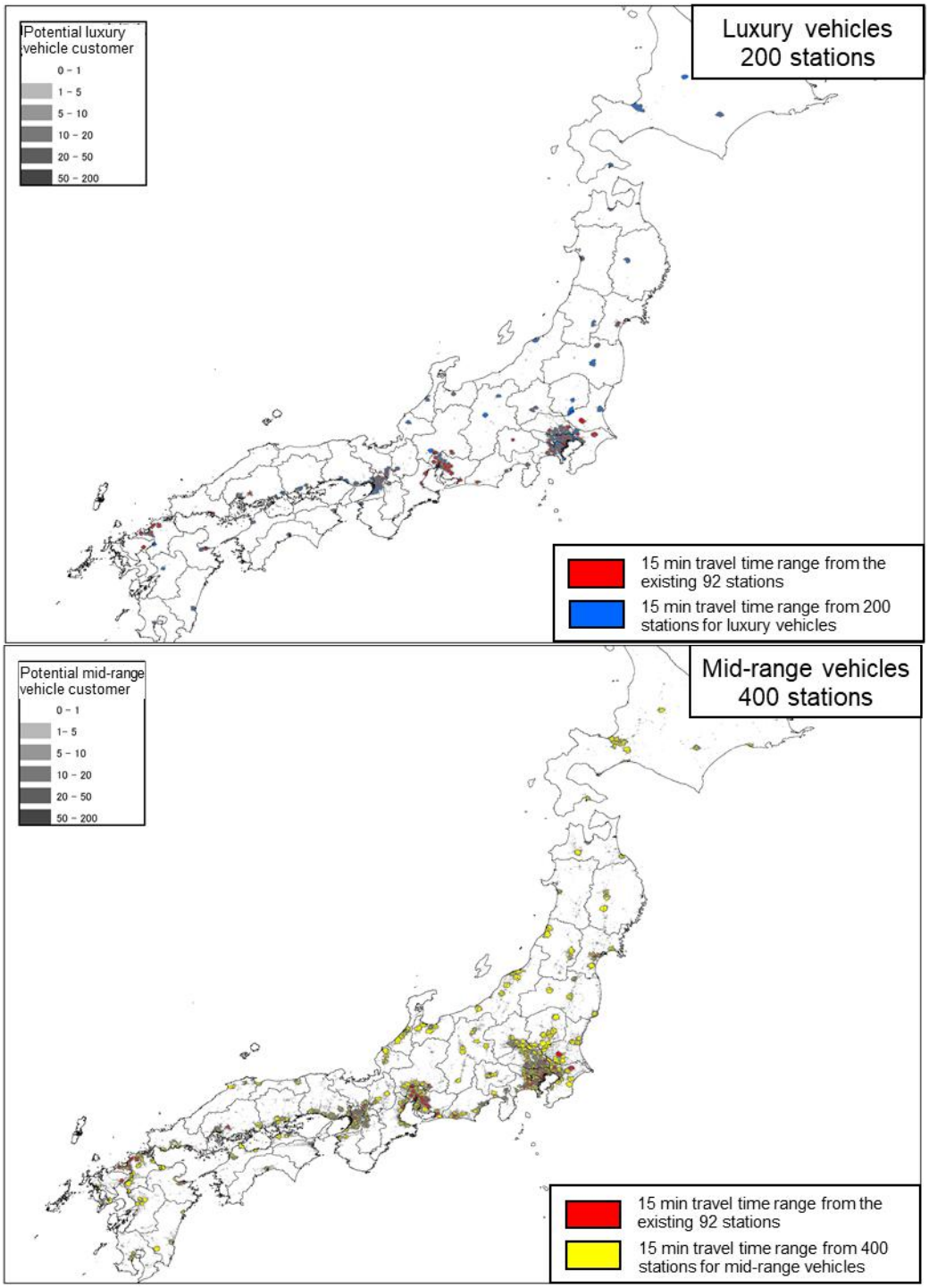

Fig. 3. Nationwide placement of 200 hydrogen refueling stations (top), 400 stations (below) (15-minute travel time range from the hydrogen refueling station shown)

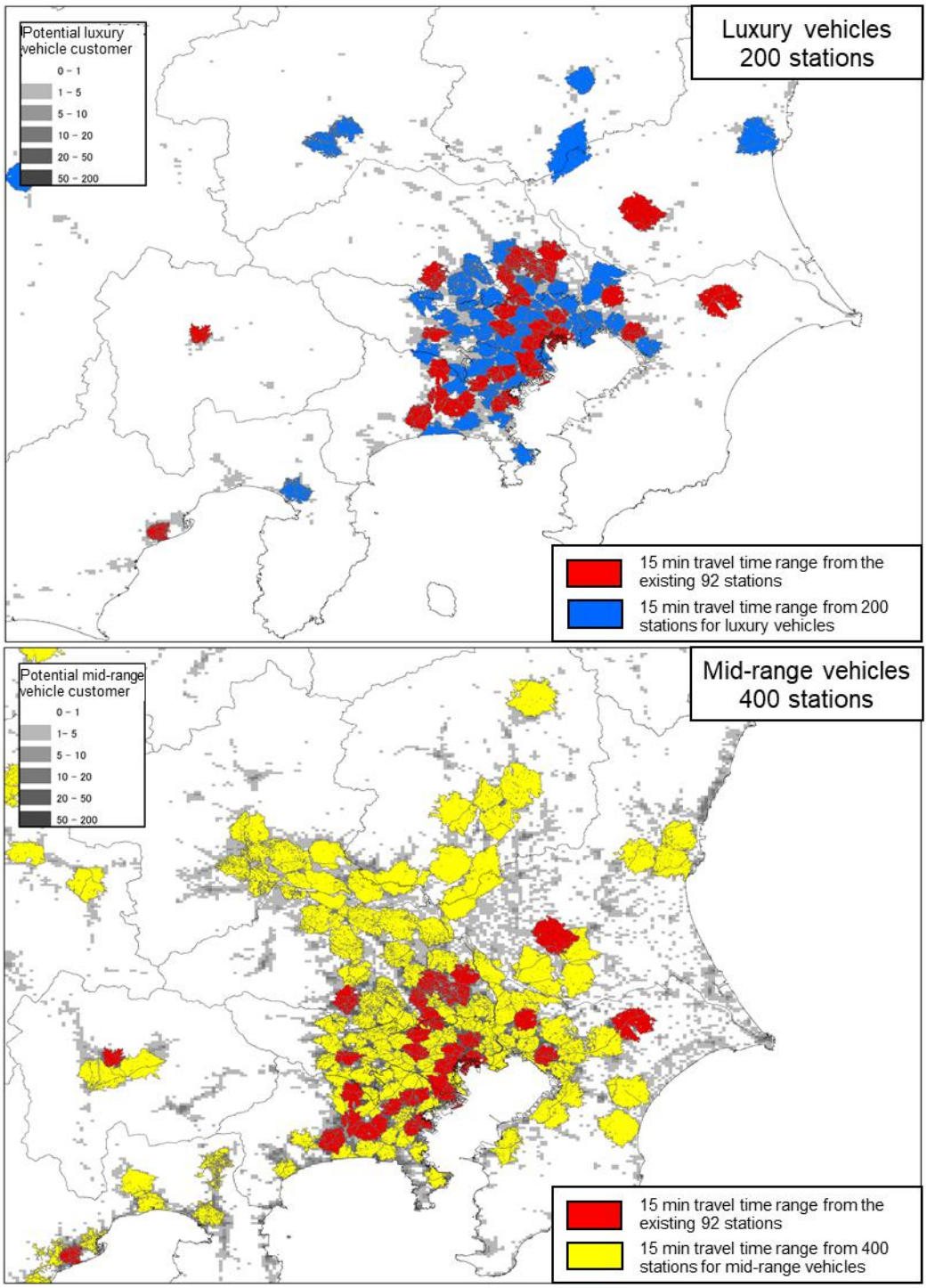

Fig. 4. Placement of 200 hydrogen refueling stations (top), 400 stations (below) in the Greater Tokyo area (15-minute travel time range from the hydrogen refueling station shown)

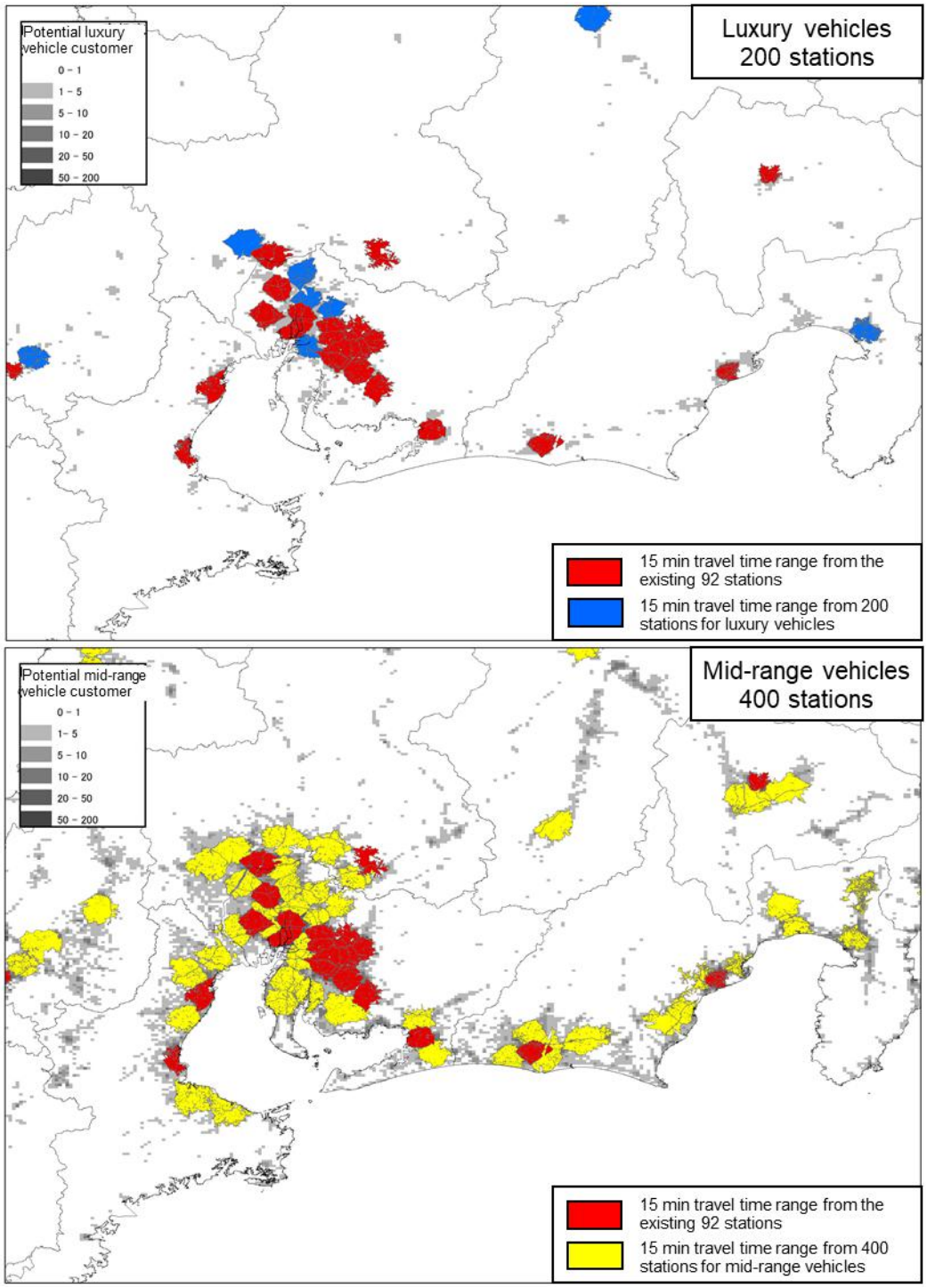

Fig. 5. Placement of 200 hydrogen refueling stations (top), 400 stations (below) in the Chukyo Metropolitan area (15-minute travel time range from the hydrogen refueling station shown)

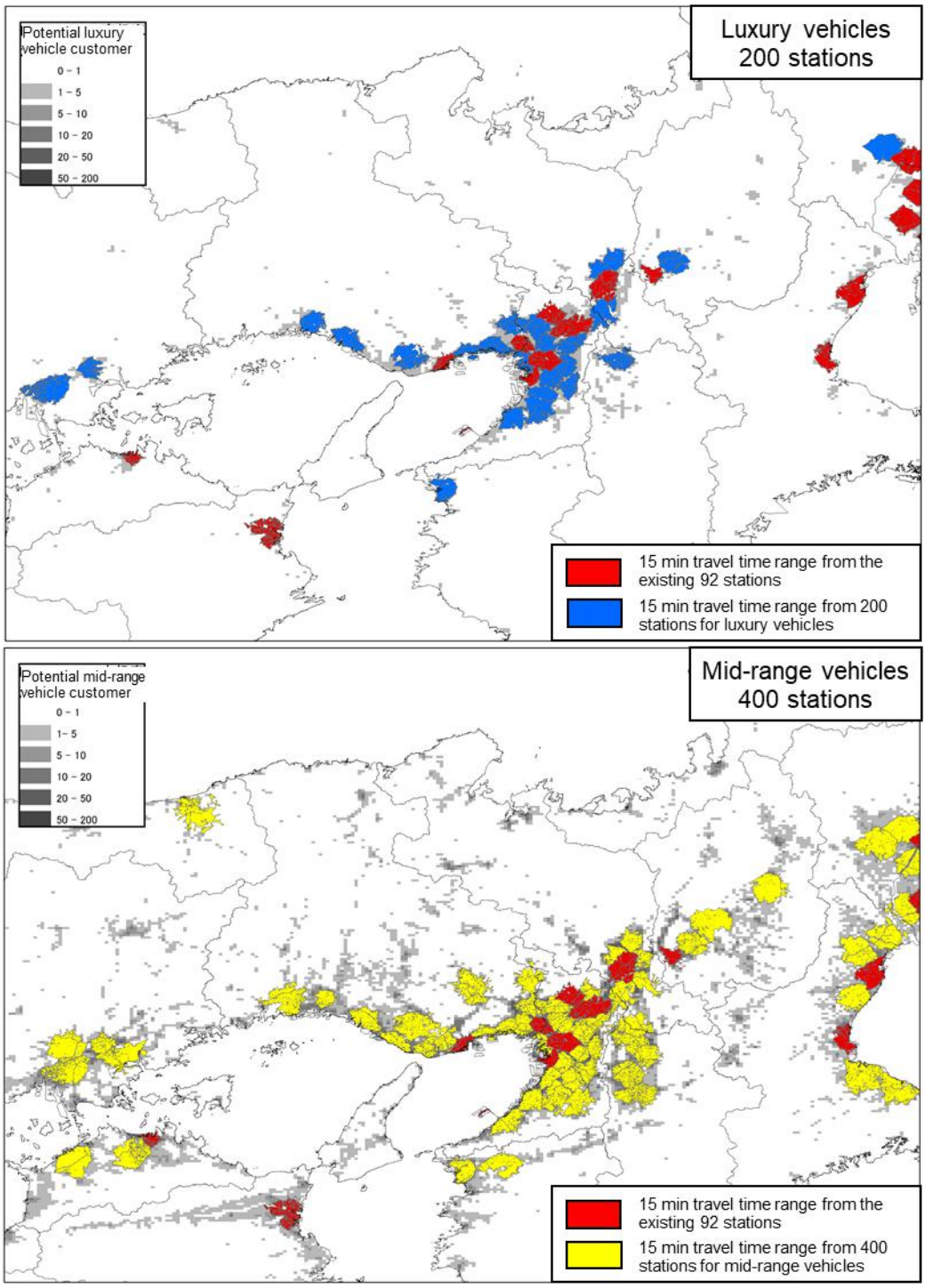

Fig. 6. Placement of 200 hydrogen refueling stations (top), 400 stations (below) in the Keihanshin Metropolitan area (15-minute travel time range from the hydrogen refueling station shown)

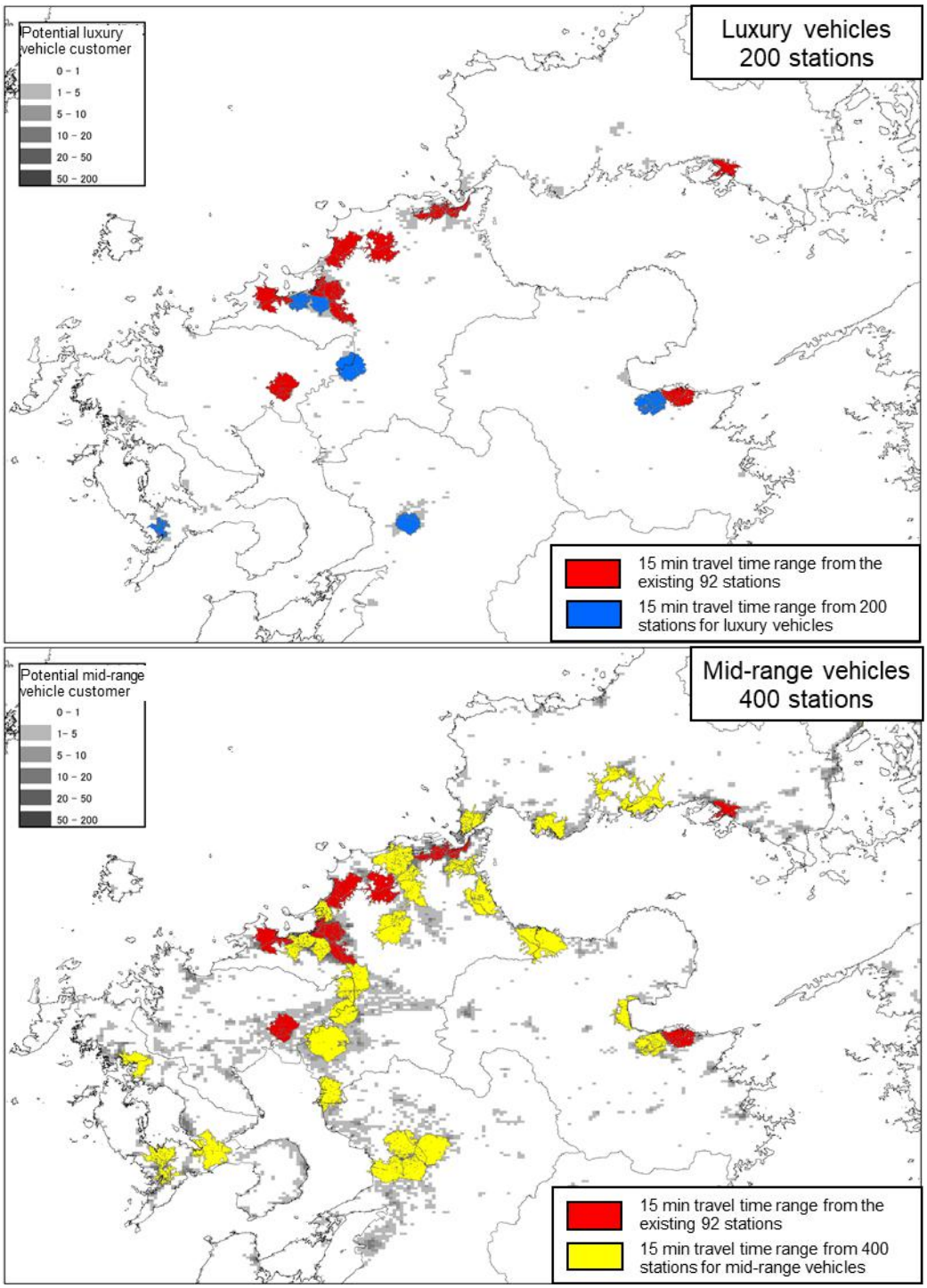

Fig. 7. Placement of 200 hydrogen refueling stations (top), 400 stations (below) in the Fukuoka Metropolitan area (15-minute travel time radius from the hydrogen refueling station shown)

4.2 Coverage of potential customers as a result of location allocation

The objective of p-median is not to maximize the coverage of potential customers but to minimize the sum of weighted distance from potential customers to the stations being located. However, the coverage of potential demands and population are often discussed in locating hydrogen stations. The coverage of potential demands is thus also investigated in this study. The coverage was defined as the percentage of potential FCV buyers located within 15 minutes driving rage from any of the identified hydrogen stations. 15 minutes seems the longest distance that at least some portion of people can accept according to the social survey. As previously mentioned in Section 1.2.1, it is ideal that identified stations are located in areas convenient for individual users. As a reference, 85% of residences in Japan are located within three (3) minutes driving distance from the closest petrol station while 90%, 95% and 99% of them are located within 4-min, 5-min, 10-min driving distance [14]. P-median analyses were conducted to calculate the coverages of 1) potential luxury car buyers; 2) middle-class vehicle buyers; 3) the entire population; and 4) registered vehicles, for each of the100, 200, 300 and 400 station allocations (including the 92 existing stations). The results are presented in Figures 8 to 12. In this calculation, the following definitions were applied:

The result indicated that the rate of increase in potential demand coverage became smaller for both the potential luxury car buyers and middle-class vehicle buyers as the number of hydrogen station increased in urban areas. This tendency is especially obvious in the Tokyo Metropolitan Area and for potential middle-class vehicle buyers. This is because p-median location problems tend to prefer locating facilities in regional centers rather than suburbs surrounding metropolitan areas to increase the demand coverage more effectively. While the coverage rate of the potential FCV demand is around 60% at the national level, it exceeds 70 to 80 percent when limited to urban areas for the 400 station allocation. Preference is thus likely to be given to urban areas in hydrogen facility placement.

The coverage of potential luxury vehicle buyers is about five to ten percent higher than the population coverage both nationwide and in all four metropolitan areas. On the other hand, the coverage of potential middle-class vehicle buyers is similar to the population coverage. This is due to the distribution of potential middle-class vehicle buyers which is approximately the same as the population distribution in Japan. However, the number of vehicles owned per person increases in rural areas in general. The coverage of registered vehicles is thus lower than the population coverage when more hydrogen stations are to be deployed in urban areas at an early stage. Yet, those coverages are similar in the Chukyo Metropolitan Area and the Fukuoka Metropolitan Area where the population distributions overlap with the distribution of registered vehicles. Therefore, more hydrogen stations will be required in suburbia of urban areas where vehicle holding ratios tend to be low, if the facility locations are determined based on the existing registered vehicle distribution. With regard to regional cities and other rural areas, most of the demand is likely to be covered by targeting potential middle-class vehicle buyers, as the distributions of population, registered vehicles and potential middle-class vehicle buyers are also similar in those areas.

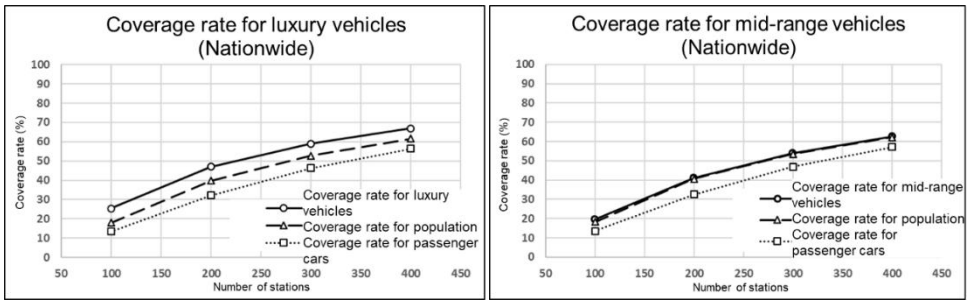

Fig. 8. National hydrogen refueling station potential coverage rate for luxury vehicles (left) and mid-range vehicles (right) (15-minute distance to hydrogen refueling station)

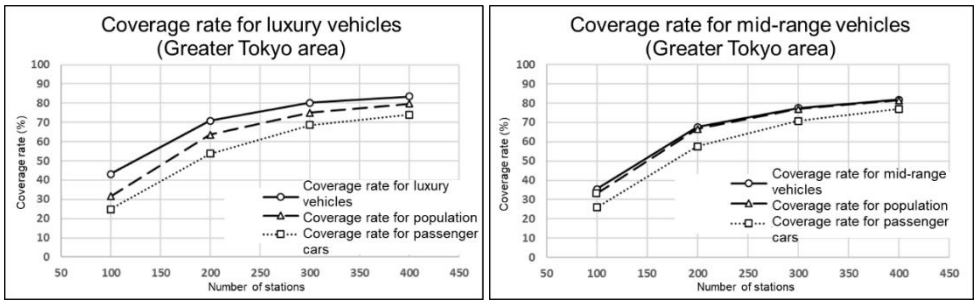

Fig. 9. Hydrogen refueling station potential coverage rate for luxury vehicles (left) and mid-range vehicles (right) in the Greater Tokyo area (15-minute distance to hydrogen refueling station)

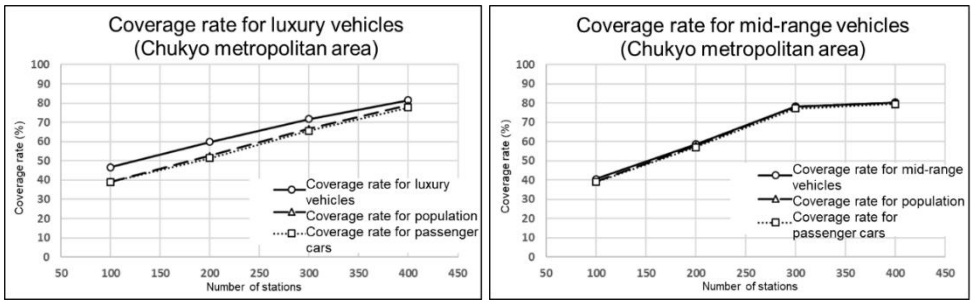

Fig. 10. Hydrogen refueling station potential coverage rate for luxury vehicles (left) and mid-range vehicles (right) in the Chukyo metropolitan area (15-minute distance to hydrogen refueling station)

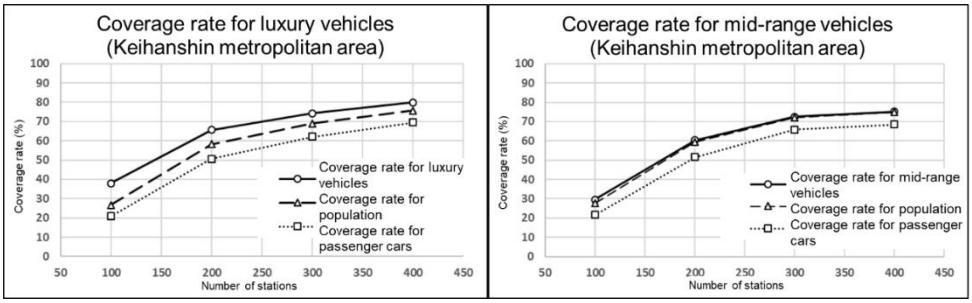

Fig. 11. Hydrogen refueling station potential coverage rate for luxury vehicles (left) and mid-range vehicles (right) in the Keihanshin metropolitan area (15-minute distance to hydrogen refueling station)

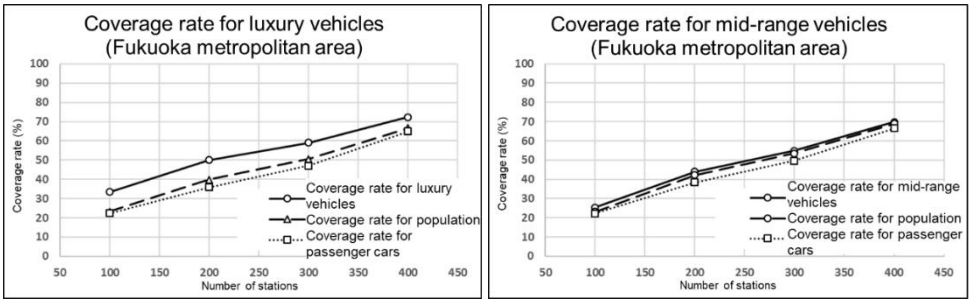

Fig. 12. Hydrogen refueling station potential coverage rate for luxury vehicles (left) and mid-range vehicles (right) in the Fukuoka metropolitan area (15-minute distance to hydrogen refueling station)

5 Conclusion

Hydrogen station deployment needs to be progressed in response to the introduction of fuel cell vehicles (FCVs) in the commercial market. Since resources allocated to deployment are limited for either private companies who wish to install stations and governments, efficient station allocation should be cognizant of serving potential customers. Based on literature review, results of a social survey and data analysis, p-median is chosen to find the optimum locations of hydrogen stations. Location and amount of potential demand of FCV's in the early stage of deployment is estimated by a regression model. The results of GIS analysis using p-median for both 2020 and 2025 indicated that hydrogen stations should be spread across the country to capture potential FCV customers effectively and to promote FCV deployment. The map resulting from the GIS analysis shows 94 percent prefectural capital cities are covered by the placement of the 200-stations by 2020 and fully covered by the 400-station allocation of 2025, implying the importance of covering regional hub cities (such as prefectural capital cities) as well as metropolises. The coverage rate of the potential FCV demand is around 60% at the national level, it exceeds 70 to 80 percent when limited to urban areas for the 400 station allocation. The geographical tendency of station locations allocated by the developed methodology provides a guide for location of hydrogen stations.

References

1. Council for a Strategy for Hydrogen and Fuel Cells, Revised Version of the Strategic Roadmap for Hydrogen and Fuel Cells [cited 2016 December 22]. Available from: http://www.meti.go.jp/press/2015/03/20160322009/20160322009-c.pdf (2016)
2. L. Cooper, Oper. Res. **11**, 331-343 (1963)
3. M. A. Nicholas, S. L. Handy, D. Sperling, Transp. Res. Rec. **1880**, 126-134 (2004)
4. M. A. Nicholas, J. Ogden, Transp. Res. Rec. **1983**, 121-128 (2006)
5. Z. Lin, J. Ogden, Y. Fan, C. Chen, Int. J. Hydrogen. Energy. **33**, 3096-3101 (2008)
6. M. J. Hodgson, Geogr. Anal. **22**, 270-279 (1990)
7. M. Melendez, A. Milbrandt, Paper presented at the National Hydrogen Association Annual Hydrogen Conference 2005, Washington, D.C., the United States (2005)
8. M. A. Nicholas, J. Transp. Geogr. **18**, 738-749 (2010)
9. S. Lim, M. Kuby, Eur. J. Oper. Res. **204**, 51-61 (2010)
10. E. M. Rogers, *Diffusion of innovations, 5th edition* (Free Press, New York, 2003)
11. T. A. Feo, M. G. Resende, J. Glob. Optim. **6**, 109-133 (1995)
12. M. B. Teitz, P. Bart, Oper. Res. **16**, 955-961 (1968)
13. M. Boudia, M. A. O. Louly, C. Prins, Comput. Oper. Res. **34**, 3402-3419 (2007)
14. S. Kimura, Kyushu university doctor thesis (2010)

Experimental Study on the Treatment of 1, 4 butanediol Mixed Wastewater by Ferro-carbon Micro-electrolysis

Jie Lei [1,*], *Xiaodong* Zhang [2] , *zhenglin* Zhou [3], *Shaohui* Fan [4], *Bo* Jiang [5], *Xianlan* Tian [6]
Xi 'an, 727400, China

Abstract. The mixed wastewater of 1, 4 butanediol was tested with iron filings and carbon powder as catalyst by aeration to provide oxygen. The effects of carbon powder, pH value and reaction time on wastewater treatment were studied. The optimal experimental condition was that the mesh number of activated carbons was 20, the pH value was 5, the reaction time was 30min, and the Chemical Oxygen Demand （COD） removal efficiency reached 36.2%. At the same time, The response surface method was used to analyze and optimize the experimental results, and the relation formula of each influencing factor on removal efficiency was established, and the order of influence degree of each factor on removal efficiency (pH> activated carbon mesh number > reaction time) was obtained, in which pH had the greatest influence on the treatment rate of ferro-carbon micro-electrolysis treatment of 1, 4-butanediol wastewater.

1 Introduction

1, 4 butanediol is an important organic chemical raw material, which is widely used in pharmaceutical chemical textile paper cars and daily chemical industry [5]. At present, the commonly used production technology is alkyl aldehyde method, and the products are 1,4-butanediol (THF), 1,4butyne glycol (BYD), polytetrahydrofuran (PTMEG) etc. THF and PTMEG is a kind of toxic organic compounds, from structural analysis belongs to refractory material, is great harm to human health [1] [2].

Ferro-carbon micro-electrolysis used the metal corrosion principle method to conduct electrolytic treatment of the waste water, by using the self-generated 1.2V potential difference of the micro-electrolytic material filled in the waste water without power, and achieve the purpose of degrading organic pollutants. Under acidic conditions, it is conducive to the micro-electrolysis reaction, which can speed up the reaction rate. The oxidation reduction reaction of dissolved oxygen and Fe^{2+} in wastewater will destroy the molecular structure of some organic substances. The Fe^{3+} will flocculate the organic substances in waste water and further remove the pollutants [3]. Activated carbon surface contains a large number of acidic or alkaline groups, which have adsorption capacity and

* Corresponding author: epleijie@aliyun.com

catalytic effect. When there is O_2 or hydrogen peroxide （H_2O_2） in wastewater, the pollutants in wastewater are catalyzed and oxidized [4].

In this study, 1, 4 butanediol mixed wastewater was taken as the research object, air was taken as the oxidant, and the effects factors such as pH, reaction time and activated carbon mesh number were studied. The experimental results indicated that the activated carbon mesh number was 20, pH value was 5, reaction time was 30min, and the COD removal efficiency reached 36.2%, which provided the fundamental researches for the Ferro-carbon micro-electrolytic treatment technology of 1, 4-butanediol mixed wastewater. Response Surface Methodology (RSM) was used to analyze and optimize the experimental results, and a quadratic polynomial mathematical model was established for the relationship between COD removal efficiency and various factors, and effect of the different factors on COD removal efficiency was analyzed.

2 Materials and methods

2.1 Materials

The wastewater comes from BDO and PTMEG production workshops of a chemical enterprise in China. The wastewater quality was as follows: COD 6000~12000 mg L^{-1}, biochemical oxygen demand（BOD_5） 596~1800 mg L^{-1}, B/C 0.083~0.11, pH 6~9, salt concentration 0.06 wt%. The main effluent discharge and pollutant concentration are shown in Table 1.

Table 1. Sewage discharge and pollution characteristics of a chemical enterprise in northwest china.

No	Parameter	Flow / m^3 h^{-1}	Concentration / mg L^{-1}	Toxicity	Biodegradation	Pretreatment
1	BDO	20	1800	N	Easy	N
2	BYD	15	200	N	Difficult	Y
3	HCHO	10	3600	Y	Bacteriostatic	Y
4	PT/THF	8	3700	Y	Bacteriostatic	Y

2.2 Test instrument

The test instruments mainly include a small Ferro-carbon reactor and pH meter and COD meter and etc.

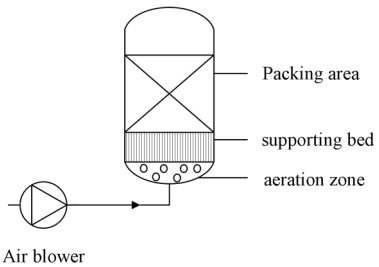

Fig. 1. Structure of the Ferro-carbon reactor

2.3 Methods

(1) Rinse the activated carbon with clean water before use, soak it in the waste water, and dry it.
(2) Put the activated carbon and iron shavings in a self-made aeration device, which is full of waste water, then in the reaction.
(3) Adjust the pH of the reaction wastewater to pH near neutrally, and test the COD of the supernatant after filtration.

3 Results and Discussion

3.1 Results

3.1.1 Effect of activated carbon mesh number on COD removal efficiency

When the Fe-C mass ratio was 1:1, the pH was 4 and the reaction time was 50 min, changed the mesh number of activated carbons, the removal efficiency of COD in wastewater after the reaction was shown in Table 2.

Table 2. Influence of activated carbon mesh number on COD removal efficiency

Activated carbon mesh	8	15	20	30
Removal efficiency /%	20.8	24.4	34.8	23.9

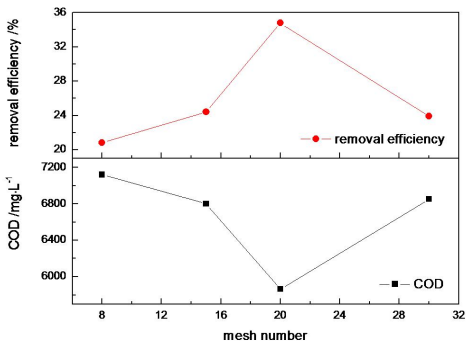

Fig. 2. Influence of activated carbon number on COD removal efficiency

3.1.2 Effect of pH on COD removal efficiency

As shown in Table 3, when the Fe-C mass ratio was 1:1, the pH was 4 and the reaction time was 50min. The removal efficiency of COD in waste water was changed by changing the pH.

Table 3. Effect of pH on COD removal efficiency

pH	3	4	5	6	7	8
Removal efficiency /%	22.4	28.8	36.2	24.5	21.5	20.8

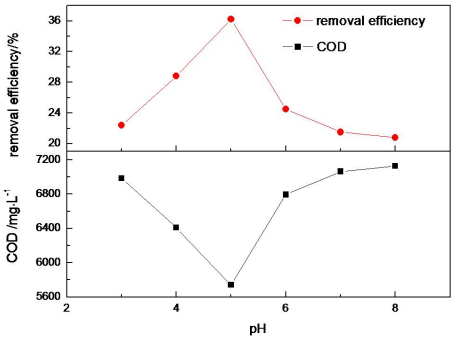

Fig. 3. Influence of pH on COD removal efficiency

As shown in Fig. 3, with the increase of pH, COD removal first increased and then decreased. When the pH was 5, the removal efficiency reached up to 36.2%. When the pH was low, the treatment efficiency was generally better than the alkaline conditions. However, when pH was too low, iron dissolved a large amount of Fe^{3+} and Fe^{3+} causes flocculation and precipitation of organics, which is easy to cause packing blockage, which was not conducive to the formation of the original battery and the removal of COD. On the other hand, when pH was alkaline, H^+ concentration was low, which was also not conducive to the formation of the original battery and reduced the COD removal efficiency on the effect of Ferro-carbon micro-electrolysis.

3.1.3 Effect of reaction time on COD removal efficiency

When the Fe-C mass ratio was 1:1 and the pH value was 5 and the activated carbon number was 20, changes the reaction time, the removal efficiency of COD in the wastewater after the reaction was shown in Table 4.

Table 4. Effect of reaction time on COD removal efficiency

Reaction time / min	10	20	30	40	50
Removal efficiency / %	25	26	33.5	34.6	35.2

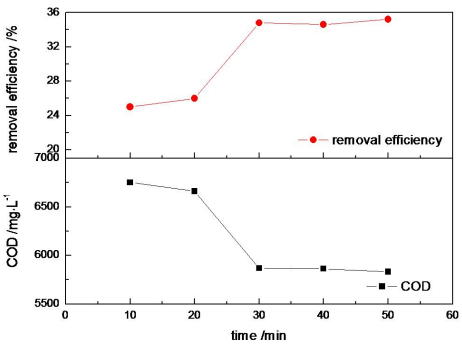

Fig. 4. Reaction time of pH on COD removal efficiency

Fig. 4 shows that, with the extension of reaction time, the removal efficiency of COD gradually increases. When the reaction time was 30min, the removal efficiency was 33.5%.

When the reaction time exceeded 30min, the removal efficiency of COD increased slowly with the increase of reaction time, and remains basically unchanged. The possible mechanism is that the oxidative effect of Ferro-carbon microcells is close to the maximum treatment capacity of pollutant degradation. Meanwhile, the adsorption and catalytic oxidation of activated carbon to COD achieves the dynamic balance under certain pollutant concentration and aeration conditions.

3.2 Discussion

Response Surface Methodology (RSM) is a mathematical statistical method for optimization of multi-factor system, which has been widely used in optimization of various waste water treatment processes, is a reliable and simple statistical tool[7][8].

In this study, RSM was used to analyze and optimize the main influencing factors, which includes the mesh number of activated carbons, pH and the reaction time, in the process of Ferro-carbon micro-electrolysis treatment of 1, 4-butanediol mixed wastewater.

A quadratic polynomial was established for the relationship between the response R1 (COD removal efficiency) and each parameter (reaction time A, pH is B, and the mesh number of activated carbon is C), which is coded as follows:

$$R1=30.6+0.077A-1.91B+0.19C+0.04AB+0.02AC+0.08BC \quad (1)$$

The A, B and C are encoding values of the response parameters, the factors before the encoding values represent the influence direction and influence the degree of the parameters [7]. According to the formula:

$$R1=30.6+0.077A-1.91B+0.19C+0.04AB+0.02AC+0.08BC$$

The study of Ferro-carbon micro-electrolysis conducts that the number of time and activated carbon has a positive effect on the response R1, while the pH has a negative effect on the response volume R1. The order of influence degree was: pH > the mesh number of activated carbons > reaction time, and pH had the greatest influence on the treatment efficiency of 1, 4 butanediol wastewater by Ferro-carbon micro-electrolysis.

Table 5. Experimental results of 1,4butanediol wastewater

NO	A time/ min	B pH	C mesh	Removal efficiency / %
1	50	7	30	16
2	50	3	8	28.9
3	50	3	30	34.6
4	10	7	30	26
5	10	7	8	21
6	10	3	30	28
7	50	7	8	24
8	10	3	8	26

3.2.1 Fitting optimization of pH with reaction time

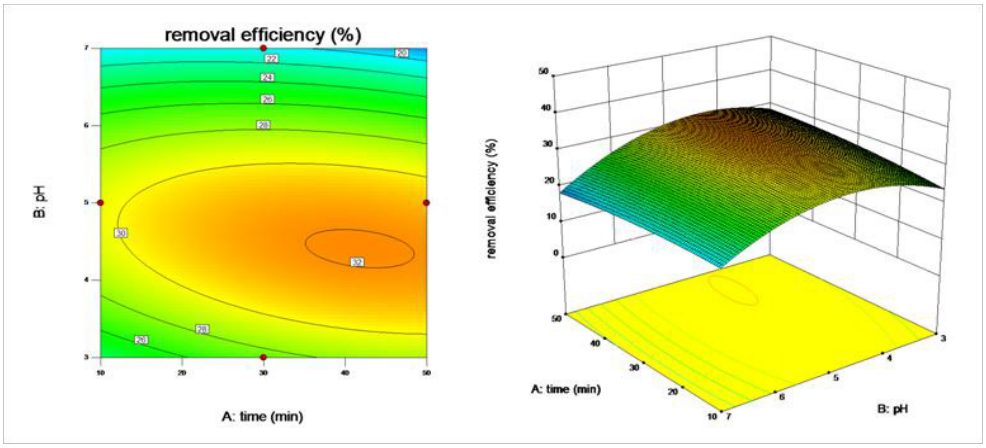

Fig. 5. Effect of reaction time and pH on COD removal efficiency (a) contour map (b) response surface map

Fig. 5 shows that under the condition of the activated carbon mesh number of 20, the reaction time was greater than 30min, the reaction time affected the COD removal efficiency gently and the pH was the main factor influencing the COD removal efficiency. With the increase of pH, COD removal efficiency first increased and then decreased, and the COD removal efficiency reached the maximum when pH was 5.

3.2.2 Fitting optimization of activated carbon mesh number with the reaction time and pH

As shown in Fig.6 and Fig.7, through optimization analysis of various parameters, the reaction condition after optimization was as follows: the mesh number of activated carbons was 22, the pH was 5 and the reaction time was about 28 min.

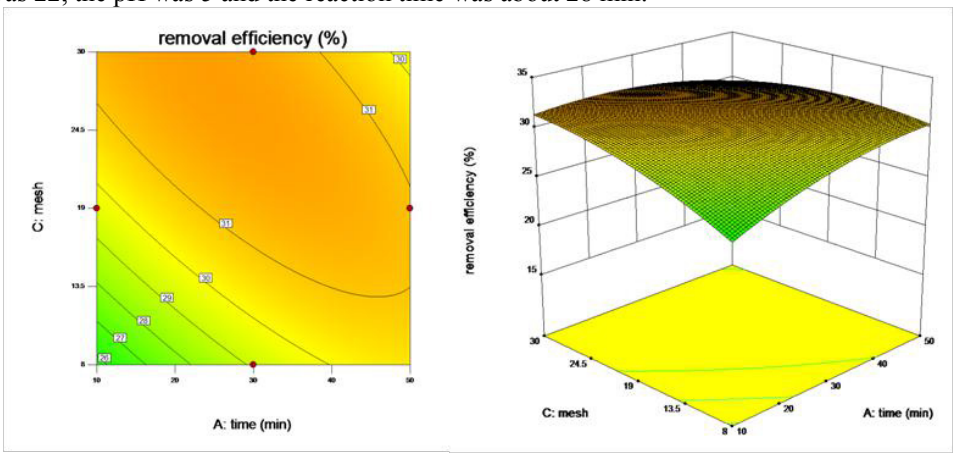

Fig. 6 Effect of reaction time and activated carbon mesh number on COD removal efficiency (a) contour map (b) response surface map

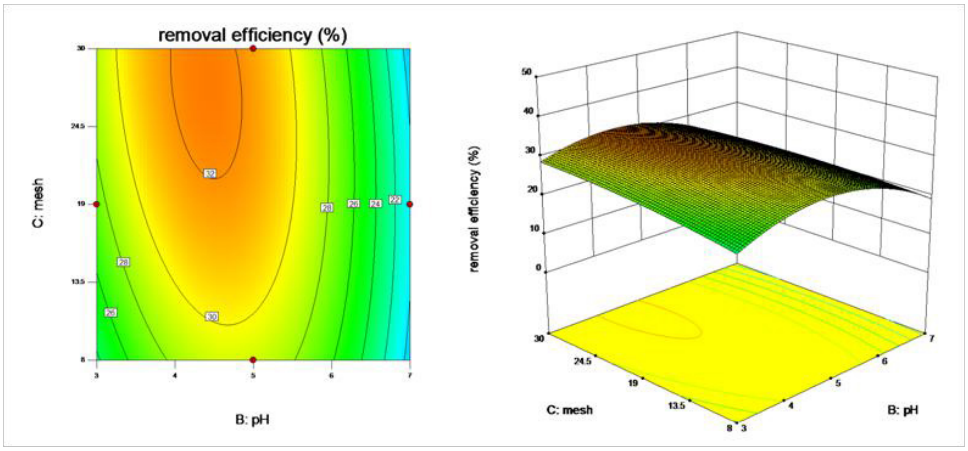

Fig. 7 Effect of pH and activated carbon mesh number on COD removal efficiency (a) contour map (b) response surface map

4 Conclusions

(1) The application of Ferro-carbon micro-electrolysis in the pretreatment of 1, 4-butanediol wastewater, can reduce the pollution load of subsequent systems and improve the biochemical property of wastewater.

(2) When the activated carbon mesh number was 20, pH value was 5 and reaction time was 30min, the removal efficiency of COD was 36.2%.

(3) RSM method was used to optimize the experimental results. The optimal working condition: activated carbon mesh number was 22, and pH value was 5 and reaction time was 28 min.

Through the analysis of experimental results by RSM, the relationship between each influencing factor and COD removal efficiency is conducted, as follows:

$$R1=30.6+0.077A-1.91B+0.19C+0.04AB+0.02AC+0.08BC$$

The reaction time and the mesh number of activated carbons have a positive effect on the COD removal efficiency, while the pH has a negative effect on the COD removal efficiency. The order of influence degree is: pH > the mesh number of activated carbons > reaction time, and pH has the greatest influence on the treatment rate of 1,4 butanediol wastewater by Ferro-carbon micro-electrolysis.

5 References

1. H.X. Guo. Xi 'an University of Architecture and Technology, China (2004).
2. Z.H. Lu. College of Sciences Zhejiang University Hangzhou, China, May, (2008).
3. Y. Zuo, J. Liu, German et al. Environmental Science & Technology, China, **S2**, 261-262 (2010).
4. J.S. Wang, H. Mo. Journal of Lanzhou Railway University, China, **19**:77-80, (2000).
5. Y. Wu, S.Y. Zhu, B. Cao, et al. Industrial Water Treatment, China, **35**:41-43(2015).

6. H. Zhang. Guangxi University, China (2013).
7. J. Zhang, S.Z. Wang, Y. Guo, et al. Xi 'an Jiao tong University, China (2010).
8. I. Arslanalaton, A. Akin, T. Olmezhanci. J CHEM TECHNOL BIOT, **85**, 493-501(2010).